2023

BAND GAP ENGINEERING IN TERNARY OXIDES AND SULFIDES: A ROUTE TO NEW PHOTOELECTRODES FOR SOLAR ENERGY CONVERSION

Fahad Ibrahim Danladi

BAND GAP ENGINEERING IN TERNARY OXIDES AND SULFIDES: A ROUTE TO NEW PHOTOELECTRODES FOR SOLAR ENERGY CONVERSION

by

FAHAD IBRAHIM DANLADI

DISSERTATION

Submitted in partial fulfillment of the requirements for the degree of Doctor of Philosophy at

The University of Texas at Arlington

August 2023

Arlington, TX

Supervising committee:

Krishnan Rajeshwar, Supervising Professor

Robin T. Macaluso

Peter Kroll

Rasika Dias

Kayunta Johnson-Winters

ACKNOWLEDGEMENTS

Throughout my doctoral studies, I was fortunate to have the support and guidance of family, friends, mentors, and collaborators who made a positive impact on my life. Their encouragement, motivation, assistance, and advice were invaluable to me, and I am forever grateful for their contributions. In the acknowledgments section of my dissertation, I will express my heartfelt appreciation for these exceptional individuals who stood by me during my years of hard work and dedication in graduate school.

First of all, I would like to start by thanking and appreciating God almighty for granting me the resilience and direction to complete my graduate studies successfully. Additionally, I want to thank my parents, Amina Sabo Bakin Zuwo and Ibrahim Danladi Mohammed, for their unwavering support and constant prayers throughout my academic journey. I am also deeply grateful to my spouse, Fatima Mouktar, for her ceaseless encouragement and motivation. Ultimately, I cannot thank my beloved daughters, Farha, Fariha, and Fahimah, enough for always being by my side. Additionally, my siblings Baba Lawan, Hadiza, Aminu, late Aliyu, Bidayat, Jamila, and Mansur have always been there for me, and I appreciate their presence in my life.

I would also like to express my sincere gratitude to Professor Krishnan Rajeshwar for his unwavering support, invaluable guidance, mentorship, and motivation throughout my graduate studies. Professor Rajeshwar's nurturing environment allowed me to excel in my academic pursuits, and I will always be grateful for his indispensable assistance in my research. Thank you, Professor Rajeshwar, for treating me like family, you are a remarkable father figure and role model.

During my graduate studies, I was fortunate to have the support and opportunity to work in Dr. Robin T. Macaluso's laboratory, for which I am deeply grateful. Additionally, I am thankful to my dissertation

committee members, Drs., Robin T. Macaluso, Peter Kroll, Rasika Dias, and Kay L Johnson-Winters, for their valuable feedback, advice, and support throughout my research work. I would like to acknowledge our collaborators: Dr. Efstathios I. Meletis, Dr. Mark C. Hersam, Dr. Vinod K. Sangwan, Dr. Hori Pada Sarker, Dr. Abhishek Kumar Adak, Chuzhong Zhang, and Riddhi Ananth for their support.

I am grateful for the support and guidance provided by my colleagues Abhishek Rawat, Dr. Abbas Vali, Dr. Mohammed Kabir Hossain, Eric Cyganowski, Jacob Fulton, and Ana Gonzalez. I am also grateful to Dr. William Cleaver, Dr. Cynthia Griffith, and Naje Huff for creating a memorable teaching experience. I extend my sincere appreciation to Drs. Roy McDougald, Brian Edwards, Jiechao Jiang, and Yi Shen for their dedication and hard work in ensuring that the instruments operate smoothly. Finally, I am thankful for the kind assistance and unwavering support of Debbie Cooke, Jill Howard, Stephanie Henry, Dorothy Sullivan, and Beth Klimek.

TABLE OF CONTENTS

LIST OF ILLUSTRATIONS

represents the total density of states, while the green line displays the projection on Cu 3*d* orbital, Mg 3*s* and 2*p* orbitals, and Ca 4*s* and 3*p* orbitals for the respective compounds. Furthermore, the blue line represents the V 3*d* orbital, and the red line represents the O 2*p* orbital. It is essential to note that for the band structure of CuV_2O_6, only one spin channel was shown as both spin down and up channels have the same band features.

Figure 2-13. The electronic band structure and projected density of states (PDOS) for (a, b) $Mg_{0.1}Cu_{0.9}V_2O_6$ and (c, d) $Ca_{0.1}Cu_{0.9}V_2O_6$ have been calculated in a 1 x 5 x 1 supercell. The black line represents the total density of states, while the orange line displays the projection on Mg 3*s* and 2*p* orbitals, and Ca 4*s* and 3*p* orbitals for the respective compounds. Furthermore, the green line represents Cu 3*d* orbital, the blue line represents the V 3*d* orbital, and the red line represents the O 2*p* orbital. It is essential to note that the system has a net nonzero magnetic moment due to the presence of odd numbers of Cu atoms in the supercell. Both the spin-up (red) and spin-down (black) channels are shown in the band structure plot.

Figure 2-14. (a) UV-Vis optical absorption spectra and Tauc plots corresponding to allowed (b) direct and (c) indirect transitions for the end members CuV_2O_6, MgV_2O_6, CaV_2O_6 and solid solutions $A_{0.1}Cu_{0.9}V_2O_6$.

Figure 2-15. Linear sweep voltammogram for CuV_2O_6, $Mg_{0.1}Cu_{0.9}V_2O_6$ and $Ca_{0.1}Cu_{0.9}V_2O_6$ in (a) 0.1 M borate buffer solution (pH = 8), (b) 0.1 M borate buffer + 4 M formate solution (pH = 8) under front-side illumination. The potential sweep rate was 5 mV/s.

Figure 3-1. Comparison of XRD patterns for various polymorphs of pyrovanadates obtained by changing anneal temperature and their respective reference in black: (a) triclinic (ICDD 128342) and monoclinic (ICDD 086711) $Mg_2V_2O_7$, (b) triclinic (ICDD 133067) $Ca_2V_2O_7$, (c) tetragonal (ICSD 10330) and triclinic (ICDD 125309) $Sr_2V_2O_7$ and (d) monoclinic (ICDD 260569) and orthorhombic (ICSD 1831) $Cu_2V_2O_7$.

Figure 3-2. Comparison between experimental and reference (in black) XRD patterns for the solid solutions and end members: (a) monoclinic $Mg0_{.67}Cu_{1.33}V_2O_7$ (ICSD 69732), (b) monoclinic $CaCuV_2O_7$ (ICSD 33851) and, (c) orthorhombic $SrCuV_2O_7$ (ICSD 33852).

Figure 3-3. Rietveld refinement plots for the end members and solid solutions: (a) monoclinic β-$Cu_2V_2O_7$, (b) orthorhombic α-$Cu_2V_2O_7$, (c) monoclinic $Mg_2V_2O_7$, (d) triclinic $Ca_2V_2O_7$, (e) triclinic $Sr_2V_2O_7$ (f) monoclinic $Mg0_{.67}Cu_{1.33}V_2O_7$, (g) monoclinic $CaCuV_2O_7$ and, (h) orthorhombic $SrCuV_2O_7$.

Figure 3-4. Crystal structure for (a) monoclinic β-$Cu_2V_2O_7$, (b) orthorhombic α-$Cu_2V_2O_7$, (c) monoclinic $Mg_2V_2O_7$, (d) triclinic $Ca_2V_2O_7$, (e) triclinic $Sr_2V_2O_7$ (f) monoclinic $Mg0_{.67}Cu_{1.33}V_2O_7$, (g) monoclinic $CaCuV_2O_7$ and, (h) orthorhombic $SrCuV_2O_7$.

Figure 3-5. Room temperature Raman spectra for the (a) end members β-$Cu_2V_2O_7$, α-$Cu_2V_2O_7$, $Mg_2V_2O_7$, $Ca_2V_2O_7$, and $Sr_2V_2O_7$ and the solid solutions; (b) $Mg0_{.67}Cu_{1.33}V_2O_7$, (c) $CaCuV_2O_7$, (d) $SrCuV_2O_7$.

Figure 3-6. SAED patterns for (a) β-$Cu_2V_2O_7$, (b) α-$Cu_2V_2O_7$, (c) $Ca_2V_2O_7$, and (d) $CaCuV_2O_7$. The SAED spots are indexed to the corresponding unit cells illustrated in Figure 3-4.

LIST OF TABLES

LIST OF ABBREVIATIONS

Å	Angstrom
AES	Atomic emission spectroscopy
AFM	Antiferromagnetic
CBM	Conduction band minima
DFT	Density functional theory
DRS	Diffuse reflectance spectroscopy
EDX	Energy-dispersive x-ray spectroscopy
*E*g	Energy gap
FM	Ferromagnetic
FTO	Fluorine-doped tin oxide
HER	Hydrogen evolution reaction
ICP	Inductively-coupled plasma
MA	Malic acid
OER	Oxygen evolution reaction
PDOS	Projected density of state
PEC	Photoelectrochemical
RHE	Reversible hydrogen electrode
SAED	Selected area electron diffraction pattern
SCS	Solution combustion synthesis
SEM	Scanning electron microscopy
TEM	Transmission electron microscopy
UV-vis	Ultraviolet-visible
VBM	Valence band maxima
XRD	X-ray diffraction

ABSTRACT

BAND GAP ENGINEERING IN TERNARY OXIDES AND SULFIDES: A ROUTE TO NEW PHOTOELECTRODES FOR SOLAR ENERGY CONVERSION

Fahad Ibrahim Danladi, Ph.D.

The University of Texas at Arlington, 2023

Supervising Professor: Krishnan Rajeshwar

In recent years, there has been a growing interest in semiconductor photoelectrodes that can effectively split water into hydrogen and oxygen using sunlight. However, there is currently no known material that is efficient enough to be used for commercial purposes. Photoelectrodes currently have an efficiency of less than 10% in converting water under visible light irradiation. There is a need to develop an efficient semiconductor photoelectrode for photoelectrochemical water splitting that is both chemically stable and affordable, composed of earth-abundant elements and capable of operating under visible light. Metal oxides are considered promising photoelectrode materials due to their low cost, stability against oxidation, and tunable band gaps. This study aims to expand the library of metal oxide and sulfide materials that could potentially be used as photoelectrode materials for photoelectrochemical (PEC) water splitting.

This research briefly introduces the photoelectrochemical technique and reviews various methods to tune the optoelectronic properties of semiconductors for solar fuel generation, focusing on improving the performance of visible-light active PEC materials. Through a combination of theory and experimentation, the potential of ternary metal oxide semiconductors in the A-Cu-V-O family (A= alkaline earth metal) was evaluated for PEC water splitting. By successfully incorporating 10% alkaline earth metals into α-CuV_2O_6, the optical band gap and PEC activity could be fine-tuned.

Finally, we successfully synthesized alkaline earth metal vanadates, namely $Mg_2V_2O_7$, $Ca_2V_2O_7$, and $Sr_2V_2O_7$, as well as quaternary vanadates of copper and alkaline earth metals through a solution combustion synthesis method that is both time- and energy-efficient. These metal oxide semiconductors have the potential as photoelectrode materials for PEC water splitting. We used both theory and experiment to investigate the effect of alkaline earth metal substitution on the crystal structure, optoelectronic properties, and PEC properties of copper pyrovanadate. Additionally, we were able to synthesize two polymorphs of ternary praseodymium sulfide, cubic $NaPrS_2$ (C) and rhombohedral $NaPrS_2$ (R), via the solid-state method. Notably, we successfully produced the layered R-$NaPrS_2$ for the first time through slow cooling to room temperature.

CHAPTER 1

INTRODUCTION

Carbon dioxide, nitrous oxide, and chlorofluorocarbon emissions from global energy generation have continued to accelerate the warming of the earth's surface.[1] To mitigate the global increase in temperature, there is a need for a significant reduction in emissions by moving towards renewable energies. Photocatalytic and photoelectrochemical water splitting (artificial photosynthesis) are alternative sources of clean, safe, and sustainable energy that uses solar energy to convert water into hydrogen and oxygen.

Photoelectrochemical (PEC) water splitting is a simple technique that generates electron and hole pairs when two electrodes are irradiated with UV light as shown in Figure 1-1.[2] These electrodes are semiconductors that absorb photon energy to reduce water to hydrogen (at the cathode) or oxidize it to oxygen (at the anode) with or without external bias. The separation of the photogenerated electron-hole pair generates a photopotential that drives the electrochemical conversion of water to oxygen and hydrogen.[2] A long-standing challenge has been the lack of efficient semiconductor photoelectrodes for water splitting into gaseous hydrogen and oxygen or carbon dioxide reduction under visible light irradiation.[3, 4] So far, the efficiency of this photoelectrode for water splitting with visible light is less than 10% (a generally considered threshold for commercial application).[4] Over the past decade, researchers have intensified efforts in the development of new semiconductor materials and improving the performance of existing ones for PEC technology.[2-7]

Oxidation: $2H_2O_{(l)} + 4h^+ \rightarrow 4H^+ + O_{2(g)}$ (1)

Reduction: $4H^+ + 4e^- \rightarrow 2H_2$ (2)

Overall reaction: $2H_2O_{(l)} \rightarrow 2H_{2(g)} + 2O_{2(g)}$ $\Delta G = +237.2$ kJ/mol (3)

For the oxygen evolution reaction (OER) described in equation 1, the potential of the valence band edge needs to be higher than the water oxidation potential of 1.23 V vs RHE. On the other hand, the hydrogen evolution reaction (HER) shown in equation 2 requires the potential of the conduction band edge to be higher than the proton reduction potential of 0.00 V vs RHE. Hence, to drive the water splitting reaction as per equation 3, a theoretical minimum optical band gap threshold of approximately 1.23 eV is necessary.

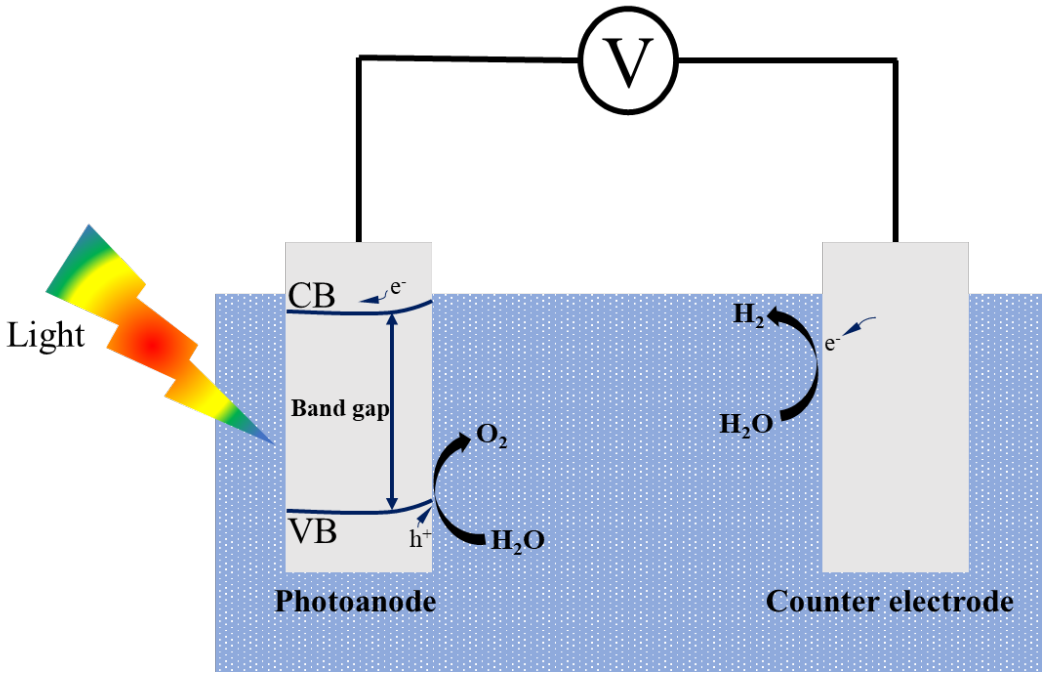

Figure 1-1. Schematic diagram for photoelectrochemical water splitting.

Tuning the optoelectronic properties of semiconductors for solar fuel generation is an attractive approach for enhancing the performance of visible-light active PEC catalysts. This can be achieved by substituting anions in metal oxide photoelectrodes with elements like sulfur and nitrogen to form oxysulfide and oxynitride, respectively, thus reducing the bandgap and improving carrier transport.[8-20] Metal oxides typically possess large bandgaps with O 2*p* orbitals being the main contributor to the valence band maxima, which are situated at a relatively lower energy level. It

was observed that subjecting a $BiVO_4$ photoelectrode to a simple heat treatment in a sulfur vapor atmosphere led to a decrease of approximately 0.3 eV in its band gap and a significant improvement in charge carrier transport.[8] Density functional theory calculations revealed that sulfur incorporation into $BiVO_4$ resulted in an upward shift of the valence band by around 0.4 eV as a result of additional electronic states originating from S 3*p*. Similarly, incorporating sulfur into monoclinic tungsten trioxide, WO_3, via spray pyrolysis with ammonium sulfide resulted in a red shift of the absorption edge spectrum from roughly 2.7 to 2.6 eV, thereby improving its visible light absorption and PEC performance.[9]

Figure 1-2 demonstrates that partial replacement of oxygen by nitrogen ions in tantalum oxide results in the formation of oxynitride and reduced band gap.[16, 21] This is because the O 2*p* orbitals are in a lower state compared to N 2*p* orbitals. Nitridation of tantalum oxide (Ta_2O_5), a semiconductor with a large bandgap of 3.9 eV results in the formation of tantalum oxynitride (TaON) with a favorable bandgap of 2.4 eV and tantalum nitride (Ta_3N_5), a visible light absorber with a bandgap of 2.1 eV.[12-16, 21] Additionally, nitridation of $BiVO_4$ has the potential to decrease its band gap to less than 2.4 eV, despite its valence band maxima being raised upward as a result of hybridization with Bi 6s orbital. Both experimental and first principle calculations have shown significant band gap reduction of around 0.2 eV and enhancement of electron-hole separation when nitrogen was incorporated into $BiVO_4$ to form $BiVO_{3.54}N_{0.31}$.[11, 17] Successful incorporation of nitrogen into zinc oxide (ZnO) crystal lattice via ion implantation method revealed a red shift in the optical absorption edges form 390 nm in ZnO to 550 nm (visible light region) in nitrogen doped ZnO nanorod arrays.[20]

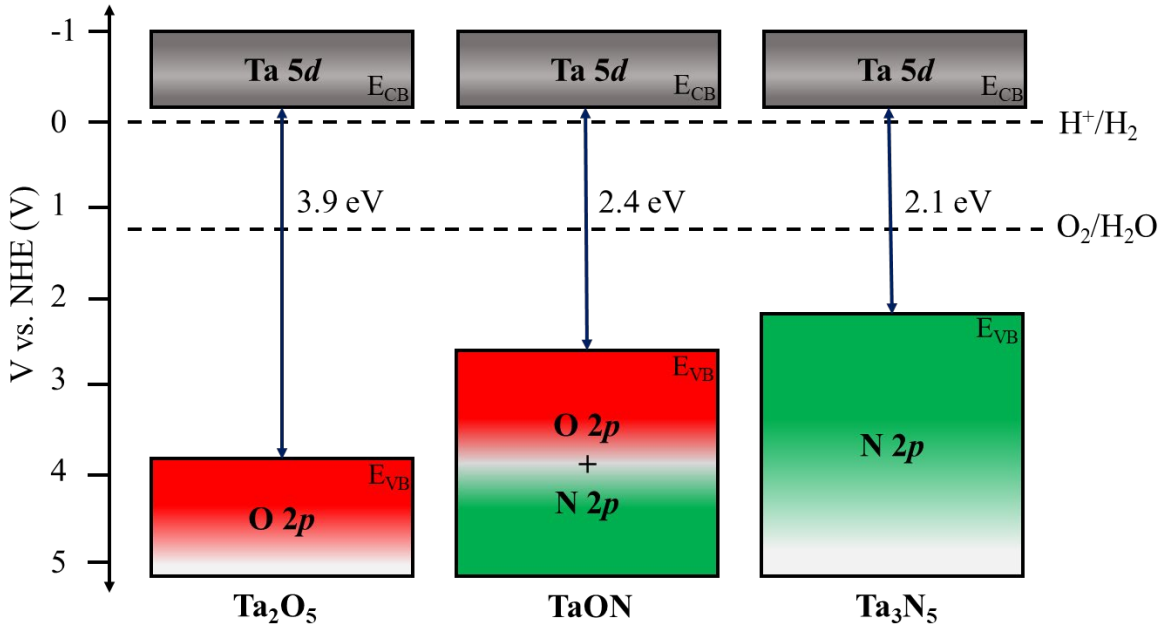

Figure 1-2. Band diagram of tantalum oxide, oxynitride and nitride showing valence band edge increase upon nitridation.[21]

Chemical composition variation and polymorphic transformation have been reported to tune the optical band gap of photoelectrode for solar water splitting.[22-25] Three ternary copper vanadates (CuV_2O_6, $Cu_2V_2O_7$ and $Cu_3V_2O_8$) with varying copper/vanadium stoichiometric ratios were synthesized via solution combustion synthesis.[22] Based on the DFT + U method analysis of the electronic band structures and projected density of state, it was found that the valence band maxima of copper vanadates were made up of O 2*p* and Cu 3*d*, while the conduction band minima were predominantly V 3*d* states. The optical band gaps for α-CuV_2O_6, α-$Cu_2V_2O_7$, β-$Cu_2V_2O_7$, and $Cu_3V_2O_8$ were calculated to be 1.89 eV, 2.12 eV, 2.28 eV, and 2.11 eV, respectively.[22] A similar study on ternary Cu-V-O family of compounds showed that the optical band gaps of α-$Cu_2V_2O_7$, β-$Cu_2V_2O_7$, $Cu_3V_2O_8$, and $Cu_{11}V_6O_{26}$ were 2.26, 2.23, 2.05 and 2.01 eV, respectively.[23] Furthermore, a Tauc plot[26] showed α-CuV_2O_6 thin film synthesized via a facile drop casting method had an optical band gap of approximately 1.95 eV whereas Mott-Schottky plots ($1/C^2$ vs V)[27] revealed that the flat band potential was in the range of 0.74 – 0.80 V vs RHE. A photocurrent

density of 25 μA was reported at 1.23 V vs RHE in 0.1 M NaBi buffer solution.[24] In comparison, β-$Cu_2V_2O_7$ has a band gap of 1.98 eV, with a flat band potential ranging from 0.68 to 0.77 V vs RHE and a photocurrent density of approximately 35 μA at 1.23 V vs RHE.[24] Therefore, the optoelectronic and photoelectrochemical properties were found to be significantly influenced by the compound stoichiometry.

Oxygen vacancy plays an important role in tuning the electronic and optical properties of ternary oxides.[28-32] The band gap of ternary oxides $M_2V_2O_{7-\delta}$ (M = Zn, Cu) synthesized in a deep eutectic solvent was modified by the presence of oxygen vacancies and mixed oxidation states of the metal ions.[28] The main absorption edge of α-$Zn_2V_2O_7$ showed a red shift as the percentage concentration of oxygen defects increased. The estimated band gaps for 18.12%, 23.34%, and 25.35% oxygen defect concentration were 2.63, 2.25, and 1.97 eV respectively, corresponding to absorption edges at 443.5 nm, 471.6 nm, and 500.6 nm.[28] Intriguingly, additional absorption edge (mid-gap state) in the visible range was observed as the concentration of oxygen defects increases which is attributed to the generated 3*d* orbital of reduced V^{+4} ion.[28] Similarly, increasing the concentration of oxygen vacancies in β-$Cu_2V_2O_7$ leads to a reduction in optical ban gap and creates mid-gap states of Cu^+ between the valence and conduction bands.[28] Furthermore, the absorption edge of $BiVO_4$ photoelectrode was enhanced beyond 530 nm upon heat treatment under hydrogen atmosphere which resulted in substantial improvement of photoactivity.[29] This treatment creates oxygen vacancies and hydrogen impurities in $BiVO_4$ photoelectrode, thereby leading to new electronic transitions between the defect states and band-edge states.[29]

Introduction of oxygen vacancies into WO_3 through heat treatment under hydrogen atmosphere extended its optical absorption edge as well as enhancing photoactivity and photostability.[30] Similarly, hydrogenation of TiO_2 nanocrystal creates disorder on the surface layers

which leads to narrowing of the band gap and enhancement of solar absorption.[31] The onset of absorption shifted from ultraviolet (3.30 eV) in the pristine TiO_2 to near-infrared (1.00 eV) in the modified nanocrystal, whereas the energy of the valence band maxima increases substantially and that of the conduction band minima change insignificantly upon hydrogenation. This shift in the onset of absorption could be attributed to optical transitions from the blue shifted valence band maxima to the conduction band tail states.[31]

Another approach to modify the optical band gap of photoelectrode is by incorporating a foreign metal cation to form a mixed cation system. The incorporation of a metal cation into bismuth vanadate was reported to tune the optical band gap and improved its PEC performance.[33-36] The absorption edge of $BiVO_4$ (520 nm) increased as bismuth was replaced by iron via electrospinning, confirming that iron incorporation resulted in increasing the visible light absorption range from 520 nm to 600 nm.[33] Compared to pure $BiVO_4$, $Bi_{0.5}Fe_{0.5}VO_4$ mesoporous film showed superior photoactivity up to around 560 nm, improved charge carrier transfer and separation efficiencies.[33] Combinatorial alloying of P, Ca, Mo, Eu, Gd and W into $BiVO_4$ showed that its optical band gap decreased by approximately 0.1 eV in the case of alloying with Mo and Gd, leading to improved PEC performance.[34, 35] Furthermore, $BiCu_2VO_6$ powder prepared via solid-state method showed improved photocatalytic activity for oxygen evolution when compared to $BiVO_4$.[36] It has been reported that $BiCu_2VO_6$ absorbs visible light, starting at approximately 600 nm which is longer than the absorption onset for $BiVO_4$.[36] The optical band gap of $BiCu_2VO_6$ determined from the absorption onset was 0.3 eV lower than that of $BiVO_4$. The narrowing of the band gap from 2.4 eV in $BiVO_4$ to 2.1 eV in $BiCu_2VO_6$ was attributed to mixing of the Cu 3*d* orbital with the V 3*d* conduction band of $BiVO_4$, as well as the retention of mixed Bi 6*s* and O 2*p* valence band in $BiCu_2VO_6$.[36]

Tuning the band gap of visible light inactive sulfides, ZnS and $AgInS_2$ through alloying yielded an active photocatalyst, $(AgIn)_xZn_{2(1-x)}S_2$ for hydrogen evolution under visible light irradiation.[37] The band gaps of the solid solutions were narrowed down to 2.40 – 1.95 eV from 3.55 and 1.80 eV in the end members ZnS and $AgInS_2$, respectively. The valence band maxima of the solid solution $(AgIn)_xZn_{2(1-x)}S_2$ was composed of hybrid orbitals of S 3*p* and Ag 4*d* (a combination of ZnS and $AgInS_2$ valence bands) whereas the conduction band minima was composed of Zn 4*s*4*p* and In 5*s*5*p* hybrid orbitals.[37] Therefore, changing the ratio of ZnS and $AgInS_2$ in the solid solution, will shift the valence and conduction bands, thereby tuning the optical band gap and band structure. Furthermore, the ratio of ZnS and $CuInS_2$ was varied to control the optical band gap of $(CuIn)_xZn_{2(1-x)}S_2$ solid solutions.[38] This modification improved the photocatalytic activity and allowed the band gap of the solid solutions to fall within the range of 2.67 – 1.75 eV, even though the band gap of the end members, ZnS and $CuInS_2$, were 3.40 and 1.40 eV, respectively. Similarly, the position of the absorption edge blue shifted whereas that of the conduction band of $Cd_{(1-x)}Zn_xS$ solid solutions shifted towards more negative potentials (Figure 1-3) as the value of x increased, confirming the dependence of the optical band gap on alloying.[39]

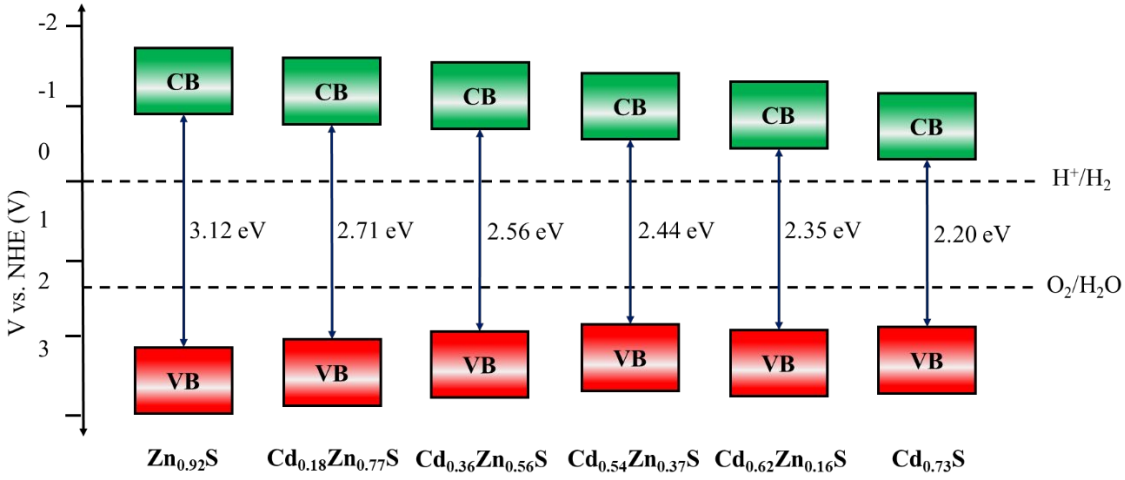

Figure 1-3. The position of the valence and conduction band potentials for $Cd_{(1-x)}Zn_xS$.[39]

Alloying has proven to be a successful technique in enhancing material performance for different applications. Therefore, our focus was on a thorough investigation of A-Cu-V-O system's potential for solar water splitting. As depicted in Figure 1-4, a ternary diagram illustrates potential thermodynamically ternary and quaternary compounds in the A-Cu-V-O system, where A represents Mg, Ca, or Sr. There are many different ternary compounds that can be found along the AO-V_2O_5 route shown in Figure 1-4. These include AVO_3, AV_2O_4, AV_2O_5, AV_2O_6, AV_3O_7, AV_4O_9, $A_2V_2O_7$ and $A_3V_2O_8$. The Cu-V-O system also has a variety of combinations along the CuO-V_2O_5 composition line, which have been extensively studied by our group and others in the field.[22, 40] There are also multiple possible quaternary compounds available in the A-Cu-V-O system. However, solution combustion synthesis of A-V-O and A-Cu-V-O systems as well as their optical and PEC properties has not been reported in the literature.

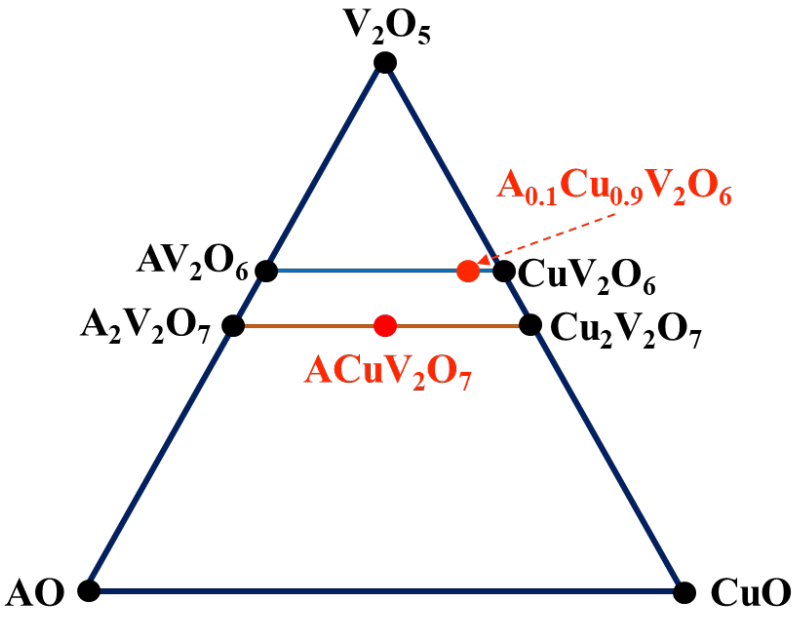

Figure 1-4. The ternary diagram illustrates the thermodynamically possible ternary and quaternary compounds in the A-Cu-V-O system, where A represents Mg, Ca, or Sr.

The focus of this dissertation is to develop efficient solution combustion synthesis techniques for A-V-O and A-Cu-V-O systems with ternary and quaternary compositions, with the aim of modifying their optical band gap and PEC behavior. The second chapter of this dissertation focuses on utilizing solution combustion synthesis to modify the structural, electronic, optical, and PEC properties of copper metavanadate by substituting it with alkaline earth metals. The experimental results were supported by a collaborative computational study. Chapter three details the time- and energy-efficient synthesis of various ternary $Cu_2V_2O_7$, $A_2V_2O_7$, and quaternary $ACuV_2O_7$ compounds, along with a comparative analysis of their properties in relation to solar water splitting, including their electronic, optical, and structural characteristics. Finally, key synthetic parameters of ternary praseodymium sulfide, $NaPrS_2$, were identified and discussed in chapter four. Solid state method was employed to synthesize two polymorphs of $NaPrS_2$, and we were able to control their cation ordering by varying the cooling rate, resulting in changes in their optical band gaps. In conclusion, chapter five provides a summary and outlines potential directions for future research.

REFERENCES

1. Short, F. T.; Neckles, H. A., The Effects of Global Climate Change on Seagrasses. Elsevier B.V: 1999; Vol. 63, pp 169-196.
2. Sivula, K.; van de Krol, R., Semiconducting Materials for Photoelectrochemical Energy Conversion. *Nature reviews. Materials* **2016,** *1* (2), 15010.
3. Kudo, A.; Miseki, Y., Heterogeneous Photocatalyst Materials for Water Splitting. *Chemical Society reviews* **2009,** *38* (1), 253-278.
4. Osterloh, F. E., Inorganic Materials as Catalysts for Photochemical Splitting of Water. *Chemistry of materials* **2008,** *20* (1), 35-54.
5. Aroutiounian, V. M.; Arakelyan, V. M.; Shahnazaryan, G. E., Metal Oxide Photoelectrodes for Hydrogen Generation Using Solar Radiation-Driven Water Splitting. *Solar energy* **2005,** *78* (5), 581-592.
6. Bard, A. J.; Fox, M. A., Artificial Photosynthesis: Solar Splitting of Water to Hydrogen and Oxygen. *Accounts of chemical research* **1995,** *28* (3), 141-145.
7. Lin, Y.; Yuan, G.; Liu, R.; Zhou, S.; Sheehan, S. W.; Wang, D., Semiconductor Nanostructure-Based Photoelectrochemical Water Splitting: A Brief Review. *Chemical physics letters* **2011,** *507* (4-6), 209-215.
8. Lamers, M.; Li, W.; Favaro, M.; Starr, D. E.; Friedrich, D.; Lardhi, S.; Cavallo, L.; Harb, M.; van de Krol, R.; Wong, L. H.; Abdi, F. F., Enhanced Carrier Transport and Bandgap Reduction in Sulfur-Modified $BiVO_4$ Photoanodes. *Chemistry of materials* **2018,** *30* (23), 8630-8638.
9. Rettie, A. J. E.; Klavetter, K. C.; Lin, J.-F.; Dolocan, A.; Celio, H.; Ishiekwene, A.; Bolton, H. L.; Pearson, K. N.; Hahn, N. T.; Mullins, C. B., Improved Visible Light Harvesting of WO_3 by Incorporation of Sulfur or Iodine: A Tale of Two Impurities. *Chemistry of materials* **2014,** *26* (4), 1670-1677.
10. Khan, A.; Ahmed, M. I.; Adam, A.; Azad, A. M.; Qamar, M., A Novel Fabrication Methodology for Sulfur-Doped ZnO Nanorods as an Active Photoanode for Improved Water Oxidation in Visible-Light Regime. *Nanotechnology* **2017,** *28* (5), 055602-055602.
11. Kim, T. W.; Ping, Y.; Galli, G. A.; Choi, K.-S., Simultaneous Enhancements in Photon Absorption and Charge Transport of Bismuth Vanadate Photoanodes for Solar Water Splitting. *Nature communications* **2015,** *6* (1), 8769-8769.
12. Abe, R.; Higashi, M.; Domen, K., Facile Fabrication of an Efficient Oxynitride TaON Photoanode for Overall Water Splitting into H_2 and O_2 under Visible Light Irradiation. *Journal of the American Chemical Society* **2010,** *132* (34), 11828-11829.
13. Chun, W.-J.; Ishikawa, A.; Fujisawa, H.; Takata, T.; Kondo, J. N.; Hara, M.; Kawai, M.; Matsumoto, Y.; Domen, K., Conduction and Valence Band Positions of Ta_2O_5, TaON, and Ta_3N_5 by UPS and Electrochemical Methods. *The Journal of Physical Chemistry B* **2003,** *107* (8), 1798-1803.

14. Hitoki, G.; Takata, T.; Kondo, J. N.; Hara, M.; Kobayashi, H.; Domen, K., An Oxynitride, TaON, as an Efficient Water Oxidation Photocatalyst under Visible Light Irradiation (Lambda < or = 500 nm). *Chemical communications (Cambridge, England)* **2002,** (16), 1698-1699.
15. Higashi, M.; Domen, K.; Abe, R., Highly Stable Water Splitting on Oxynitride TaON Photoanode System under Visible Light Irradiation. *Journal of the American Chemical Society* **2012,** *134* (16), 6968-6971.
16. de Respinis, M.; Fravventura, M.; Abdi, F. F.; Schreuders, H.; Savenije, T. J.; Smith, W. A.; Dam, B.; van de Krol, R., Oxynitrogenography: Controlled Synthesis of Single-Phase Tantalum Oxynitride Photoabsorbers. *Chemistry of Materials* **2015,** *27* (20), 7091-7099.
17. Lai, K.; Zhu, Y.; Lu, J.; Dai, Y.; Huang, B., Synergistic Effects of Codopants on Photocatalytic O_2 Evolution in $BiVO_4$. *Solid state sciences* **2013,** *24*, 79-84.
18. Vojvodic, A.; Medford, A. J.; Studt, F.; Abild-Pedersen, F.; Khan, T. S.; Bligaard, T.; Nørskov, J. K.; Slac National Accelerator Lab, M. P. C. A., Exploring the Limits: A Low-Pressure, Low-Temperature Haber–Bosch Process. *Chemical physics letters* **2014,** *598* (C), 108-112.
19. Wang, G.; Xiao, X.; Li, W.; Lin, Z.; Zhao, Z.; Chen, C.; Wang, C.; Li, Y.; Huang, X.; Miao, L.; Jiang, C.; Huang, Y.; Duan, X., Significantly Enhanced Visible Light Photoelectrochemical Activity in TiO_2 Nanowire Arrays by Nitrogen Implantation. *Nano Letters* **2015,** *15* (7), 4692-4698.
20. Wang, M.; Ren, F.; Zhou, J.; Cai, G.; Cai, L.; Hu, Y.; Wang, D.; Liu, Y.; Guo, L.; Shen, S., N Doping to ZnO Nanorods for Photoelectrochemical Water Splitting under Visible Light: Engineered Impurity Distribution and Terraced Band Structure. *Scientific reports* **2015,** *5* (1), 12925-12925.
21. Abdi, F. F.; Berglund, S. P., Recent Developments in Complex Metal Oxide Photoelectrodes. *Journal of physics. D, Applied physics* **2017,** *50* (19), 193002.
22. Hossain, M. K.; Sotelo, P.; Sarker, H. P.; Galante, M. T.; Kormányos, A.; Longo, C.; Macaluso, R. T.; Huda, M. N.; Janáky, C.; Rajeshwar, K., Rapid One-Pot Synthesis and Photoelectrochemical Properties of Copper Vanadates. *ACS Applied Energy Materials* **2019,** *2* (4), 2837-2847.
23. Zhou, L.; Yan, Q.; Shinde, A.; Guevarra, D.; Newhouse, P. F.; Becerra-Stasiewicz, N.; Chatman, S. M.; Haber, J. A.; Neaton, J. B.; Gregoire, J. M., High Throughput Discovery of Solar Fuels Photoanodes in the CuO-V_2O_5 System. *Advanced energy materials* **2015,** *5* (22), 1500968.
24. Guo, W.; Chemelewski, W. D.; Mabayoje, O.; Xiao, P.; Zhang, Y.; Mullins, C. B., Synthesis and Characterization of CuV_2O_6 and $Cu_2V_2O_7$: Two Photoanode Candidates for Photoelectrochemical Water Oxidation. *Journal of physical chemistry. C* **2015,** *119* (49), 27220-27227.
25. Newhouse, P. F.; Boyd, D. A.; Shinde, A.; Guevarra, D.; Zhou, L.; Soedarmadji, E.; Li, G.; Neaton, J. B.; Gregoire, J. M., Solar Fuel Photoanodes Prepared by Inkjet Printing of Copper Vanadates. *Journal of materials chemistry. A, Materials for energy and sustainability* **2016,** *4* (19), 7483-7494.

26. Tauc, J.; Grigorovici, R.; Vancu, A., Optical properties and electronic structure of amorphous germanium. *Physica status solidi (b)* **1966,** *15* (2), 627-637.
27. Gelderman, K.; Lee, L.; Donne, S. W., Flat-Band Potential of a Semiconductor: Using the Mott–Schottky Equation. *Journal of Chemical Education* **2007,** *84* (4), 685.
28. Hong, S.; Doughty, R. M.; Osterloh, F. E.; Zaikina, J. V.; Argonne National Lab, A. I. L. A. P. S., Deep Eutectic Solvent Route Synthesis of Zinc and Copper Vanadate n-Type Semiconductors - Mapping Oxygen Vacancies and their Effect on Photovoltage. *Journal of materials chemistry. A, Materials for energy and sustainability* **2019,** *7* (19), 1233-12316.
29. Wang, G.; Ling, Y.; Lu, X.; Qian, F.; Tong, Y.; Zhang, J. Z.; Lordi, V.; Rocha Leao, C.; Li, Y., Computational and Photoelectrochemical Study of Hydrogenated Bismuth Vanadate. *Journal of physical chemistry. C* **2013,** *117* (21), 10957-10964.
30. Wang, G.; Ling, Y.; Wang, H.; Yang, X.; Wang, C.; Zhang, J. Z.; Li, Y., Hydrogen-Treated WO_3 Nanoflakes Show Enhanced Photostability Electronic **2012,** *5* (3), 618-6187.
31. Chen, X.; Liu, L.; Yu, P. Y.; Mao, S. S., Increasing Solar Absorption for Photocatalysis with Black Hydrogenated Titanium Dioxide Nanocrystals. *Science (American Association for the Advancement of Science)* **2011,** *331* (6018), 746-750.
32. Wrighton, M. S.; Ellis, A. B.; Wolczanski, P. T.; Morse, D. L.; Abrahamson, H. B.; Ginley, D. S., Strontium Titanate Photoelectrodes. Efficient Photoassisted Electrolysis of Water at Zero Applied Potential. *Journal of the American Chemical Society* **1976,** *98* (10), 2774-2779.
33. Zhang, M.; Pham, H. K.; Fang, Y.; Tay, Y. F.; Abdi, F. F.; Wong, L. H., The Synergistic Effect of Cation Mixing In Mesoporous $Bi_xFe_{1-x}VO_4$ Heterojunction Photoanodes for Solar Water Splitting. *Journal of materials chemistry. A, Materials for energy and sustainability* **2019,** *7* (24), 14816-14824.
34. Newhouse, P. F.; Guevarra, D.; Umehara, M.; Reyes-Lillo, S. E.; Zhou, L.; Boyd, D. A.; Suram, S. K.; Cooper, J. K.; Haber, J. A.; Neaton, J. B.; Gregoire, J. M., Combinatorial Alloying Improves Bismuth Vanadate Photoanodes via Reduced Monoclinic Distortion. *Energy & environmental science* **2018,** *11* (9), 2444-2457.
35. Newhouse, P. F.; Guevarra, D.; Umehara, M.; Boyd, D. A.; Zhou, L.; Cooper, J. K.; Haber, J. A.; Gregoire, J. M., Multi-Modal Optimization of Bismuth Vanadate Photoanodes via Combinatorial Alloying and Hydrogen Processing. *Chemical communications (Cambridge, England)* **2019,** *55* (4), 489-492.
36. Liu, H.; Nakamura, R.; Nakato, Y., Bismuth-Copper Vanadate $BiCu_2VO_6$ as a Novel Photocatalyst for Efficient Visible-Light-Driven Oxygen Evolution. *Chemphyschem* **2005,** *6* (12), 2499-2502.
37. Tsuji, I.; Kato, H.; Kobayashi, H.; Kudo, A., Photocatalytic H_2 Evolution Reaction from Aqueous Solutions over Band Structure-Controlled $(AgIn)_xZn_{2(1-x)}S_2$ Solid Solution Photocatalysts with Visible-Light Response and Their Surface Nanostructures. *Journal of the American Chemical Society* **2004,** *126* (41), 13406-13413.

38. Tsuji, I.; Kato, H.; Kobayashi, H.; Kudo, A., Photocatalytic H_2 Evolution under Visible-Light Irradiation over Band-Structure-Controlled $(CuIn)_xZn_{2(1-x)}S_2$ Solid Solutions. *The journal of physical chemistry. B* **2005,** *109* (15), 7323-7329.
39. Xing, C.; Zhang, Y.; Yan, W. E. I.; Guo, L., Band Structure-Controlled Solid Solution of $Cd_{1-x}Zn_xS$ Photocatalyst for Hydrogen Production by Water Splitting. *International journal of hydrogen energy* **2006,** *31* (14), 2018-2024.
40. Hassan, A.; Iqbal, T.; Tahir, M. B.; Afsheen, S., A Review on Copper Vanadate-Based Nanostructures for Photocatalysis Energy Production. *International journal of energy research* **2019,** *43* (1), 9-28.

CHAPTER 2

TUNING THE ELECTRONIC, OPTICAL AND PHOTOELECTROCHEMICAL PROPERTIES OF COPPER METAVANADATE VIA ALKALINE EARTH METAL SUBSTITUTION

ABSTRACT:

Here, we present a fundamental understanding of the effect of alkaline earth metal substitution on the optical, electronic, and photoelectrochemical (PEC) properties of copper metavanadate. Mixed compositions of $A_{0.1}Cu_{0.9}V_2O_6$ (A = Mg, Ca) photoanodes were synthesized via time and energy-efficient solution combustion (SCS) method. The effect of introducing alkaline earth metals on crystal structure, microstructure, electronic, and optical properties of copper metavanadates was investigated by powder x-ray diffraction (PXRD), scanning electron microscopy (SEM), diffuse reflectance spectroscopy (DRS), transmission electron microscopy (TEM) and Raman spectroscopy. PXRD patterns, TEM, and Raman scattering data showed that the polycrystalline powder samples were solid solutions of copper and alkaline earth metal metavanadates. DRS showed a decrease in the optical bandgap with Cu incorporation. In addition, the PEC properties exhibited a strong dependence on the alloy composition. These semiconductor samples are potential candidates for PEC water splitting, photocatalysis, phosphors, or photovoltaic devices.

2.1 INTRODUCTION

Due to the rise in energy demand caused by industrialization, there has been a need to explore other sources of sustainable and clean energy, such as photoelectrochemical (PEC) water splitting.[1] However, a major obstacle in this field has been the lack of efficient photoelectrodes that are both chemically stable and made of abundant elements, and that can operate under visible light irradiation.[2-4] Metal vanadates have been extensively studied experimentally as photoelectrode materials due to their unique physical properties and exceptional performance.[5, 6] Vanadate-based materials have favorable bandgap and diverse crystal structures suitable for solar water conversion.[7, 8]

The Cu-V-O system has shown potential application in solar water splitting, battery material, and display devices.[9-17] The solar water-splitting performance and optoelectronic properties of the Cu-V-O family of compounds are affected by various stoichiometries.[10, 18] α-CuV_2O_6, β- and α-$Cu_2V_2O_7$ and γ-$Cu_3V_2O_8$ have been synthesized via solution combustion method and it was observed that the copper lean α-CuV_2O_6 exhibits better photoactivity.[10] The PEC stability of α-$Cu_2V_2O_7$, β-$Cu_2V_2O_7$, γ -$Cu_3V_2O_8$, and $Cu_{11}V_6O_{26}$ was compared in three different electrolytes, and $Cu_{11}V_6O_{26}$ was found to have better stability.[15] Phase pure α-CuV_2O_6 prepared via solution combustion synthesis has recorded the highest photocurrent response in this family of compounds, reaching approximately 750 μA/cm^2 at 1.74 V versus RHE.[11]

In this study, we incorporated alkaline earth metals to explore copper vanadate solid solutions. The effect of cation addition on the crystal structure, electronic, optical and PEC properties of the metavanadates prepared via solution combustion synthesis have been investigated. While the formation of copper and alkaline earth metal solid solutions did not improve the PEC performance, previous reports on mixed cation system have shown better activity.[19] Using DFT calculations and

spectroscopic techniques, we show below how the optical bandgap and crystal structure of α-CuV_2O_6 can be modified upon incorporation of alkaline earth metals.

2.2 EXPERIMENTS AND CALCULATION METHODS

2.2.1 Materials. $Cu(NO_3)_2{\cdot}2.5H_2O$, (Alfa Aesar), $Mg(NO_3)_2{\cdot}6H_2O$ (99+%, Acros Organics), $Ca(NO_3)_2{\cdot}4H_2O$ (Certified ACS, Fisher Scientific), NH_4VO_3 (Alfa Aesar), $C_4H_6O_5$ (98%, Alfa Aesar), NH_4OH (Alfa Aesa), HCOONa (Kodak), H_3BO_3 (Fisher Scientific) and $Na_2B_4O_7{\cdot}10H_2O$ were used without further purification.

2.2.2 Synthesis. The metavanadates were prepared via solution combustion synthesis following the chemical reaction shown in Equation 1.

$$3M(NO_3)_2{\cdot}xH_2O_{(s)} + 6NH_4VO_{3\,(s)} + C_4H_6O_{5\,(s)} \rightarrow 3MV_2O_{6\,(s)} + 6N_{2\,(g)} + 4CO_{2\,(g)} + (15 + 3x)\,H_2O_{(g)} \quad (1)$$

where, M = Mg, Ca, Cu.

All the polycrystalline samples were prepared by solution combustion synthesis (SCS) according to the procedure from our previous report.[10] The end members MgV_2O_6, CaV_2O_6, CuV_2O_6 and the solid solutions $A_{0.1}Cu_{0.9}V_2O_6$ (A= Mg, Ca) were prepared by dissolving a stoichiometric amount of alkaline earth metal or copper nitrates, ammonium vanadate and DL-malic acid in a beaker containing water as per Table 2-1. After homogenizing the solutions, the mixture was placed in a preheated muffle furnace at around 300 °C for 5 – 10 min, where it was first dehydrated before ignition. All samples were annealed at 600 °C for 1 h in an alumina crucible to improve crystallinity and remove organic traces.

Table 2-1. The concentration of precursor mixtures for the synthesis of end members and solid solutions via SCS.

Sample	Precursor (M)				
	$Mg(NO_3)_2.6H_2O$	$Ca(NO_3)_2.4H_2O$	$Cu(NO_3)_2.6H_2O$	NH_4VO_3	$C_4H_6O_5$
MgV_2O_6	0.250	0.000	0.000	0.500	0.750
CaV_2O_6	0.000	0.250	0.000	0.500	0.750
$Mg_{0.1}Cu_{0.9}V_2O_6$	0.025	0.000	0.225	0.500	0.750
$Ca_{0.1}Cu_{0.9}V_2O_6$	0.000	0.025	0.225	0.500	0.750
CuV_2O_6	0.000	0.000	0.250	0.500	0.750

2.2.3 Physical Characterization. Samples were analyzed by powder X-ray diffraction recorded using a Bruker D8 advance instrument (Cu Kα radiation: λ = 1.5406 Å). The samples were measured at 40 kV and 40 mA over a 2θ range of 10 - 70° with a step size of 2θ = 0.002° and scan speed of 1° per minute. Phase analyses and Rietveld refinement of the PXRD data was carried out using GSAS-EXPGUI software package.[20] For structural characterization, Transmission Electron Microscopy (TEM) was carried out using Hitachi H-9500 instrument operating at an acceleration voltage of 300 kV and a LaB_6 filament. Scanning electron microscopy (SEM) and energy dispersive X-ray spectrometry (EDX) experiments were performed on a Hitachi S-3000 N FE scanning electron microscope equipped with a tungsten electron source and Thermo Scientific UltraDry^{TM} model EDX detector. Spectral data for elemental mapping were recorded at an accelerating voltage of 25 kV. Raman spectra of the samples were collected using Thermo scientific DXR3 Raman microscope equipped with 633 nm diode laser (He-Ne gas laser) at a power of 1 mW. Diffuse reflectance spectroscopy was carried out using a Varian Cary 500

instrument under diffuse reflectance mode and over the range of 350 – 800 nm. The absorption coefficient, α, was calculated from the Kubelka – Munk transformation (eq 2) of the DRS data.[21, 22]

$$\frac{\propto}{S} = \frac{(1-R)^2}{2R} \quad (2)$$

Here, α is the absorption coefficient, S is the scattering coefficient and R represents the reflectance. Optical bandgaps were estimated based on Tauc analyses presented in eq 3.[21-24]

$$h\nu = \propto (h\nu - E_g)^n \quad (3)$$

where E_g is the bandgap and n describes the nature of the electronic transition, i.e., n = ½ for direct allowed transition and n = 2 for indirect allowed transition.

X-ray photoelectron spectroscopy (XPS) was conducted on a Thermo XPS NEXSA instrument equipped with an Al Kα X-ray source. Inductively coupled plasma-atomic emission spectroscopy (ICP-AES) analysis was conducted using a Thermo iCap7600 instrument equipped with a radial view and ESI SC-2DX PrepFAST autosampler. Online dilution was carried out using the prepFAST system, and standards of Cu, Mg, Ca, and V with concentrations ranging from 0.5 ppm to 10 ppm were used to create calibration curves. A slight modification to the standard digestion method was required to dissolve the vanadium oxide precipitate, which involved the addition of 500 µL of concentrated hydrochloric acid and heating overnight at 65 °C.

2.2.4 Electrode Preparation and Photoelectrochemical Measurements. The electrode films were prepared by suspending 100 mg of the bulk powder in 20 mL of ethanol. The suspension was deposited on fluorine-doped tin oxide (FTO) by spray-coating using a previously reported procedure.[25] Electron microscopy and EDX were used to confirm elemental distribution, texture

and surface homogeneity. Photoelectrochemical (PEC) measurements were performed on a CH Instruments, Model CHI720C. The surface of the working electrodes was irradiated using A 400 W Xe-arc lamp (Newport) with an IR filter and a calibrated Si reference cell (Oriel) to achieve a measured light intensity of 1 sun (100 mW/cm^2). PEC measurements were carried out in a standard one-compartment three electrode electrochemical cell, where Ag/AgCl/3M NaCl was used as reference electrode, Pt wire as the counterelectrode and the vanadate film as the counter electrode. In this study, potential conversion to the reversible hydrogen electrode scale was determined according to eq 4.

$$E_{RHE} = E_{Ag/AgCl} + E^0_{Ag/AgCl(3M\ KCl)} + 0.0591pH \quad (4)$$

where $E^0_{Ag/AgCl(3M\ KCl)}$ = 0.209 V versus NHE at 25 °C.

Photocurrent measurements of the vanadate films were measured in a 0.1 M borate buffer electrolyte (pH = 8.0) using a potential scan of 5 mV/s sweep rate. In some cases, 4 M formate was added to the electrolyte as a hole scavenger. Front-side illumination under a manual chopper was used at intervals of 5 s.

2.2.5 Computational Methodology. Spin-polarized *ab initio* density functional theory calculations were performed as implemented of Quantum ESPRESSO package.[26, 27] To extend the Kohn-Sham equations, a plane wave basis set with kinetic energy cut-off of 50 Ry for electronic wave function was employed. The interactions between the valence electrons and ionic core were described using projector-augmented wave, PAW potentials.[28]. The revised Perdew-Burke-Ernzerhof (PBE) functional within the generalized gradient approximation (GGA) for solids, namely the PBEsol functional was utilized to describe the exchange and correlation.[29] Brillouin zone was sampled using the Monkhorst–Pack k-point mesh.[30] Geometry optimization of CaV_2O_6 was performed using an unshifted k-point mesh of $4 \times 12 \times 6$, while the geometry

optimization of bulk CuV_2O_6 and MgV_2O_6 utilizes an unshifted k-point mesh of 4 × 10 × 6. To calculate the projected density of states (PDOS), a denser k-point grid was employed. To aid convergence, Marzari-Vanderbilt[31] cold smearing function with a width of 0.005 Ry was used. For geometry optimization, Hellmann-Feynman forces[32] were employed to allow relaxation of all atoms inside a unit cell until the residual forces on all the constituent atoms decrease below 0.01 eV/Å. It can be noted that DFT has a well-known limitation of underestimating the self-interaction correction (SIC) of strongly correlated electrons in highly localized orbitals. Therefore, to better describe the localization of the 3*d* electrons of Cu and V, the DFT + U framework[33] was employed in this study. Controlling the SIC, which enhances the depiction of geometric, electronic, and magnetic structures, was mainly achieved by manipulating the on-site Coulombic interaction term U and exchange parameter J within this framework. In this sense, we have chosen the values of U as 3.0 and 3.5 eV, respectively, for the Cu and V 3*d* orbitals, with a fixed value of J set at 1 eV aiming towards a better agreement with the experimentally observed lattice parameters, band gaps, and magnetic ordering of the investigated systems. We note that analogous U values have been employed for Cu and V 3*d* orbitals in many compounds, as previously reported in the literature.[11, 34, 35] These calculations were performed by our collaborator, Dr. Abhishek Kumar Adak.

2.3 RESULTS AND DISCUSSION

2.3.1 Crystal Structures and Characterization. MV_2O_6 (M = Mg, Ca, Cu) crystallize in brannerite (monoclinic, m-brannerite and triclinic, t-brannerite) and pseudobrannerite (p-brannerite) structure type.[36, 37] MgV_2O_6 exhibits m-brannerite structure (Figure 2-1a) consisting of MgO_6 octahedra that forms $(Mg\text{-}O)_n$ chain along the b-axis and edge-shared VO_6 octahedra which form infinite anionic layers along the ac-plane.[36] The vanadium ions have 5+1 coordination due to

one of the V-O bond lengths being much longer than the others in the VO_6 octahedra.[36] MgO_6 octahedra are sandwiched between layer of $(VO_6)_n$ to form infinite chains along the b-axis.[36] M-brannerite structure may transform to p-brannerite structure by the rotation of $(V\text{-}O)_n$ zig-zag chain around the b-axis, such that one of the V-O bond (most loosely bonded) will elongate and change the coordination of vanadium to trigonal bipyramid.[36] Figure 2-1b shows p-brannerite structure of CaV_2O_6 which consists of CaO_6 and VO_5 polyhedra, Additionally, CuV_2O_6 adopts a t-brannerite structure (Figure 2-1c) which is a distorted m-brannerite structure that is stabilize by the Jahn-Teller effect.[36-38] CuV_2O_6 consists of CuO_6 and VO_6 octahedral layers. At temperature above 625 °C, CuV_2O_6 transforms from t-brannerite to m-brannerite.[36, 38]

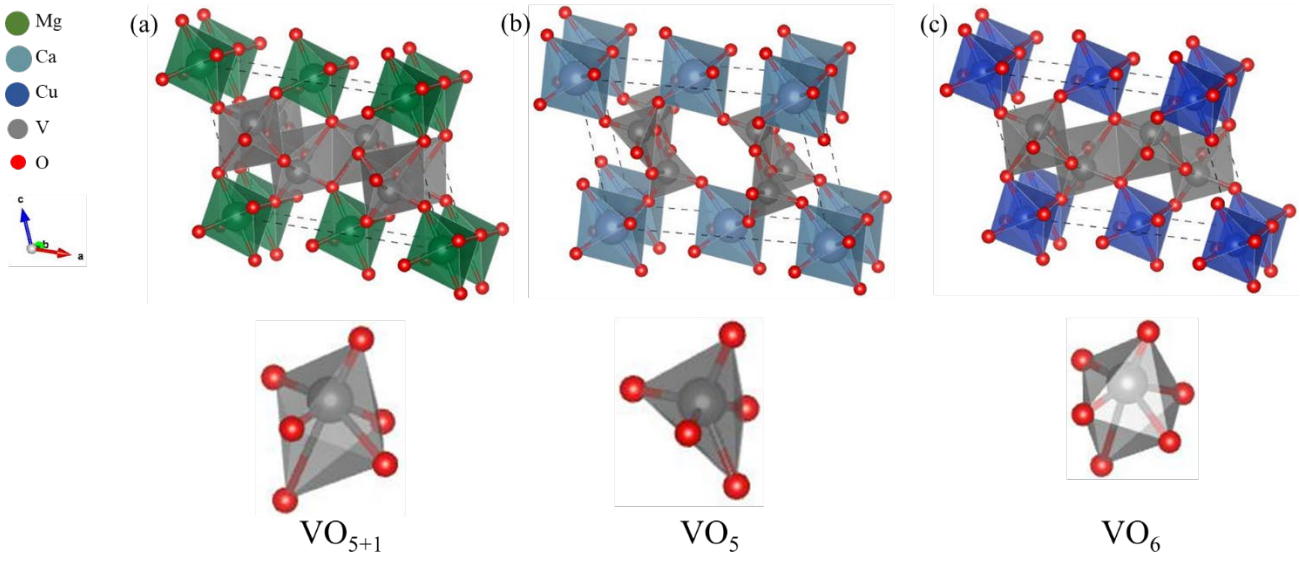

Figure 2-1. Crystal structure for (a) MgV_2O_6, (b) CaV_2O_6 and (c) CuV_2O_6 with their respective VO_n polyhedral units.

Table 2-2 shows the purity and composition of the samples obtained from SCS as evaluated using the ICP-AES method. The sample compositions matched well with the expected values from the precursor amounts added, including both the end members and the solid solutions, considering the experimental uncertainty. The combustion synthesis yields were consistently high, with a range

of 95% to 98% for all samples. These findings suggest that SCS can produce phase-pure products, which is consistent with our previous reports on the Cu-V-O system.[10, 11]

Table 2-2. Comparison between ICP-AES assays with precursor added during SCS.

Sample	Experimental ratio			Precursor added		
	Cu/2V	Mg/2V	Ca/2V	Cu/2V	Mg/2V	Ca/2V
MgV_2O_6	0.00	1.05	0.00	0.00	1.00	0.00
CaV_2O_6	0.00	0.00	1.02	0.00	0.00	1.00
CuV_2O_6	1.05	0.00	0.00	1.00	0.00	0.00
$Mg_{0.1}Cu_{0.9}V_2O_6$	0.95	0.11	0.00	0.90	0.10	0.00
$Ca_{0.1}Cu_{0.9}V_2O_6$	0.96	0.00	0.11	0.90	0.00	0.10

The X-ray powder diffraction patterns of the synthesized compounds are shown in Figure 2-2. The X-ray diffractograms of the pristine MgV_2O_6, CaV_2O_6, and CuV_2O_6 showed they adopt m-berrenerite, p-berrenerite and t-berrenerite structures, respectively, which is consistent with previous reports.[38-40] The Rietveld refinement (Figure 2-3) confirms that MgV_2O_6 and CaV_2O_6 adopt a monoclinic structure with $C2/m$ space group symmetry while CuV_2O_6 adopts a triclinic (space group, $P\bar{1}$) structure. Table 2-3 shows the summary of the Rietveld refinements with a goodness of fit, χ^2, between 1.06 - 1.07. Furthermore, the effect of the alkaline earth metal substitution on the local structure, $A_{0.1}Cu_{0.9}V_2O_6$ (A = Mg, Ca) was investigated by X-ray diffraction (Figure 2-2). A triclinic (space group, $P\bar{1}$) structure was maintained for the $A_{0.1}Cu_{0.9}V_2O_6$ solid solutions. As expected, a shift in the diffraction peak was observed with substitution of copper by the alkaline earth metal, indicating the formation of solid solution. No

obvious peaks from either monoclinic MgV_2O_6 or CaV_2O_6 were observed in the PXRD pattern for $A_{0.1}Cu_{0.9}V_2O_6$, also suggesting complete incorporation of Mg or Ca into the CuV_2O_6 lattice. The experimental diffraction pattern of the solid solutions was refined using the Rietveld method (Figure 2-3). During the refinement, the occupancy of the mixed A/Cu site (2a) was allowed to "float", and a best fit was observed when 10% of the 2a Wyckoff sites was occupied by the alkaline earth metal. The lattice parameters of the solid solutions slightly increased with alkaline earth metal substitution, suggesting the substitution of the small copper atoms by larger alkaline earth metal atoms within the CuV_2O_6 lattice. Refinement parameters are listed in Table 2-3. A small amount (4.4%) of β-$Cu_2V_2O_7$ impurity was detected in $Mg_{0.1}Cu_{0.9}V_2O_6$.

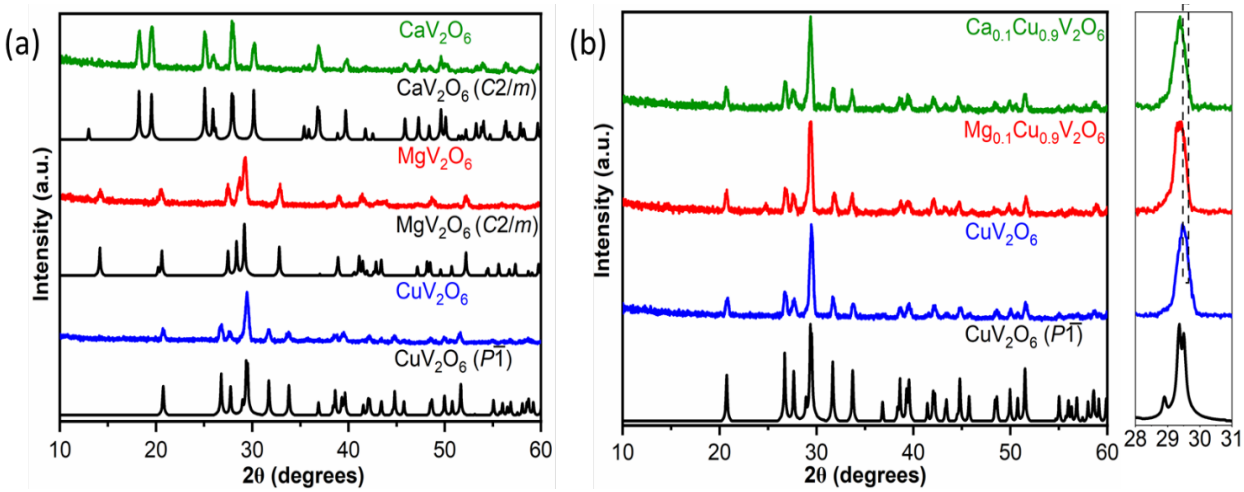

Figure 2-2. Comparative XRD patterns: (a) experimental for the end members and their respective reference in black and (b) the solid solutions $A_{0.1}Cu_{0.9}V_2O_6$ and CuV_2O_6.

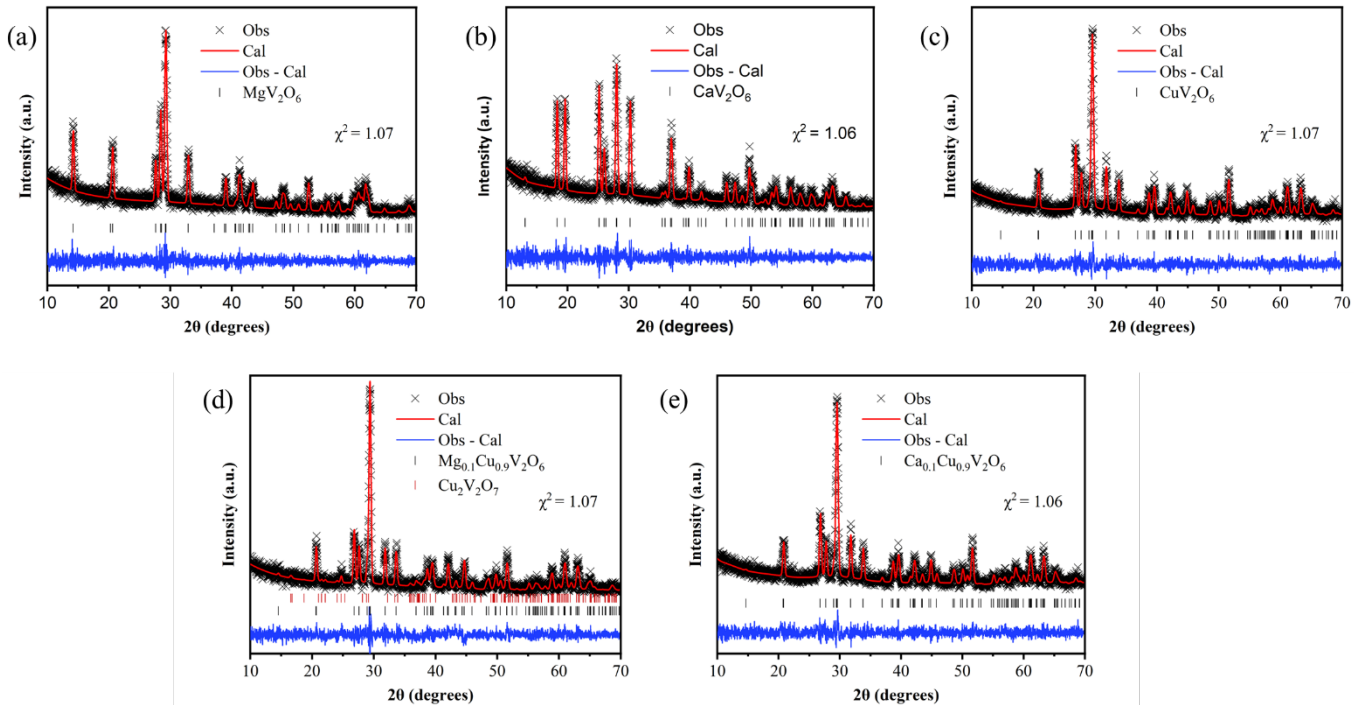

Figure 2-3. Rietveld refinement plot from PXRD data for (a-c) the end members and (d, e) the solid solutions $A_{0.1}Cu_{0.9}V_2O_6$.

Table 2-3. Refinement parameters for the end members CuV_2O_6, MgV_2O_6, CaV_2O_6 and solid solutions $A_{0.1}Cu_{0.9}V_2O_6$.

Sample	a (Å)	b (Å)	c (Å)	α (°)	β (°)	γ (°)	V (Å^3)	χ^2
MgV_2O_6	9.2906(7)	3.4899(3)	6.7342(4)	90.000	111.654(5)	90.000	202.939	1.07
CaV_2O_6	10.0629(5)	3.6734(1)	7.0349(2)	90.000	104.849(3)	90.000	251.367	1.06
CuV_2O_6	9.1732(3)	3.5540(3)	6.4817(2)	92.286(1)	110.323(3)	91.771(3)	197.774	1.07
$Mg_{0.1}Cu_{0.9}V_2O_6$	9.1809(3)	3.5465(1)	6.5011(1)	92.029(2)	110.485(2)	91.475(2)	197.991	1.07
$Ca_{0.1}Cu_{0.9}V_2O_6$	9.1819(3)	3.5539(3)	6.5035(3)	92.156(1)	110.274(3)	91.678(3)	198.726	1.06

Figure 2-4 shows selected area electron diffraction (SAED) patterns from the solid solutions and the end members. To further confirm alloy formation and phase purity, d-spacing values from SAED patterns of the solid solutions were compared with d-spacings from PXRD data (Table 2-4). It was observed from the result that the d-spacing values from the SAED patterns were in good agreement with the d-spacing values obtained via Rietveld refinement of the PXRD data.

Furthermore, the SAED pattern of the solid solutions showed the regular triclinic symmetric diffraction pattern like for CuV_2O_6.

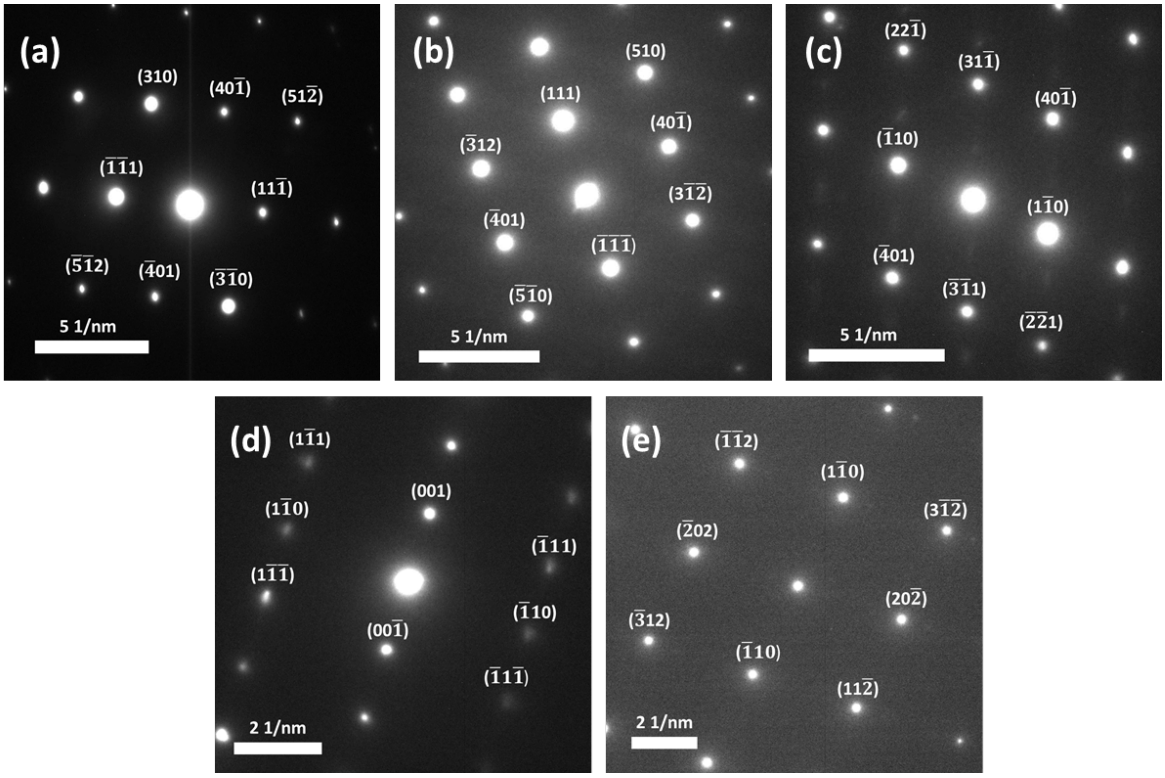

Figure 2-4. SAED patterns for (a-c) the end members MgV_2O_6, CaV_2O_6, CuV_2O_6, and (d, e) the solid solutions $Mg_{0.1}Cu_{0.9}V_2O_6$ and $Ca_{0.1}Cu_{0.9}V_2O_6$. The SAED spots were indexed to the corresponding unit cells illustrated in Figure 1-1.

Table 2-4. Comparison of estimated d-spacing values from SAED and PXRD data for the end members CuV_2O_6, MgV_2O_6, CaV_2O_6 and solid solutions $A_{0.1}Cu_{0.9}V_2O_6$.

Sample	d-spacing (Å) SAED	d-spacing (Å) XRD	Plane
MgV_2O_6	3.05	3.060	(11$\bar{1}$)
	2.44	2.319	(40$\bar{1}$)
	2.22	2.221	(310)
	1.69	1.615	(51$\bar{2}$)
CaV_2O_6	3.022	2.961	(111)
	2.461	2.500	(40$\bar{1}$)

	2.152	2.186	$(\bar{3}12)$
	1.733	1.718	(510)
CuV_2O_6	3.25	3.330	$(1\bar{1}0)$
	2.37	2.291	$(40\bar{1})$
	2.35	2.277	$(31\bar{1})$
	1.64	1.632	$(22\bar{1})$
$Mg_{0.1}Cu_{0.9}V_2O_6$	6.161	6.083	(001)
	3.331	3.322	$(\bar{1}10)$
	3.085	3.035	$(\bar{1}11)$
	2.812	2.809	$(1\bar{1}1)$
$Ca_{0.1}Cu_{0.9}V_2O_6$	3.272	3.333	$(1\bar{1}0)$
	2.982	3.033	$(20\bar{2})$
	2.403	2.442	$(\bar{1}\bar{1}2)$
	2.048	2.086	$(3\bar{1}\bar{2})$

Figure 2-5 shows representative SEM images of the end members and solid solutions $A_{0.1}Cu_{0.9}V_2O_6$ thin films. The average particle size for the solid solutions $A_{0.1}Cu_{0.9}V_2O_6$ and end members ranged between 2 – 10 μm. Energy dispersive X-ray (EDX) spectroscopy was used to measure the elemental compositions of the solid solutions $A_{0.1}Cu_{0.9}V_2O_6$ and the EDX spectrum is shown in Figures 2-6 and 2-7. The average Mg/Cu and Ca/Cu ratio was determined to be 0.094 and 0.090, respectively, in good agreement with the theoretical stoichiometric value, 0.111 for the chemical formula, $A_{0.1}Cu_{0.9}V_2O_6$. There was uniform distribution of the elements over the various polycrystalline sample grains as shown in the EDX elemental maps in Figure 2-8.

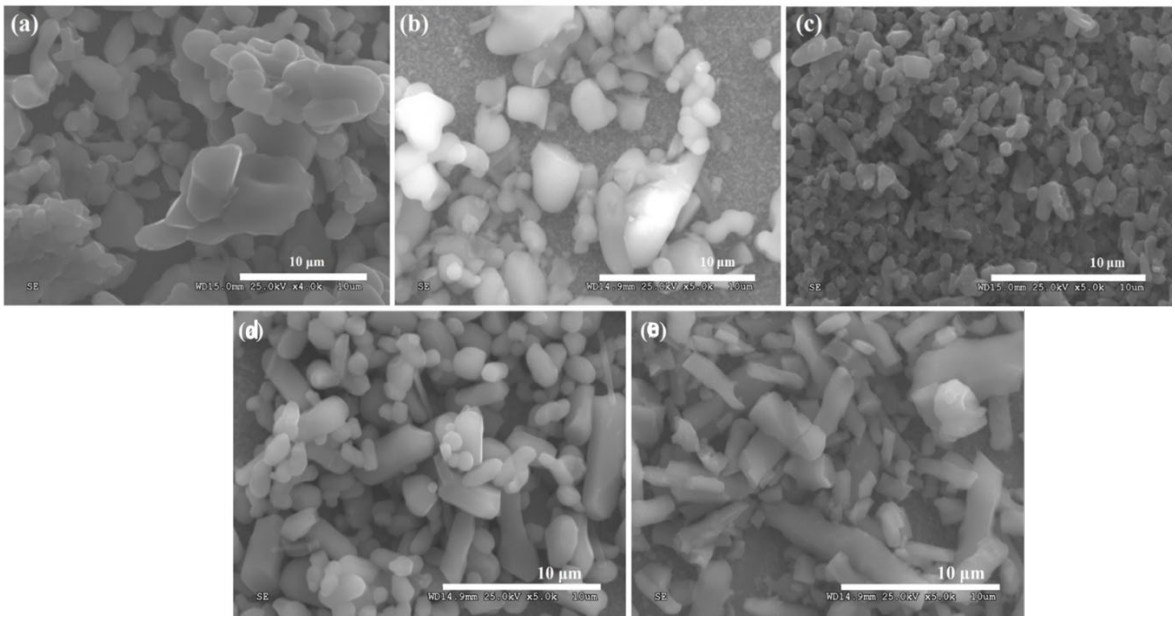

Figure 2-5. SEM images for the end members (a) MgV_2O_6, (b) CaV_2O_6 and (c) CuV_2O_6, and the solid solutions (d) $Mg_{0.1}Cu_{0.9}V_2O_6$ and (e) $Ca_{0.1}Cu_{0.9}V_2O_6$.

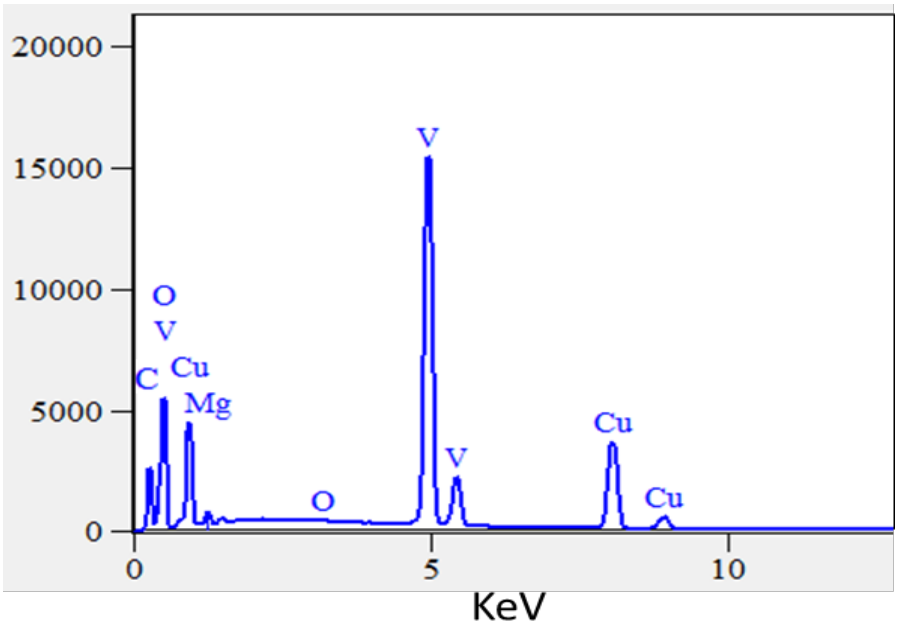

Figure 2-6. Representative EDX spectrum for $Mg_{0.1}Cu_{0.9}V_2O_6$.

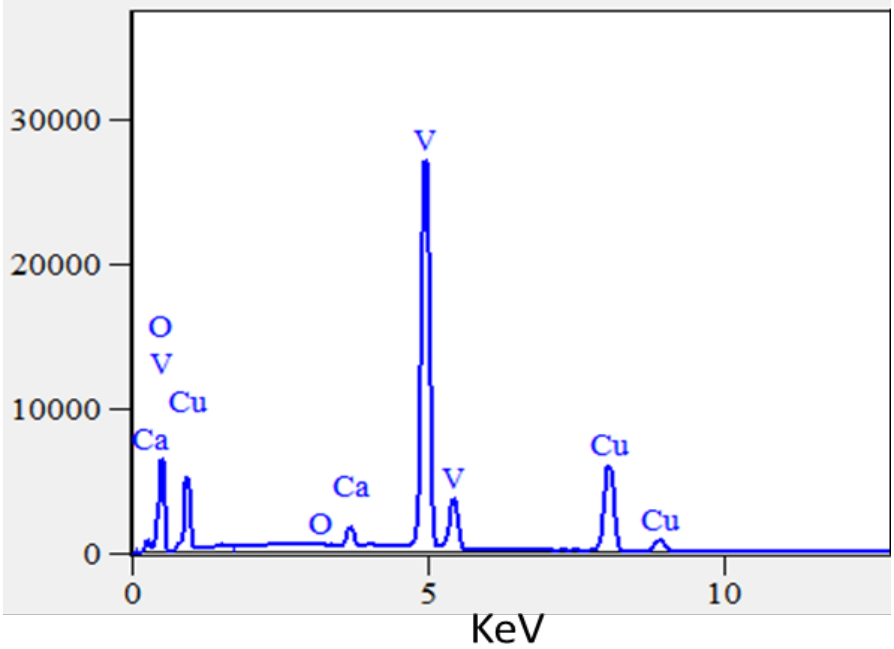

Figure 2-7. EDX spectrum for $Ca_{0.1}Cu_{0.9}V_2O_6$.

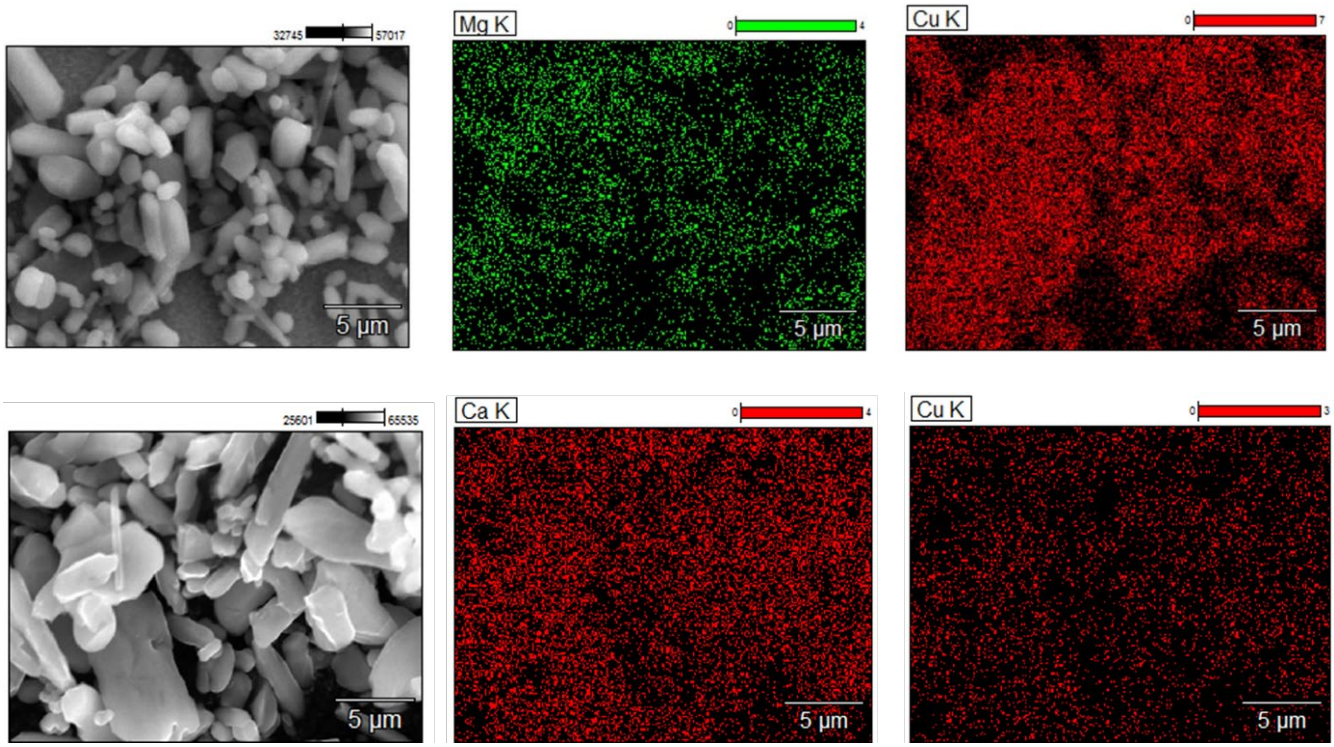

Figure 2-8. EDX maps for $Mg_{0.1}Cu_{0.9}V_2O_6$ (top) and $Ca_{0.1}Cu_{0.9}V_2O_6$ (bottom).

Raman spectra of the end members CuV_2O_6, MgV_2O_6 and CaV_2O_6, and that of the solid solutions $Mg_{0.1}Cu_{0.9}V_2O_6$ and $Ca_{0.1}Cu_{0.9}V_2O_6$ are presented in Figure 2-9. The observed Raman bands were in good agreement with previous reports[11, 41] and no impurity peaks were observed, indicating phase purity. The Raman bands observed in the region 750 - 950 cm^{-1} were assigned to the stretching vibrations of V−O in VO_n polyhedra, whereas the bands observed at 400 – 750 cm^{-1} were assigned to symmetric and asymmetric V−O bending vibrations.[11, 41] Raman bands below 400 cm^{-1} may be assigned to Cu/Mg/Ca−O vibrations and lattice phonon modes.[11, 41] While the general shape of the peaks is similar for CuV_2O_6 and $A_{0.1}Cu_{0.9}V_2O_6$ solid solutions, there was noticeable peak shift to the right at the higher frequency range (750 – 950 cm^{-1}) upon substitution of Cu by alkaline earth metals, suggesting distortion in VO_6 octahedra due to bond length contraction of axial V−O (Figure 2-9b).

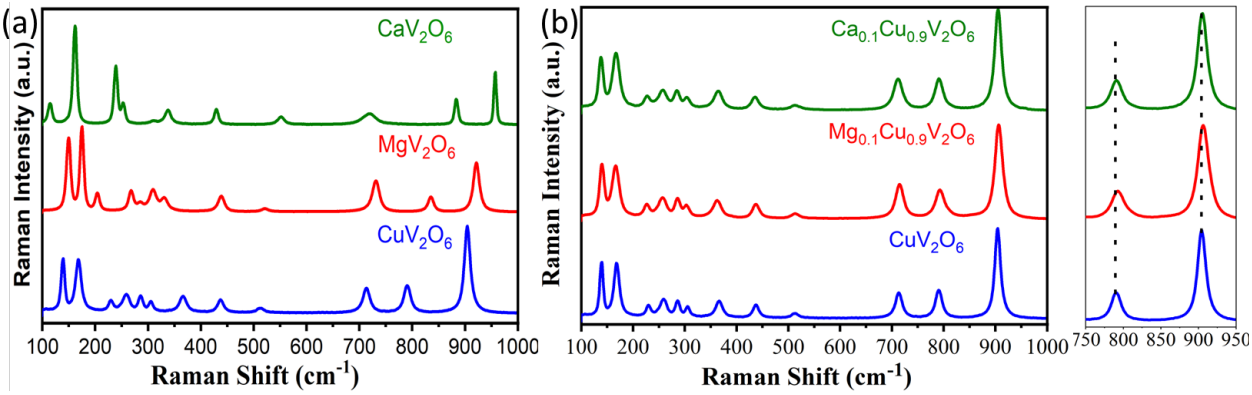

Figure 2-9. Room temperature Raman spectra of (a) end members CuV_2O_6, MgV_2O_6, CaV_2O_6 and (b) solid solutions $A_{0.1}Cu_{0.9}V_2O_6$.

X-ray photoelectron spectra were collected to gain insight into the surface chemical composition and valence states of Mg, Ca, Cu, and V. The binding energy range for the core level XPS spectra of Mg 1*s*, Ca 2*p*, and Cu 2*p* appeared at 1300 – 1308, 340 – 360, and 925 – 965 eV, respectively, as seen in Figures 2-10a-c. The divalent state of Mg was confirmed by the presence

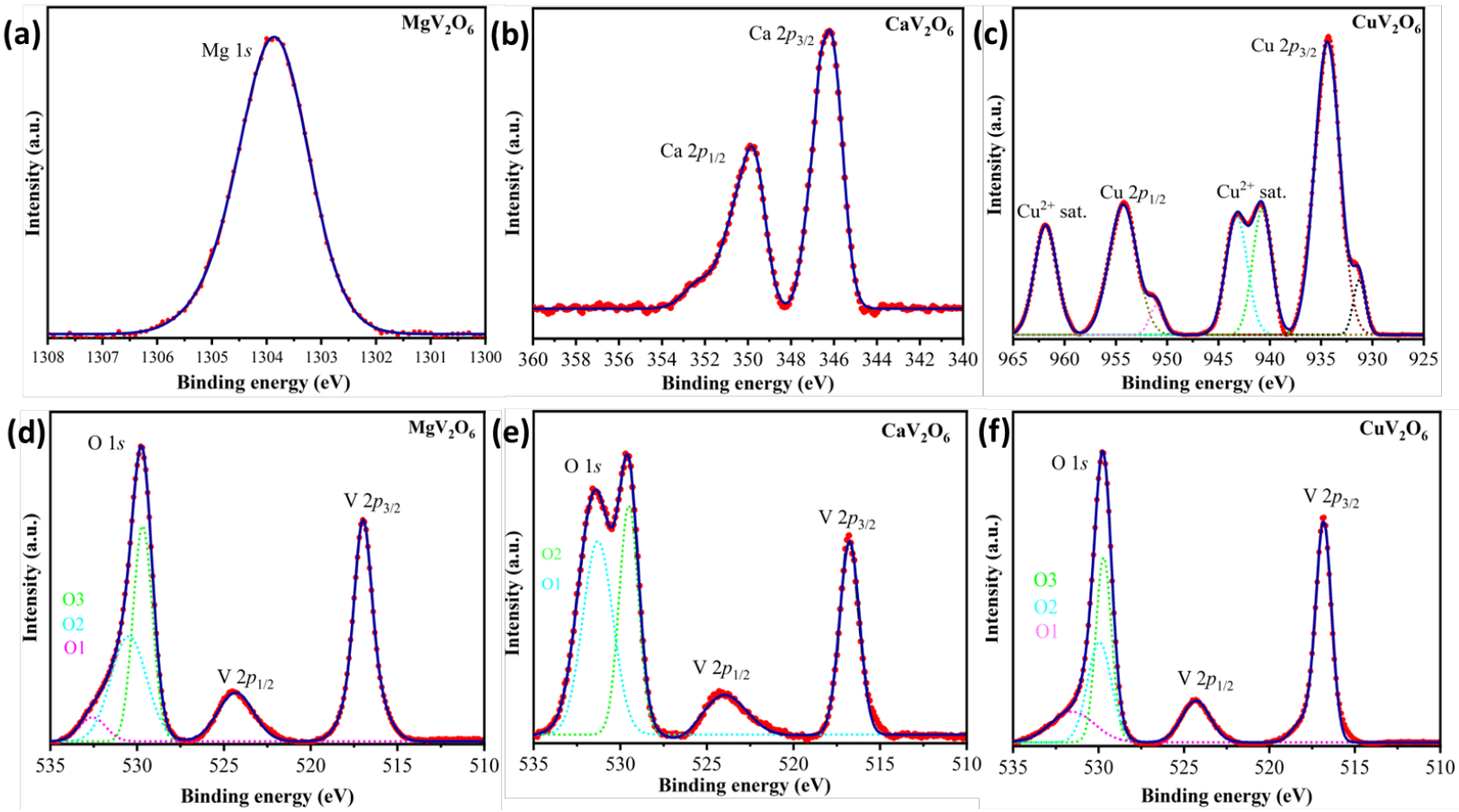

Figure 2-10. High resolution XPS spectra showing (a) Mg 1*s* in MgV_2O_6, (b) Ca 2*p* in CaV_2O_6, (c) Cu 2*p* in CuV_2O_6 and (d-f) O 1*s* and V 2*p* in MgV_2O_6, CaV_2O_6 and CuV_2O_6, respectively. In selected cases, peak deconvolutions are shown.

of a XPS peak at 1303.8 eV in good agreement with a previous report on MgO.[42] According to Figure 2-10b, the Ca 2*p* core level XPS spectra revealed two peaks at 346.2 and 349.8 eV that correspond to Ca $2p_{3/2}$ and $2p_{1/2}$ with binding energy difference of 3.6 eV, attributed to spin-orbital, confirms that Ca is in a divalent state.[43] Figure 2-10c revealed that the Cu $2p_{3/2}$ and $2p_{1/2}$ spectra of CuV_2O_6 split each into two peaks, 931.6/934.4 eV and 951.4/954.3 eV, respectively. This peak splitting is attributed to the presence of Cu^+ ions, which serve to balance the charge associated with oxygen vacancies.[12, 44] The presence of Cu^{2+} was confirmed by the appearance of peak at 934.4 and 954.3 eV.

The binding energy range for V 2*p* and O 1*s* in MgV_2O_6, CaV_2O_6, and CuV_2O_6, is between 510 – 535 eV as depicted in Figures 2-10 d-f. All the three end members have two separate peaks for V $2p_{3/2}$ and V $2p_{1/2}$ at 517 and 524.4 eV, respectively, which confirmed the presence of V^{5+}.[15] In the XPS spectra of the end members, the O 1*s* peak is split into three sub-peaks due to the vanadate containing oxygen atoms located at three different atomic sites. These sub-peaks, seen at 529.7, 530.4, and 532.5 eV, correspond to the O atom bonded to V and Mg/Ca/Cu, as well as water that is chemically adsorbed.[44, 45] Unlike MgV_2O_6 and CuV_2O_6, CaV_2O_6 has an extra peak that deviate from ideal O lattice, suggesting the presence of oxygen defects in the lattices as previously reported.[45]

Finally, Figures 2-11a-f show the deconvoluted peaks of the solid solutions, based on the high resolution XPS spectra collected for O 1*s*, Mg 1*s*, Ca 2*p*, Cu 2*p*, and V 2*p*. Similar chemical state and bonding environment for the elements that were observed in the end members were also seen in the solid solutions. The chemical state and bonding environment for the elements in the end members were also found in the solid solutions, suggesting they both have similar features.

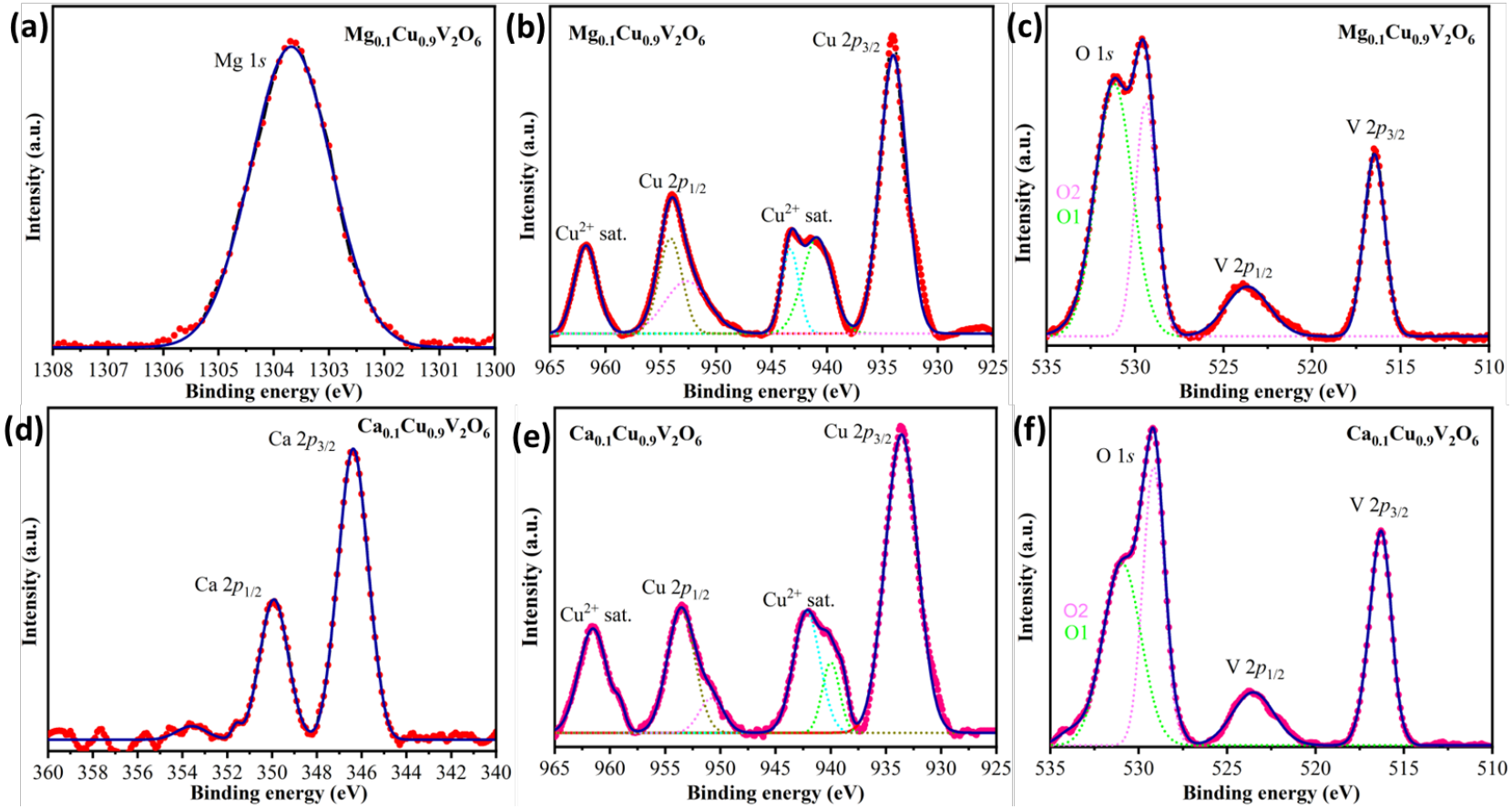

Figure 2-11. High resolution XPS spectra showing (a-c) Mg 1*s*, Cu 2*p,* O 1*s* and V 2*p* in $Mg_{0.1}Cu_{0.9}V_2O_6$, and (d-f) Ca 2*p,* Cu 2*p,* O 1*s* and V 2*p* in $Ca_{0.1}Cu_{0.9}V_2O_6$, respectively. In selected cases, peak deconvolutions are also shown.

2.3.2 Electronic and Optical Behavior.

Geometry optimization. Geometry optimization was performed on the conventional unit cell of bulk CuV_2O_6, MgV_2O_6, and CaV_2O_6, which consists of 18 atoms. Table 2-5 shows that the DFT-optimized lattice parameters align well with the experimentally observed values. However, it should be emphasized that the optimized lattice parameters for CaV_2O_6 were slightly over-estimated in comparison to the experimental value. This discrepancy may be attributed to the utilization of the same Hubbard U value for the 3*d* orbital of V atoms in all three complexes, despite the presence of VO_6 octahedral in CuV_2O_6 and MgV_2O_6 and VO_5 polyhedral in CaV_2O_6. U value is highly environment-specific inside a crystal and varies with the change in coordination geometry of an atom which may have played a role in the slight discrepancy in reproducing the lattice parameter of CaV_2O_6. Furthermore, to investigate the relative strength of different magnetic coupling between Cu atoms within a conventional unit cell, we have considered both ferromagnetic (FM) and antiferromagnetic (AFM) coupling. Our study reveals that there exists a discernible disparity in the total energy between the lowest energy AFM and FM structures, which amounts to 5.6 meV/Cu atom, demonstrating a proclivity towards AFM coupling. This finding suggests that the magnetic coupling within the Cu atoms is relatively weak which is in good agreement with previous experimental and theoretical observations where the system exhibits paramagnetic behaviour under ambient conditions. Consequently, only the AFM coupling between two neighbouring Cu atoms was considered for all forthcoming DFT computations.

To investigate the effect of 10% doping of Cu atoms with Mg and Ca, a $1 \times 5 \times 1$ supercell of CuV_2O_6 was considered for the substitution of a Cu atom with either Mg or Ca. Following the atomic substitution, structural optimization was performed, wherein the optimized lattice parameters were determined and tabulated. These parameters were in good agreement with the

Table 2-5. Comparison between experimental and calculated (1 x 5 x 1 supercell) unit cell parameters.

Sample		a (Å)	b (Å)	c (Å)	α (°)	β (°)	γ (°)
MgV_2O_6	Expt.	9.2906	3.4899	6.7342	90.000	111.654	90.00
	DFT	9.2517	3.4980	6.6344	90.000	113.789	90.000
CaV_2O_6	Expt.	10.0629	3.6734	7.0349	90.000	104.849	90.000
	DFT	10.3197	3.6370	7.1350	90.000	102.871	90.000
CuV_2O_6	Expt.	9.1732	3.5540	6.4817	92.286	110.323	91.771
	DFT	9.1549	17.8475	6.4089	93.533	111.653	92.037
$Mg_{0.1}Cu_{0.9}V_2O_6$	Expt.	9.1809	3.5465	6.5011	92.029	110.485	91.475
	DFT	9.1598	17.8147	6.4292	93.307	111.802	91.848
$Ca_{0.1}Cu_{0.9}V_2O_6$	Expt.	9.1819	3.5539	6.5035	92.156	110.274	91.678
	DFT	9.1756	17.8483	6.4689	93.479	111.761	91.719

values obtained from experimental measurements. Furthermore, substitution of a Cu atom into 5 × 1 × 1 and 1 × 1 × 5 supercells of CuV_2O_6 also results in a doping level of 10%. However, the deviation in total energies assessed through DFT calculations between these two and the 1 × 5 × 1 is less than 1 meV/Cu-atom. Therefore, we have considered the 1 × 5 × 1 supercell of CuV_2O_6 to reduce the interaction between two doping sites by maximizing their distances in all three directions. Similarly, we have also considered the 12.5% doping of Cu-atoms by investigating various AFM magnetic couplings between two neighboring Cu atoms in a 1 × 2 × 2 supercell of $Mg_{0.12}Cu_{0.88}V_2O_6$. From the total energies obtained through DFT calculations, we have determined

that the variation in formation energy between 10% and 12.5% doping amounts to only 12 meV/Cu doping site. Consequently, the scenario involving 12.5% doping is more energetically favorable. The net magnetic moment as obtained from DFT is 1 μ_B/cell for both 10% and 12.5% doping. It is worth mentioning that considering different AFM couplings in 12.5% doping scenario doesn't significantly affect the formation energy or magnetic moment. Therefore, to conduct our DFT calculations, we used a 10% doped 1 × 5 × 1 supercell of CuV_2O_6.

In this study, the electronic properties of bulk systems have been investigated using DFT. The electronic band structure in an antiferromagnetically coupled 1 × 5 × 1 supercell of bulk CuV_2O_6 was shown in Figure 2-12a while the calculated orbital PDOS of CuV_2O_6 was illustrated in Figure 2-12b. As the AFM-coupled Cu atoms lead to net zero magnetic moments, we obtain a symmetric band structure for both spin channels. Thus, in Figure 2-12a, we have presented the band structure originating from one spin channel exclusively. Further, we noted that a denser k-point mesh was required to capture the O 2*p* states near the Fermi level. It can be observed from the PDOS plot as displayed in Figure 2-12b that hybridized Cu 3*d* and O 2*p* orbitals primarily contribute to the top of the valance band maxima (VBM). The hybridization of Cu *3d* and O *2p* also increases the dispersion at the VBM, thereby presenting an opportunity to reduce the effective mass of the hole/positive charge carriers and hence, improving their mobility. In addition, a midgap state was observed in the band structure which agrees with the previous study.[11] These empty midgap states are primarily Cu 3*d* e_g states hybridized with O *2p* orbitals. In addition, the bottom of the conduction band was mainly occupied by V 3*d* orbitals, which have a minor or negligible contribution from O 2*p* and Cu 3*d* orbitals. This further evidence the observation of hybridization at valance band maxima, midgap state, and conduction band minima. From these results, we found CuV_2O_6 to be an indirect band gap semiconductor with a gap of 1.84 eV, which agrees well with

the experimental findings. In an earlier study, while investigating the chemical stability of $CuWO_4$ for PEC water oxidation, the presence of a midgap electronic state on the surface of $CuWO_4$ was observed through electrochemical impedance spectroscopy.[34] Such midgap states may play a crucial role in determining the hole transfer rate for water oxidization in spite of the fact that no conclusive evidence was found on whether the midgap state results from intrinsic Cu 3*d* states or photo-induced water oxidation intermediate species. Another study examined the electronic properties of bulk $CuWO_4$ using DFT and reported the presence of midgap states.[35] In this study, the authors performed DFT, DFT + U, and hybrid DFT calculations to investigate the PDOS and electronic band structure of the bulk system. The DFT method failed to reproduce the position of the midgap state and underestimated the band gap. On the other hand, DFT + U method could predict the band gap more accurately, but with a displacement of midgap states from the Fermi level toward the conduction band minima. In contrast, the hybrid calculations gave a better match with the experimental band gap and the mid-gap state was observed a little above the Fermi level.

The electronic band structure and calculated orbital PDOS of MgV_2O_6 and CaV_2O_6 are presented in Figures 2-12c - f. We have applied Hubbard correction on V 3*d* orbital which has led to the localization of V 3*d* orbitals at conduction bands. We note that bulk MgV_2O_6 and CaV_2O_6 systems are not magnetic. Further, Figures 2-12c - f indicate that both compounds have almost similar electronic structures. The slight variation in band dispersion near the VBM and CBM may be due to the presence of VO_6 octahedral in MgV_2O_6 and VO_5 polyhedral in CaV_2O_6. The conduction band and valence band are primarily derived from the V 3*d* and O 2*p* orbitals due to the splitting of the VO_6 octahedral and VO_5 polyhedral crystal field, as shown in the corresponding band structure plots. The DOS near the Fermi level is mainly made up of V 3d and O 2p states,

suggesting a significant interaction between these two elements. The s-block elements Mg and Ca have very little contribution in the electronic states near the Fermi level. We found MgV_2O_6 and CaV_2O_6 to be indirect band gap semiconductors with a gap of 2.68 eV and 2.85 eV, respectively, which agrees well with the experimental observation.

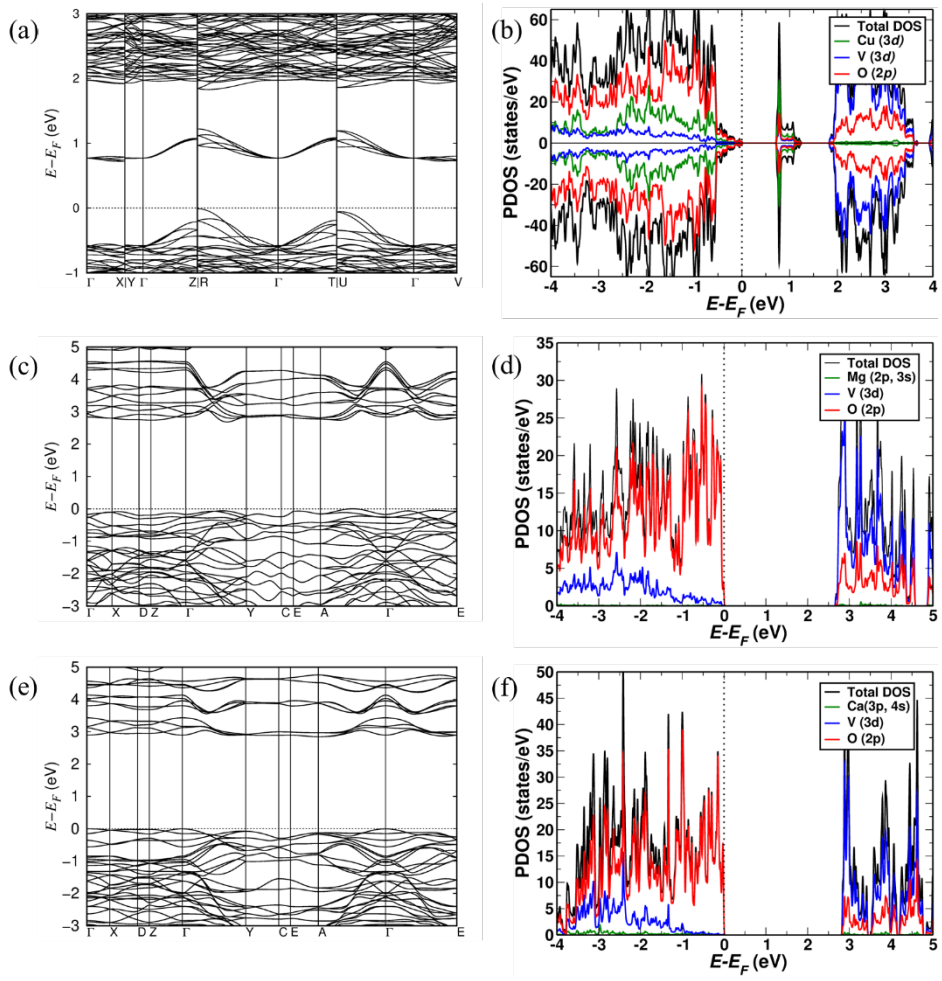

Figure 2-12. The electronic band structure and projected density of states (PDOS) for the bulk (a, b) CuV_2O_6, (c, d) MgV_2O_6 and (e, f) CaV_2O_6 have been calculated in a 1 x 5 x 1 supercell. The black line represents the total density of states, while the green line displays the projection on Cu 3*d* orbital, Mg 3*s* and 2*p* orbitals, and Ca 4*s* and 3*p* orbitals for the respective compounds. Furthermore, the blue line represents the V 3*d* orbital, and the red line represents the O 2*p* orbital. It is essential to note that for the band structure of CuV_2O_6, only one spin channel was shown as both spin down and up channels have the same band features.

Figures 2-13a - d show the electronic band structure of both spin-up (red) and spin-down (black) channels for $Mg_{0.1}Cu_{0.9}V_2O_6$ and $Ca_{0.1}Cu_{0.9}V_2O_6$ as well as the calculated orbital PDOS, which were obtained by the substitution of one Cu atom out of ten from an AFM coupled 1 × 5 × 1 supercell of bulk CuV_2O_6. Upon substitution of the Cu atom with elements from the s-block, the system obtains a net non-zero magnetic moment because of the presence of an odd number of Cu atoms in a supercell. As expected from the PDOS plots of bulk MgV_2O_6 and CaV_2O_6, we don't observe the contribution of Mg 3*s* and 2*p* orbitals and Ca 4*s* and 3*p* orbitals near the Fermi level. We also don't observe change in the midgap state as it is primarily populated by Cu 3*d* states. As the systems are 10% doped, the PDOS and the band structure look similar to what is observed in Figures 2-12a and b for undoped bulk CuV_2O_6. The band dispersion of the down-spin channel in Figures 2-13a and c was similar to the band dispersion observed in Figure 2-12a. In contrast, we notice a slightly modified band dispersion in the spin-up channel near VBM and CBM. As we know the states near VBM are of O 2*p* orbitals, the modification in band dispersion (near high symmetry point U) arises due to doping of Mg and Ca atoms which results in changing the hybridization of Cu-O bonding environment. Similarly, the change in the vanadium 3*d* octahedral environment due to doping leads to further flattening of the spin up channel conduction bands (near high symmetry point R). Moreover, we notice a slight change in the band gap. Upon doping, the $Mg_{0.1}Cu_{0.9}V_2O_6$ system shows an indirect band gap of 1.85 eV in down spin channel and 1.90 eV in up-spin channel whereas upon Ca doping the $Ca_{0.1}Cu_{0.9}V_2O_6$ system shows an indirect band gap of 1.87 eV in down spin channel and 1.91 eV in up-spin channel.

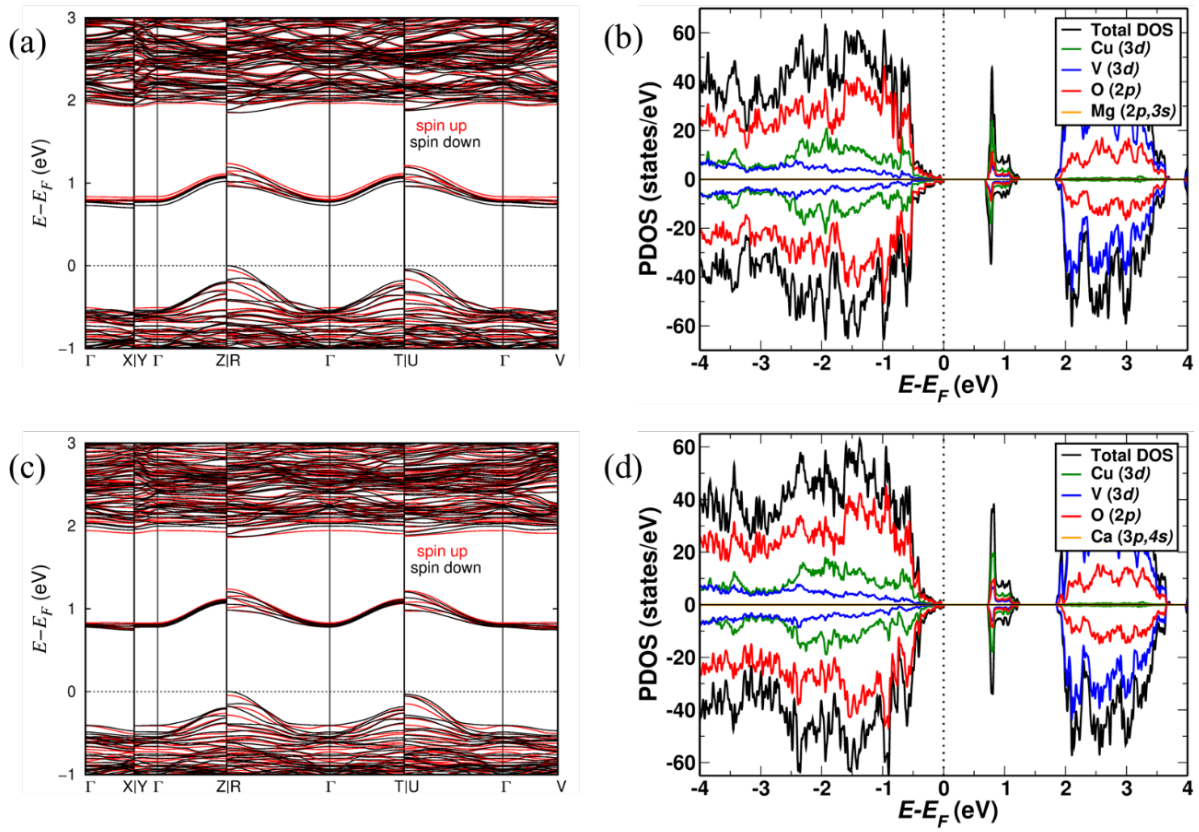

Figure 2-13. The electronic band structure and projected density of states (PDOS) for (a, b) $Mg_{0.1}Cu_{0.9}V_2O_6$ and (c, d) $Ca_{0.1}Cu_{0.9}V_2O_6$ have been calculated in a 1 x 5 x 1 supercell. The black line represents the total density of states, while the orange line displays the projection on Mg 3*s* and 2*p* orbitals, and Ca 4*s* and 3*p* orbitals for the respective compounds. Furthermore, the green line represents Cu 3*d* orbital, the blue line represents the V 3*d* orbital, and the red line represents the O 2*p* orbital. It is essential to note that the system has a net nonzero magnetic moment due to the presence of odd numbers of Cu atoms in the supercell. Both the spin-up (red) and spin-down (black) channels are shown in the band structure plot.

Diffuse reflectance spectroscopy (DRS) data reveal changes in the optical band gap of CuV_2O_6 upon substitution of copper by alkaline earth metals. Figure 2-14a depicts the optical absorption spectra derived from DRS measurements of the end members CuV_2O_6, MgV_2O_6, CaV_2O_6 and solid solutions $A_{0.1}Cu_{0.9}V_2O_6$. The end members CuV_2O_6, MgV_2O_6 and CaV_2O_6 exhibits clear absorption edge at ~700, 600 and 500 nm, respectively. A blue shift in the absorption edge with introduction of alkaline earth metal into the structural framework of CuV_2O_6 was observed. Similarly, Tauc plot constructed from Kubelka-Munk transformation[21, 22] of the DRS data shows

an increase in both direct and indirect bandgaps of CuV_2O_6 upon incorporation of 10% alkaline earth metal, suggesting that the bandgap depends on alkaline earth metal substitution (Figure 2-14b and c). This increase in both direct and indirect bandgap can be attributed to changes in the vanadium octahedral environment with introduction of alkaline earth metal.[46] The band gap obtained via DRS measurement and DFT calculations are in good agreement (Table 2-6).

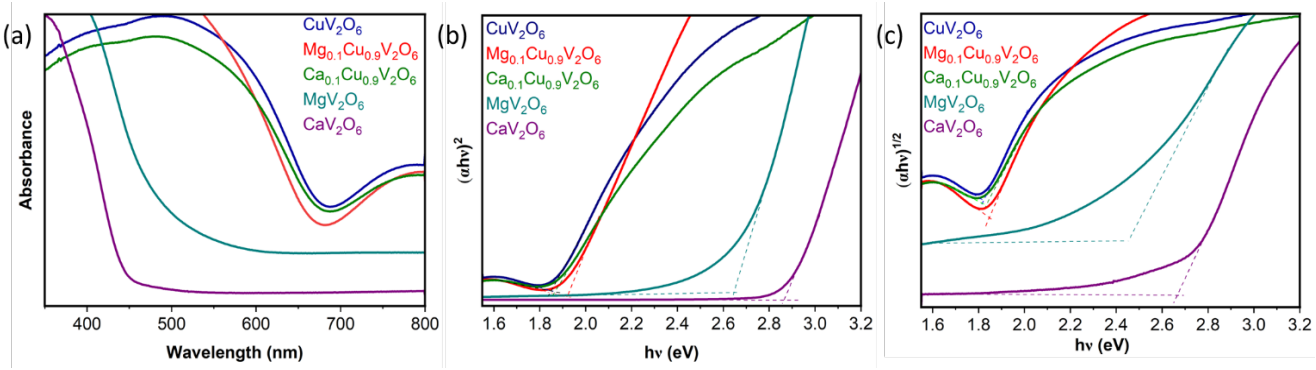

Figure 2-14. (a) UV-Vis optical absorption spectra and Tauc plots corresponding to allowed (b) direct and (c) indirect transitions for the end members CuV_2O_6, MgV_2O_6, CaV_2O_6 and solid solutions $A_{0.1}Cu_{0.9}V_2O_6$.

Table 2-6. Comparison between experimental and computational energy band gap for the end members CuV_2O_6, MgV_2O_6, CaV_2O_6 and solid solutions $A_{0.1}Cu_{0.9}V_2O_6$.

	Experiment		DFT	
Sample	**Direct (eV)**	**Indirect (eV)**	**Direct (eV)**	**Indirect (eV)**
MgV_2O_6	2.62	2.45	2.77	2.68
CaV_2O_6	2.86	2.66	2.89	2.85
CuV_2O_6(Bulk)	1.85	1.82	1.92	1.90
CuV_2O_6(1x5x1)	1.85	1.82	1.86	1.84
$Mg_{0.1}Cu_{0.9}V_2O_6$	1.92	1.85	1.86	1.85
$Ca_{0.1}Cu_{0.9}V_2O_6$	1.87	1.84	1.88	1.87

2.3.3 Photoelectrochemical Properties. The PEC activity of CuV_2O_6 and $A_{0.1}Cu_{0.9}V_2O_6$ thin film electrodes was investigated using chopped linear sweep voltammetry (LSV) in 0.1 M borate buffer (pH = 8) under simulated solar light (100 mW/cm^2). Both copper vanadate and the solid solutions showed anodic photocurrent under reverse bias potential, suggesting n-type semiconductor behavior of the photoelectrode films. At the thermodynamic oxidation potential of water (1.23 V vs RHE), the photocurrent density of CuV_2O_6 and $Ca_{0.1}Cu_{0.9}V_2O_6$ was observed at 53 μA/cm^2 while that of $Mg_{0.1}Cu_{0.9}V_2O_6$ was at 27 μA/cm^2. However, the photocurrent density drastically increased beyond 1.23 V vs RHE and achieved a maximum value of 395, 260 and 230 μA/cm^2 at 1.74 V vs RHE for CuV_2O_6, $Ca_{0.1}Cu_{0.9}V_2O_6$ and $Mg_{0.1}Cu_{0.9}V_2O_6$, respectively (Figure 2-15a). The higher photocurrent density observed in $Ca_{0.1}Cu_{0.9}V_2O_6$ relative to $Mg_{0.1}Cu_{0.9}V_2O_6$ solid solution, can be attributed to a lower bandgap in the former. Figure 15b shows an increase in photocurrent density for all samples when the PEC measurement was carried out in borate + 4 M formate solution, suggesting faster hole transfer kinetics in the presence of hole scavenger.

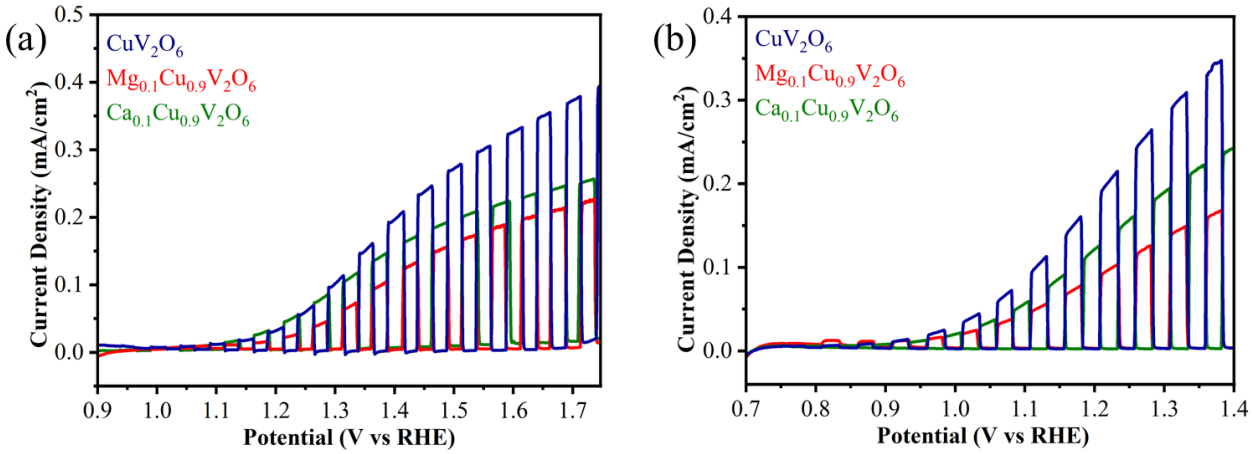

Figure 2-15. Linear sweep voltammogram for CuV_2O_6, $Mg_{0.1}Cu_{0.9}V_2O_6$ and $Ca_{0.1}Cu_{0.9}V_2O_6$ in (a) 0.1 M borate buffer solution (pH = 8), (b) 0.1 M borate buffer + 4 M formate solution (pH = 8) under front-side illumination. The potential sweep rate was 5 mV/s.

2.4 CONCLUSIONS

In this study, time- and energy-efficient solution combustion synthesis was used to prepare ternary oxide semiconductors in the A-Cu-V-O system. To evaluate their potential for solar water conversion, a range of characterization techniques were employed in a study that combined theory and experimentation to investigate the alkaline earth metal substitution in α-CuV_2O_6. We demonstrated that the incorporation of 10% alkaline earth metal into α-CuV_2O_6 can tune the band gap and photoelectrochemical activity. Further studies are required to understand changes in charge separation efficiency, carrier lifetime, and diffusion lengths upon alkaline earth metal substitution.

REFERENCES

1. Jin, X.; Li, J.; Cui, Y.; Liu, X.; Zhang, X.; Yao, J.; Liu, B., Cu_3P–Ni_2P Hybrid Hexagonal Nanosheet Arrays for Efficient Hydrogen Evolution Reaction in Alkaline Solution. *Inorganic Chemistry* **2019,** *58* (17), 11630-11635.
2. Lee, D. K.; Lee, D.; Lumley, M. A.; Choi, K.-S., Progress on Ternary Oxide-Based Photoanodes for use in Photoelectrochemical Cells for Solar Water Splitting. *Chemical Society Reviews* **2019,** *48* (7), 2126-2157.
3. Kudo, A.; Miseki, Y., Heterogeneous Photocatalyst Materials for Water Splitting. *Chemical Society Reviews* **2009,** *38* (1), 253-278.
4. Osterloh, F. E., Inorganic Materials as Catalysts for Photochemical Splitting of Water. *Chemistry of Materials* **2008,** *20* (1), 35-54.
5. Liu, N.; Li, B.; He, Z.; Dai, L.; Wang, H.; Wang, L., Recent Advances and Perspectives On Vanadium- and Manganese-Based Cathode Materials for Aqueous Zinc Ion Batteries. *Journal of Energy Chemistry* **2021,** *59*, 134-159.
6. Hassan, A.; Iqbal, T.; Tahir, M. B.; Afsheen, S., A Review on Copper Vanadate-Based Nanostructures for Photocatalysis Energy Production. *International Journal of Energy Research* **2019,** *43* (1), 9-28.
7. Kim, J. H.; Lee, J. S., Solar Water Splitting: Elaborately Modified $BiVO_4$ Photoanodes for Solar Water Splitting. *Advanced Materials (Weinheim)* **2019,** *31* (20), 1806938.
8. Nakabayashi, Y.; Nishikawa, M.; Nosaka, Y., Fabrication of Bismuth Copper Vanadate Electrodes Through Feasible Chemical Solution Method for Visible Light-Induced Water Oxidation. *Journal of Applied Electrochemistry* **2016,** *46* (1), 9-16.
9. Rajeshwar, K.; Hossain, M. K.; Macaluso, R. T.; Janáky, C.; Varga, A.; Kulesza, P. J., Review-Copper Oxide-Based Ternary and Quaternary Oxides: Where Solid-State Chemistry Meets Photoelectrochemistry. *Journal of the Electrochemical Society* **2018,** *165* (4), H3192-H3206.
10. Hossain, M. K.; Sotelo, P.; Sarker, H. P.; Galante, M. T.; Kormányos, A.; Longo, C.; Macaluso, R. T.; Huda, M. N.; Janáky, C.; Rajeshwar, K., Rapid One-Pot Synthesis and Photoelectrochemical Properties of Copper Vanadates. *ACS Applied Energy Materials* **2019,** *2* (4), 2837-2847.
11. Hossain, M. K.; Sarker, H. P.; Sotelo, P.; Dang, U.; Rodríguez-Gutiérrez, I.; Blawat, J.; Vali, A.; Xie, W.; Oskam, G.; Huda, M. N.; Macaluso, R. T.; Rajeshwar, K., Phase-Pure Copper Vanadate (α-CuV_2O_6): Solution Combustion Synthesis and Characterization. *Chemistry of Materials* **2020,** *32* (14), 6247-6255.
12. Liu, Y.; Li, Q.; Ma, K.; Yang, G.; Wang, C., Graphene Oxide Wrapped CuV_2O_6 Nanobelts as High-Capacity and Long-Life Cathode Materials of Aqueous Zinc-Ion Batteries. *ACS Nano* **2019,** *13* (10), 12081-12089.
13. Jiang, C.-M.; Farmand, M.; Wu, C. H.; Liu, Y-S.; Guo, J.; Drisdell, W. S.; Cooper, J. K.; Sharp, I. D., Electronic Structure, Optoelectronic Properties, and Photoelectrochemical Characteristics of γ-$Cu_3V_2O_8$ Thin Films. *Chemistry of Materials* **2017,** *29* (7), 3334-3345.

14. Benko, F. A.; Koffyberg, F. P., Semiconductivity and Optical Interband Transitions of CuV_2O_6 and $Cu_2V_2O_7$. *Canadian journal of Physics* **1992,** *70* (2-3), 99-103.
15. Zhou, L.; Yan, Q.; Shinde, A.; Guevarra, D.; Newhouse, P. F.; Becerra-Stasiewicz, N.; Chatman, S. M.; Haber, J. A.; Neaton, J. B.; Gregoire, J. M., High Throughput Discovery of Solar Fuels Photoanodes in the CuO-V_2O_5 System. *Advanced Energy Materials* **2015,** *5* (22), 1500968.
16. Guo, W.; Chemelewski, W. D.; Mabayoje, O.; Xiao, P.; Zhang, Y.; Mullins, C. B., Synthesis and Characterization of CuV_2O_6 and $Cu_2V_2O_7$: Two Photoanode Candidates for Photoelectrochemical Water Oxidation. *The Journal of Physical Chemistry C* **2015,** *119* (49), 27220-27227.
17. Newhouse, P. F.; Boyd, D. A.; Shinde, A.; Guevarra, D.; Zhou, L.; Soedarmadji, E.; Li, G.; Neaton, J. B.; Gregoire, J. M., Solar Fuel Photoanodes Prepared by Inkjet Printing of Copper Vanadates. *Journal of Materials Chemistry. A, Materials for Energy and Sustainability* **2016,** *4* (19), 7483-7494.
18. Khan, I.; Qurashi, A., Shape Controlled Synthesis of Copper Vanadate Platelet Nanostructures, Their Optical Band Edges, and Solar-Driven Water Splitting Properties. *Scientific Reports* **2017,** *7* (1), 14370-11.
19. Zhang, M.; Pham, H. K.; Fang, Y.; Tay, Y. F.; Abdi, F. F.; Wong, L. H., The Synergistic Effect of Cation Mixing In Mesoporous $Bi_xFe_{1-x}VO_4$ Heterojunction Photoanodes for Solar Water Splitting. *Journal of Materials Chemistry. A, Materials for Energy and Sustainability* **2019,** *7* (24), 14816-14824.
20. Toby, B. H., EXPGUI, a Graphical User Interface for GSAS. *Journal of Applied Crystallography* **2001,** *34* (2), 210-213.
21. Roy, D.; Samu, G. F.; Hossain, M. K.; Janáky, C.; Rajeshwar, K., On the Measured Optical Bandgap Values of Inorganic Oxide Semiconductors for Solar Fuels Generation. *Catalysis Today* **2018,** *300*, 136-144.
22. Tauc, J.; Grigorovici, R.; Vancu, A., Optical Properties and Electronic Structure of Amorphous Germanium. *Physica Status Solidi (b)* **1966,** *15* (2), 627-637.
23. Viezbicke, B. D.; Patel, S.; Davis, B. E.; Birnie Iii, D. P., Evaluation of the Tauc Method for Optical Absorption Edge Determination: ZnO Thin Films as a Model System. *Physica Status Solidi. B: Basic Solid State Physics* **2015,** *252* (8), 1700-1710.
24. Murphy, A. B., Band-Gap Determination from Diffuse Reflectance Measurements of Semiconductor Films, and Application to Photoelectrochemical Water-Splitting. *Solar Energy Materials and Solar Cells* **2007,** *91* (14), 1326-1337.
25. Hossain, M. K.; Samu, G. F.; Gandha, K.; Santhanagopalan, S.; Liu, J. P.; Janáky, C.; Rajeshwar, K., Solution Combustion Synthesis, Characterization, and Photocatalytic Activity of $CuBi_2O_4$ and Its Nanocomposites with CuO andα-Bi_2O_3. *Journal of Physical Chemistry. C* **2017,** *121* (15), 8252-8261.
26. Giannozzi, P.; Baroni, S.; Bonini, N.; Calandra, M.; Car, R.; Cavazzoni, C.; Ceresoli, D.; Chiarotti, G. L.; Cococcioni, M.; Dabo, I.; Dal Corso, A.; de Gironcoli, S.; Fabris, S.; Fratesi, G.; Gebauer, R.; Gerstmann, U.; Gougoussis, C.; Kokalj, A.; Lazzeri, M.; Martin-

Samos, L.; Marzari, N.; Mauri, F.; Mazzarello, R.; Paolini, S.; Pasquarello, A.; Paulatto, L.; Sbraccia, C.; Scandolo, S.; Sclauzero, G.; Seitsonen, A. P.; Smogunov, A.; Umari, P.; Wentzcovitch, R. M., Quantum Espresso: a Modular and Open-Source Software Project for Quantum Simulations of Materials. *Journal of Physics. Condensed Matter* **2009,** *21* (39), 395502-395502 (19).
27. Andreussi, O.; Brumme, T.; Bunau, O.; Buongiorno Nardelli, M.; Calandra, M.; Car, R.; Cavazzoni, C.; Ceresoli, D.; Cococcioni, M.; Colonna, N.; Carnimeo, I.; Dal Corso, A.; de Gironcoli, S.; Delugas, P.; DiStasio, R.; Ferretti, A.; Floris, A.; Fratesi, G.; Fugallo, G.; Gebauer, R.; Gerstmann, U.; Giustino, F.; Gorni, T.; Jia, J.; Kawamura, M.; Ko, H.-Y.; Kokalj, A.; Küçükbenli, E.; Lazzeri, M.; Marsili, M.; Marzari, N.; Mauri, F.; Nguyen, N. L.; Nguyen, H.-V.; Otero-de-la-Roza, A.; Paulatto, L.; Poncé, S.; Giannozzi, P.; Rocca, D.; Sabatini, R.; Santra, B.; Schlipf, M.; Seitsonen, A. P.; Smogunov, A.; Timrov, I.; Thonhauser, T.; Umari, P.; Vast, N.; Wu, X.; Baroni, S., Advanced Capabilities for Materials Modelling with Quantum Espresso. *Journal of Physics. Condensed Matter* **2017**.
28. Blöchl, P. E., Projector Augmented-wave Method. *Physical Review B* **1994,** *50* (24), 17953-17979.
29. Perdew, J. P.; Ruzsinszky, A.; Csonka, G. I.; Vydrov, O. A.; Scuseria, G. E.; Constantin, L. A.; Zhou, X.; Burke, K., Restoring the Density-Gradient Expansion for Exchange in Solids and Surfaces. *Physical Review Letters* **2008,** *100* (13), 136406.
30. Monkhorst, H. J.; Pack, J. D., Special Points for Brillouin-Zone Integrations. *Physical Review B* **1976,** *13* (12), 5188-5192.
31. Marzari, N.; Vanderbilt, D.; De Vita, A.; Payne, M. C., Thermal Contraction and Disordering of the Al(110) Surface. *Physical Review Letters* **1999,** *82* (16), 3296-3299.
32. Feynman, R. P., Forces in Molecules. *Physical Review* **1939,** *56* (4), 340-343.
33. Liechtenstein, A. I.; Anisimov, V. I.; Zaanen, J., Density-Functional Theory and Strong Interactions: Orbital Ordering in Mott-Hubbard Insulators. *Physical Review B* **1995,** *52* (8), R5467-R5470.
34. Yourey, J. E.; Pyper, K. J.; Kurtz, J. B.; Bartlett, B. M., Chemical Stability of $CuWO_4$ for Photoelectrochemical Water Oxidation. *The Journal of Physical Chemistry C* **2013,** *117* (17), 8708-8718.
35. Tian, C. M.; Jiang, M.; Tang, D.; Qiao, L.; Xiao, H. Y.; Oropeza, F. E.; Hofmann, J. P.; Hensen, E. J. M.; Tadich, A.; Li, W.; Qi, D. C.; Zhang, K. H. L., Elucidating the Electronic Structure of $CuWO_4$ Thin Films for Enhanced Photoelectrochemical Water Splitting. *Journal of materials chemistry. A, Materials for Energy and Sustainability* **2019,** *7* (19), 11895-11907.
36. MocaŁA, K.; ZioŁKowski, J., Polymorphism of the Bivalent Metal Vanadates MeV_2O_6 (Me = Mg, Ca, Mn, Co, Ni, Cu, Zn, Cd). *Journal of Solid State Chemistry* **1987,** *69* (2), 299-311.
37. Hong, S.; Burkhow, S. J.; Doughty, R. M.; Cheng, Y.; Ryan, B. J.; Mantravadi, A.; Roling, L. T.; Panthani, M. G.; Osterloh, F. E.; Smith, E. A.; Zaikina, J. V., Local Structural Disorder in Metavanadates MV_2O_6 (M = Zn and Cu) Synthesized by the Deep Eutectic Solvent

Route: Photoactive Oxides with Oxygen Vacancies. *Chemistry of Materials* **2021,** *33* (5), 1667-1682.
38. Calvo, C.; Manolescu, D., Refinement of the Structure of CuV_2O_6. *Acta Crystallographica Section B* **1973,** *29* (8), 1743-1745.
39. Ng, H. N.; Calvo, C., Crystal Structure of and Electron Spin Resonance of Mn^{2+} in MgV_2O_6. *Canadian Journal of Chemistry* **1972,** *50* (22), 3619-3624.
40. Bouloux, J.-C.; Perez, G.; Galy, J., Structure Cristalline des Métavanadates CaV_2O_6 et $CdV_2O_6\alpha$. La Lransformation Polymorphique $CdV_2O_6\alpha \rightleftarrows CdV_2O_6\beta$. *Bulletin de Minéralogie* **1972,** *95* (1), 130-133.
41. Jin, X.; Ding, X.; Qin, Z.; Li, Y.; Jiao, M.; Wang, R.; Yang, X.; Lv, X., Comprehensive Study of Electronic, Optical, and Thermophysical Properties of Metavanadates CaV_2O_6 and MgV_2O_6. *Inorganic Chemistry* **2022,** *61* (44), 17623-17633.
42. Khairallah, F.; Glisenti, A., XPS Study of MgO Nanopowders Obtained by Different Preparation Procedures. *Surface Science Spectra* **2006,** *13* (1), 58-71.
43. Manjunath, G.; Vardhan, R. V.; Salian, A.; Jagannatha, R.; Kedia, M.; Mandal, S., Effect of Annealing-Temperature-Assisted Phase Evolution on Conductivity of Solution Combustion Processed Calcium Vanadium Oxide Films. *Bulletin of Materials Science* **2018,** *41* (5), 1-9.
44. Rawat, A.; Clark, L.; Zhang, C.; Cavin, J.; Sangwan, V. K.; Toth, P. S.; Janáky, C.; Ananth, R.; Goldfine, E.; Bedzyk, M. J.; Weiss, E. A.; Rondinelli, J. M.; Hersam, M. C.; Meletis, E. I.; Rajeshwar, K., Solution Combustion Synthesis and Characterization of Magnesium Copper Vanadates. *Inorganic Chemistry* **2023,** *62* (23), 8903-8913.
45. Yu, R.; Xue, N.; Huo, S.; Li, J.; Wang, J., Structure Characteristics and Photoactivity of Simultaneous Luminescence and Photocatalysis in CaV_2O_6 Nanorods Synthesized by the Sol-Gel Pechini Method. **2015,** *5* (78), 6352-63512.
46. Lakshminarasimhan, N.; Li, J.; Hsu, H.-C.; Subramanian, M. A., Optical Properties of Brannerite-Type Vanadium Oxides, MV_2O_6 (M = Ca, Mg, Mn, Co, Ni, Cu, or Zn). *Journal of Solid State Chemistry* **2022,** *312*, 123279.

CHAPTER 3

SOLUTION COMBUSTION SYNTHESIS OF ALKALINE EARTH METAL–SUBSTITUTED COPPER PYROVANADATE

3.1 INTRODUCTION

Photoelectrochemical water splitting is a unique energy conversion approach that utilizes solar energy to generate hydrogen and oxygen from water using a semiconductor photocatalyst. The development of a photoelectrode that can enhance the efficiency of solar energy conversion is crucial. An ideal photoelectrode for water splitting should possess high stability against photocorrosion under applicable conditions, be cost-effective and easily accessible, have a suitable bandgap to absorb a significant portion of the solar spectrum and the potential of the valence (1.23 V) and conduction (0.00 V) band edge must be sufficient enough for oxygen evolution reaction (OER) and hydrogen evolution reaction (HER), respectively.

Metal vanadates are one of the most suitable photoelectrodes for photoelectrochemical water splitting because they have a favorable bandgap that allows for visible light absorption.[1-12] Recently, both $WO_3/BiVO_4$ nanorods and $BiVO_4$ have been reported to be photoelectrode candidates for photocatalytic hydrogen generation.[2, 3] Additionally, two polymorphs of $AgVO_3$ prepared through electrodeposition have been studied for their photoelectrochemical activity.[4] ZnV_2O_6 and $FeVO_4$ have also been identified as promising photoelectrode materials for solar water splitting into hydrogen and oxygen.[5, 13] Finally, the Cu-V-O family of compounds have shown potential for practical applications in solar water splitting.[7-10, 12, 14, 15]

Mixed metal vanadates have been reported to improve the performance of photocatalysts for hydrogen production using solar energy and water. $Bi_xFe_{1-x}VO_4$ photoanodes exhibit a better

photoelectrochemical performance for solar water splitting than the end members $BiVO_4$ and $FeVO_4$.[1] A combination of Bi and Cu in $BiCu_2VO_6$ photocatalyst can absorb photons in the visible light range more efficiently than $BiVO_4$ or CuO for oxygen production in aqueous suspension.[16, 17]

In the present study, solid solutions of alkaline earth metal and copper pyrovanadates were prepared via solution combustion synthesis. We demonstrated that the substitution of copper with alkaline earth metal influences the structural, electronic, optical, and PEC properties of $Cu_2V_2O_7$ and $M_2V_2O_7$ (M = Mg, Ca, Sr).

3.2 EXPERIMENTS AND CALCULATION METHODS

3.2.1 Materials. $Cu(NO_3)_2{\cdot}2.5H_2O$, (Alfa Aesar), $Mg(NO_3)_2{\cdot}6H_2O$ (99+%, Acros Organics), $Ca(NO_3)_2{\cdot}4H_2O$ (Certified ACS, Fisher Scientific), $Sr(NO_3)_2$ (99+% ACS reagent, Sigma Aldrich) NH_4VO_3 (Alfa Aesar), $C_4H_6O_5$ (98%, Alfa Aesar), NH_4OH (Alfa Aesa), HCOONa (Kodak), H_3BO_3 (Fisher Scientific) and $Na_2B_4O_7{\cdot}10H_2O$ were used without further purification.

3.2.2 Synthesis. The pyrovanadates were prepared via solution combustion synthesis following the chemical reaction shown in Equations 1-7.

$$12Cu(NO_3)_2{\cdot}2.5H_2O_{(s)} + 12NH_4VO_{3(s)} + 7C_4H_6O_{5(s)} \rightarrow 6\mathbf{Cu_2V_2O_7}_{(s)} + 18N_{2(g)} + 28CO_{2(g)} + 75\ H_2O_{(g)} \quad (1)$$

$$12Mg(NO_3)_2{\cdot}6H_2O_{(s)} + 12NH_4VO_{3(s)} + 7C_4H_6O_{5(s)} \rightarrow 6\mathbf{Mg_2V_2O_7}_{(s)} + 18N_{2(g)} + 28CO_{2(g)} + 112H_2O_{(g)} \quad (2)$$

$$12Ca(NO_3)_2{\cdot}4H_2O_{(s)} + 12NH_4VO_{3(s)} + 7C_4H_6O_{5(s)} \rightarrow 6\mathbf{Ca_2V_2O_7}_{(s)} + 18N_{2(g)} + 28CO_{2(g)} + 88H_2O_{(g)} \quad (3)$$

$$12Sr(NO_3)_{2(s)} + 12NH_4VO_{3(s)} + 7C_4H_6O_{5(s)} \rightarrow 6\mathbf{Sr_2V_2O_7}_{(s)} + 18N_{2(g)} + 28CO_{2(g)} + 40H_2O_{(g)} \quad (4)$$

$$8Cu(NO_3)_2{\cdot}2.5H_2O_{(s)} + 4Mg(NO_3)_2{\cdot}6H_2O_{(s)} + 12NH_4VO_{3(s)} + 7C_4H_6O_{5(s)} \rightarrow 6\mathbf{Mg_{0.67}Cu_{1.33}V_2O_7}_{(s)} + 18N_{2(g)} + 28CO_{2(g)} + 84H_2O_{(g)} \quad (5)$$

$$6Cu(NO_3)_2{\cdot}2.5H_2O_{(s)} + 6Ca(NO_3)_2{\cdot}4H_2O_{(s)} + 12NH_4VO_{3(s)} + 7C_4H_6O_{5(s)} \rightarrow 6\mathbf{CaCuV_2O_7}_{(s)} + 18N_{2(g)} + 28CO_{2(g)} + 79H_2O_{(g)} \quad (6)$$

$$6Cu(NO_3)_2{\cdot}2.5H_2O_{(s)} + 6Sr(NO_3)_{2(s)} + 12NH_4VO_{3(s)} + 7C_4H_6O_{5(s)} \rightarrow 6\mathbf{SrCuV_2O_7}_{(s)} + 18N_{2(g)} + 28CO_{2(g)} + 55H_2O_{(g)} \quad (7)$$

The polycrystalline samples were synthesized through solution combustion synthesis (SCS) using the same process detailed in our previous report.[18] To prepare the end members $Mg_2V_2O_7$, $Ca_2V_2O_7$, $Sr_2V_2O_7$, $Cu_2V_2O_7$ as well as the solid solutions $Mg_{0.67}Cu_{1.33}V_2O_7$, $CaCuV_2O_7$, and $SrCuV_2O_7$, alkaline earth metal or copper nitrates, ammonium vanadate, and DL-malic acid were dissolved in a beaker of water according to Table 3-1. After the solutions were mixed thoroughly, they were dehydrated and ignited in a preheated muffle furnace at around 300 °C for 5-10 min. All samples were then annealed at 500-650 °C for 1 hour in an alumina crucible to improve their crystallinity and remove any organic residue.

3.2.3 Physical Characterization. Samples were analyzed by powder X-ray diffraction recorded at room temperature using a laboratory Stoe Stadi-P powder diffractometer (Mo Kα radiation: λ = 0.7107 Å, Ge (111) monochromator, goniometer circles: 140 and 80 mm, Mythen Dectris 1K detector) operating in Debye-Scherrer geometry. The samples were measured at 40 kV and 40 mA over a 2θ range of 3 - 30° with a step size of 2θ = 0.02° and counting time = 1 s $step^{-1}$. For improved particle statistics during the PXRD measurement, the capillary was rotated. Phase analyses and Rietveld refinement of the PXRD data was carried out using GSAS-EXPGUI software package and TOPAS.[19, 20] For structural characterization, Transmission Electron Microscopy (TEM) analysis was carried out using Hitachi H-9500 instrument operating at an acceleration voltage of 300 kV and a LaB_6 filament.

Table 3-1. The concentration of precursor mixtures for the synthesis of end members and solid solutions via SCS.

Sample	Precursor (M)					
	$Mg(NO_3)_2.6H_2O$	$Ca(NO_3)_2.4H_2O$	$Sr(NO_3)_2$	$Cu(NO_3)_2.6H_2O$	NH_4VO_3	$C_4H_6O_5$
$Mg_2V_2O_7$	0.5000	0.0000	0.0000	0.0000	0.5000	1.0000
$Mg_{0.67}Cu_{1.33}V_2O_7$	0.1675	0.0000	0.0000	0.3325	0.5000	1.0000
$Ca_2V_2O_7$	0.0000	0.5000	0.0000	0.0000	0.5000	1.0000
$CaCuV_2O_7$	0.0000	0.2500	0.0000	0.2500	0.5000	1.0000
$Sr_2V_2O_7$	0.000	0.0000	0.5000	0.0000	0.5000	1.0000
$SrCuV_2O_7$	0.0000	0.0000	0.2500	0.2500	0.5000	1.0000
β-$Cu_2V_2O_7$	0.0000	0.0000	0.0000	0.5000	0.5000	1.0000
α- $Cu_2V_2O_7$	0.0000	0.0000	0.0000	0.5000	0.5000	1.0000

3.2.4 Spectroscopic Analyses. Raman spectra of the samples were collected using Thermo scientific DXR3 Raman microscope equipped with 532 nm diode laser (He-Ne gas laser) at a power of 1 mW. Diffuse reflectance spectroscopy measurements were carried out using a Varian Cary 500 instrument under diffuse reflectance mode and over the range of 350 – 700 nm. The absorption coefficient, α, was calculated from the Kubelka – Munk transformation (eq 2) of the DRS data.[21, 22]

$$\frac{\propto}{S} = \frac{(1-R)^2}{2R} \tag{8}$$

Here, α is the absorption coefficient, S is the scattering coefficient and R represents the reflectance. Optical bandgaps were estimated based on Tauc analyses presented in eq 3.[21-24]

$$h\nu = \propto (h\nu - E_g)^n \tag{9}$$

where E_g is the bandgap and n is nature of the electronic transition, i.e., n = ½ for direct allowed transition and n = 2 for indirect allowed transition.

The Thermo iCap7600 instrument with a radial view and ESI SC-2DX PrepFAST autosampler was used for inductively coupled plasma-optical emission spectroscopy (ICP-OES) analysis following the previously reported method.[25] The prepFAST system was utilized for online dilution and calibration curves were generated from standards of Cu, Mg, Ca, Sr, and V with concentrations of 10, 5, 2, 1, and 0.5 ppm, respectively. To dissolve the vanadium oxide precipitate, a modification to the standard digestion method was necessary and involved a second step using 500 µL of concentrated hydrochloric acid and heated overnight at 65 °C.

3.2.5 Electrode Preparation and Photoelectrochemical Measurements. The electrode films were prepared by suspending 100 mg of the bulk powder in 20 mL of ethanol and then depositing

it on fluorine-doped tin oxide (FTO) by spray-coating, using a method that has been previously reported.[26] To confirm the distribution of elements, texture, and surface homogeneity, electron microscopy and EDX were employed. A CH Instruments, Model CHI720C, was used to perform the photoelectrochemical (PEC) measurements. The working electrodes' surface was exposed to light using a 400 W Xe-arc lamp (Newport) with an IR filter and a calibrated Si reference cell (Oriel) to attain a measured light intensity of 1 sun (100 mW/cm^2). The PEC measurements were carried out in a standard one-compartment three-electrode electrochemical cell, with the vanadate films serving as the working electrode, Ag/AgCl/3M KCl acting as the reference electrode, and Pt wire as the counter electrode. The potential conversion to the reversible hydrogen electrode was determined based on eq 4 in this study.

$$E_{RHE} = E_{Ag/AgCl} + E^0_{Ag/AgCl(3M\ KCl)} + 0.0591pH \qquad (10)$$

where $E^0_{Ag/AgCl(3M\ KCl)}$ = 0.209 V versus NHE at 25 °C.

Photocurrent measurements of the vanadate films were measured in a 0.1 M borate buffer electrolyte (pH = 8.0) using a potential scan of 5 mV/s sweep rate. In some cases, 4 M formate was added to the electrolyte as a hole scavenger. Front-side illumination under a manual chopper was used at intervals of 5 s.

3.2.6 Computational Methodology. Spin polarized density functional theory (DFT+U) with Hubbard U correction for Cu and V 3*d* orbital calculations were performed using the Vienna ab initio Simulation Package (VASP-5.4.4)[27] within the atomic simulation environment (ASE). The exchange and correlation were described by the PBE (Perdew-Burke-Ernzerhof) functional[28] within the GGA (generalized gradient approximation) approximation. The projector-augmented wave (PAW)[29] method was employed to treat ion-electron interactions. Periodic boundary conditions were used in all three directions to simulate the model systems. To optimize the

geometry, the cells were relaxed until the residual forces on all atoms reached a level below 0.01 eV $Å^{-1}$. The electronic basis set was expanded using plane waves and a kinetic energy cut-off of 600 eV was applied for the entire calculation to ensure accurate results. The Monkhorst-Pack scheme was used for K points sampling within the first Brillouin zone (BZ). For geometric optimization, different K-point meshes were utilized for different compounds. 5×5×3 and 5×5×1 k-point meshes were used for monoclinic and orthorhombic $Cu_2V_2O_7$. For $MgCuV_2O_7$, $CaCuV_2O_7$, and $SrCuV_2O_7$, we used 5×5×3, 5×5×5 and 5×5×1 k-point mesh, respectively. While $Mg_2V_2O_7$ and $Ca_2V_2O_7$ used a 5×5×5 k-point mesh, and $Sr_2V_2O_7$ used a 5×5×3 k-point mesh. However, to calculate the density of states (DOS), a more denser k-point grid was employed..

The electron self-interaction correction (SIC), particularly for *d* and *f* orbitals, is often underestimated with the use of DFT, resulting in inadequate descriptions of geometric, electronic, optical, and magnetic structures. In order to address the SIC error associated with the standard DFT approach, we employed the DFT+U framework to analyze the magnetic, electronic, optical, and structural characteristics of $Cu_2V_2O_7$, $MCuV_2O_7$ and $M_2V_2O_7$. The SIC can be controlled by adjusting the on-site Coulombic interaction term U and exchange parameter J. In this study, an effective U value of 3.25 eV and 6.5 eV were applied to the V and Cu 3*d* orbitals, respectively. These values produced lattice parameters and energy band gap that were comparable to the results of the experimental study. Furthermore, similar U values for V and Cu 3*d* orbitals were also applied in other studies for many compounds.[30-35] The experimental values for lattice parameters show a slight deviation (approximately 2%), but they still fall within the typical error limits of DFT. Additionally, the chosen method gave similar description of magnetic ordering as obtained from other calculations.[36] Finally, the VESTA software was used to visualize and analyze the crystal structure.[33] The computational study was done in collaboration with Dr. Hori Sarker.

3.3 RESULTS AND DISCUSSION

3.3.1 Synthesis and structure. For the solution combustion synthesis of the pyrovanadates, DL-malic acid was utilized as both fuel and chealating agent. Previous reports have suggested a potential mechanism where $M(NO_3)_2$ and NH_4VO_3 dissociate in solution, producing their respective ions as shown in equation 11 - 12.[37, 38] The metals formed a polymeric complex network when DL-malic acid acted as the chelating agent (equation 13). The complex undergoes thermal breakdown through combustion once the fuel has reached ignition temperature, resulting in the formation of the final product.

$$NH_4VO_3 \rightarrow NH_4^+ + VO_3^- \quad (11)$$

$$M(NO_3)_2 \rightarrow M^{2+} + 2NO_3^- \quad (12)$$

$$M^{2+} - MA + VO_3^- - MA \rightarrow M^{2+} - MA - VO_3^- - MA - \quad (13)$$

The ICP-OES method was utilized to evaluate the purity and composition of the samples derived from SCS. As per Table 3-2, the sample compositions were in great conformity with the anticipated values from the precursor amounts added, for both the end members and the solid solutions, within the confines of experimental uncertainty. The combustion synthesis yields were consistently high, ranging from 96% to 98% for all the samples. These findings indicate that SCS can produce a phase-pure product which aligns with our previous reports on the Cu-V-O system.[18, 39]

Table 3-2. Comparison between ICP-OES assays with precursor added during SCS.

Sample	Experimentally Determined Ratio				Precursor Added			
	Cu/2V	Mg/2V	Ca/2V	Sr/2V	Cu/2V	Mg/2V	Ca/2V	Sr/2V
$Mg_2V_2O_7$	0.00	1.99	0.00	0.00	0.00	2.00	0.00	0.00
$Mg0.67Cu_{1.33}V_2O_7$	1.41	0.69	0.00	0.00	1.33	0.67	0.00	0.00
$Ca_2V_2O_7$	0.00	0.00	1.96	0.00	0.00	0.00	2.00	0.00
$CaCuV_2O_7$	1.02	0.00	0.98	0.00	1.00	0.00	1.00	0.00
$Sr_2V_2O_7$	0.00	0.00	0.00	1.98	0.00	0.00	0.00	2.00
$SrCuV_2O_7$	1.08	0.00	0.00	0.99	1.00	0.00	0.00	1.00
β-$Cu_2V_2O_7$	2.23	0.00	0.00	0.00	2.00	0.00	0.00	0.00
α-$Cu_2V_2O_7$	2.17	0.00	0.00	0.00	2.00	0.00	0.00	0.00

In order to examine how annealing temperatures impact the as-synthesized samples, various polymorphs of copper and alkaline earth metal pyrovanadates were obtained by changing the annealing temperatures of the as-synthesized $M_2V_2O_7$ as depicted in Figure 3-1. Annealing at 500 °C revealed a well-defined monoclinic β-$Cu_2V_2O_7$, triclinic $Mg_2V_2O_7$, triclinic $Ca_2V_2O_7$, and tetragonal $Sr_2V_2O_7$. Mixed phases were observed when the as-synthesized pyrovanadates were annealed at 550 °C. Further increasing the anneal temperature to 650 °C resulted in the formation of orthorhombic α-$Cu_2V_2O_7$, monoclinic $Mg_2V_2O_7$, and triclinic $Sr_2V_2O_7$. However, no phase transformation was recorded when as-synthesized $Ca_2V_2O_7$ was annealed at 500 - 650 °C.

Furthermore, $Mg_2V_2O_7$ has two stable polymorphs; low temperature β-$Mg_2V_2O_7$ (triclinic, space group, $P\bar{1}$) and high temperature α-$Mg_2V_2O_7$ (monoclinic, space group, $P2/c$) as depicted in Figure 3-1a. PXRD pattern confirmed the formation of β-polymorph when the as-synthesized

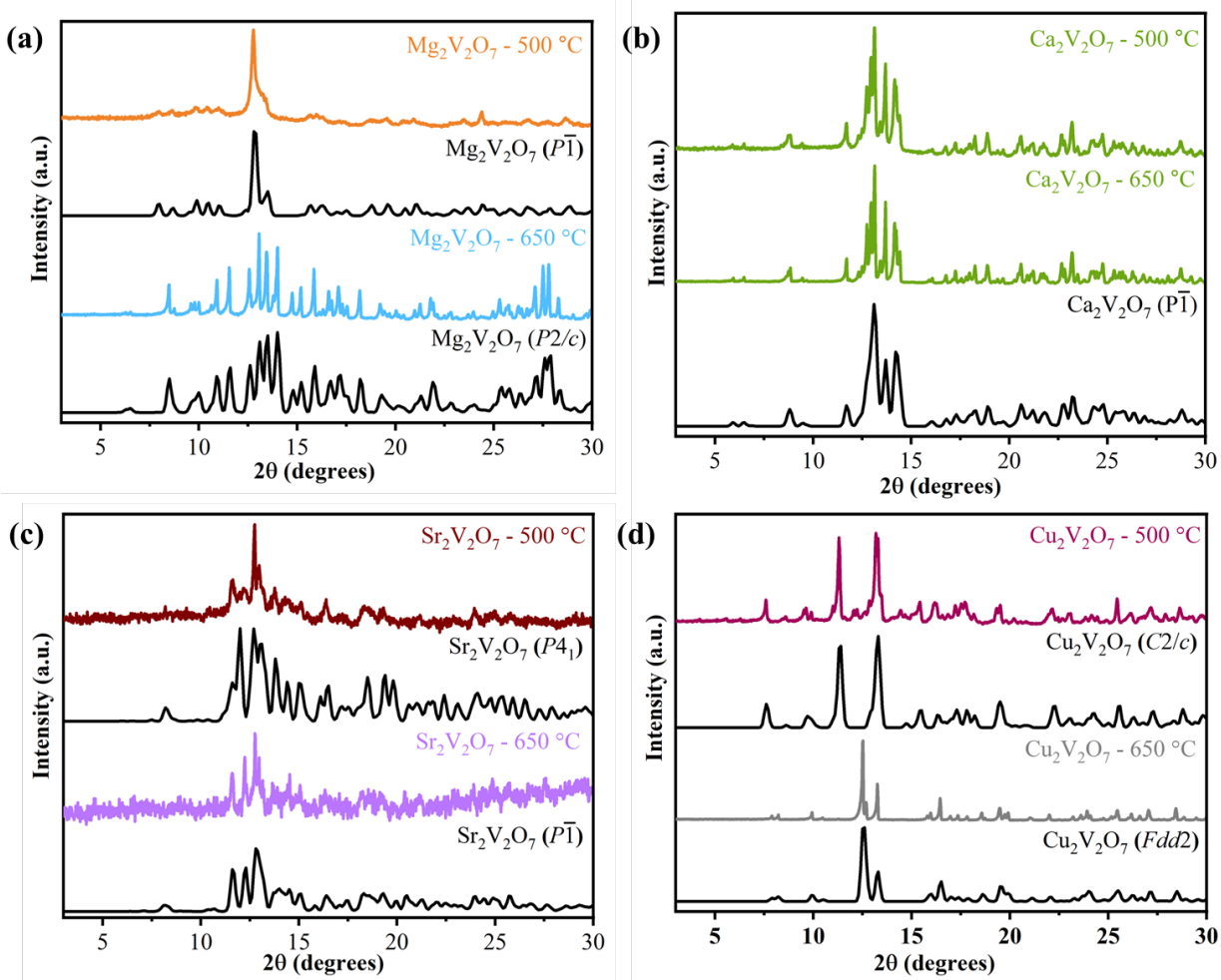

Figure 3-1. Comparison of XRD patterns for various polymorphs of pyrovanadates obtained by changing anneal temperature and their respective reference in black: (a) triclinic (ICDD 128342) and monoclinic (ICDD 086711) $Mg_2V_2O_7$, (b) triclinic (ICDD 133067) $Ca_2V_2O_7$, (c) tetragonal (ICSD 10330) and triclinic (ICDD 125309) $Sr_2V_2O_7$ and (d) monoclinic (ICDD 260569) and orthorhombic (ICSD 1831) $Cu_2V_2O_7$.

$Mg_2V_2O_7$ was annealed at 500 °C for 1h, which eventually started to transform to the monoclinic phase above 500 °C. At 650 °C, a complete transformation to the α-polymorph was achieved. Phase pure β- and α-polymorphs were obtained at 500 and 650 °C, respectively. A monoclinic $Mg_2V_2O_7$ was prepared via a solid-state method at 650 °C whereas the triclinic polymorph was obtained after sintering at 800 °C.[40, 41] In our case, the triclinic polymorph may be favored by the solution combustion synthesis environment as previously observed in Cu-V-O system.[18] When

subjected to different annealing temperatures, $Ca_2V_2O_7$ displayed a contrasting behavior to $Mg_2V_2O_7$. The as-synthesized $Ca_2V_2O_7$ did not undergo any phase transformation when annealed for an hour at 500-650 °C, indicating that it only exists in the triclinic phase with a space group of $P\bar{1}$ (Figure 3-1b). Synthesis of $Ca_2V_2O_7$ via a facile solid-state reaction, co-precipitation and hydrothermal techniques yielded a triclinic phase.[41-44]

Similarly, annealing as-synthesized $Sr_2V_2O_7$ at 500 °C resulted in the formation of a tetragonal β- $Sr_2V_2O_7$. At a higher annealing temperature of 650 °C, a triclinic α-$Sr_2V_2O_7$ phase was formed, indicating that changes in the annealing temperature can lead to the formation of β- and α-polymorphs, as illustrated in Figure 3-1c. Triclinic α-$Sr_2V_2O_7$ was obtained through solid state method at 1100 °C whereas the β-$Sr_2V_2O_7$ was only reported by J.N. Dann et al.[45, 46] Furthermore, it was observed that $Cu_2V_2O_7$ crystallized in low temperature β-$Cu_2V_2O_7$ and high temperature α-$Cu_2V_2O_7$ at 500 °C and 650 °C, respectively as depicted in Figure 3-1d. Upon annealing the as-synthesized sample at 550°C, a mixed phase was observed suggesting the transformation of β-$Cu_2V_2O_7$ to α-polymorphs above 500 °C, which is consistent with previous report.[18] The β to α transition in Cu−V−O samples was previously reported at 605 – 610 °C.[18, 47]

On the other hand, copper and alkaline earth metal solid solutions were synthesized for the first time via solution combustion synthesis. The resulting structures of $Mg_{0.67}Cu_{1.33}V_2O_7$ and $CaCuV_2O_7$ were monoclinic after thermal annealing at 650°C for one hour, while $SrCuV_2O_7$ formed an orthorhombic structure. Figure 3-2 shows a comparison of the PXRD patterns of the solid solutions and end members. The powders of the solid solutions, including $Mg_{0.67}Cu_{1.33}V_2O_7$, $CaCuV_2O_7$ and $SrCuV_2O_7$, were previously obtained using a solid-state method at a temperature range of 660-750°C.[48-51]

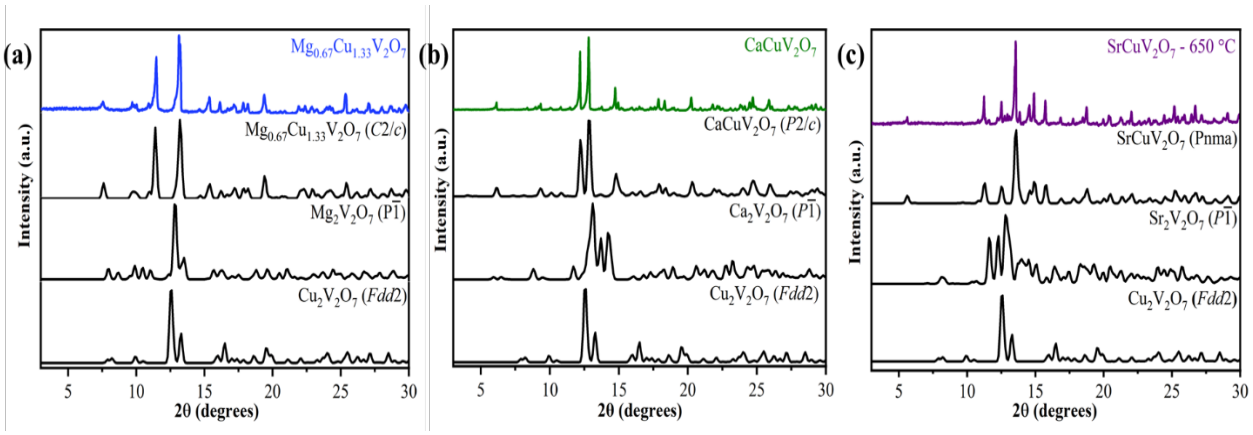

Figure 3-2. Comparison between experimental and reference (in black) XRD patterns for the solid solutions and end members: (a) monoclinic $Mg_{0.67}Cu_{1.33}V_2O_7$ (ICSD 69732), (b) monoclinic $CaCuV_2O_7$ (ICSD 33851) and, (c) orthorhombic $SrCuV_2O_7$ (ICSD 33852).

The structural refinement of the end members and solid solutions' structure was done using PXRD data and a pre-existing structural model. Compositions, crystal systems and unit cell parameters for various phases prepared via solution combustion synthesis were obtained through Rietveld refinement. For $Cu_2V_2O_7$, both the PXRD of samples annealed at 500 and 650 °C were refined whereas only end member and solid solutions annealed at 650 °C were considered for Rietveld refinement as shown in Figure 3-3. Table 3-3 summarizes the unit cell parameters and the refinement results for the end members and solid solutions.

The unit cell parameters and compositions were obtained through the Rietveld refinement of the PXRD data for the end members and the solid solutions. The Rietveld refinement plots were presented in Figure 3-3a-h and the refinement summary in Table 3-3. Apart from $Cu_2V_2O_7$ (both 500 and 650 °C), only samples annealed at 650 °C were refined. As presented in Table 3-3, the unit cell parameters obtained via Rietveld refinement and DFT calculations were in good agreement. Rietveld refinement of the XRD data shows that $Mg_2V_2O_7$, $Ca_2V_2O_7$, $Sr_2V_2O_7$, α-$Cu_2V_2O_7$, and $Mg_{0.67}C_{1.33}V_2O_7$ exists in pure phase. However, there were two minority phases in

β-$Cu_2V_2O_7$; α-$Cu_2V_2O_7$ (~2.1%) and α-CuV_2O_6 (~9.0%). Similarly, $CaCuV_2O_7$ showed CaV_2O_6 (~ 3.7 %) as minority phase. Finally, $SrCuV_2O_7$ has $Sr_2V_2O_7$ (~2.0%) as the only minority phase.

The crystal structures of the end members and solid solutions were presented in Figure 3-4. As previously mentioned, β-$Cu_2V_2O_7$, and α-$Cu_2V_2O_7$ crystallized in monoclinic space group *C*2/*c* and orthorhombic space group *Fdd*2, respectively (Figures 3-4a, b).[52] Both β-$Cu_2V_2O_7$, and α-$Cu_2V_2O_7$ contain distorted CuO_5 square pyramids that share their edges and linked by V_2O_7, which was formed through the dimerization of VO_4 tetrahedra.

The crystal structure of monoclinic $Mg_2V_2O_7$ with space group *P*2/*c* is presented in Figure 3-4c. The structure contains VO_4 tetrahedra and edge sharing MgO_6 octahedra. $Ca_2V_2O_7$ crystallized in triclinic space group $P\bar{1}$ as depicted in Figure 3-4d. Within the structure, there are CaO_6 and CaO_7 polyhedral units that are collinear along with alternating VO_4 tetrahedra and VO_5 square pyramids (emerged by joining two VO_4 dimers with a shared edge).[42] In the crystal structure of triclinic (space group $P\bar{1}$) $Sr_2V_2O_7$, which is shown in Figure 3-4e, there are layers composed of SrO_8 and SrO_9 polyhedral, as well as VO_4 tetrahedra. The tetrahedrally coordinated vanadium atom are connected by sharing an oxygen atom, creating V_2O_7.

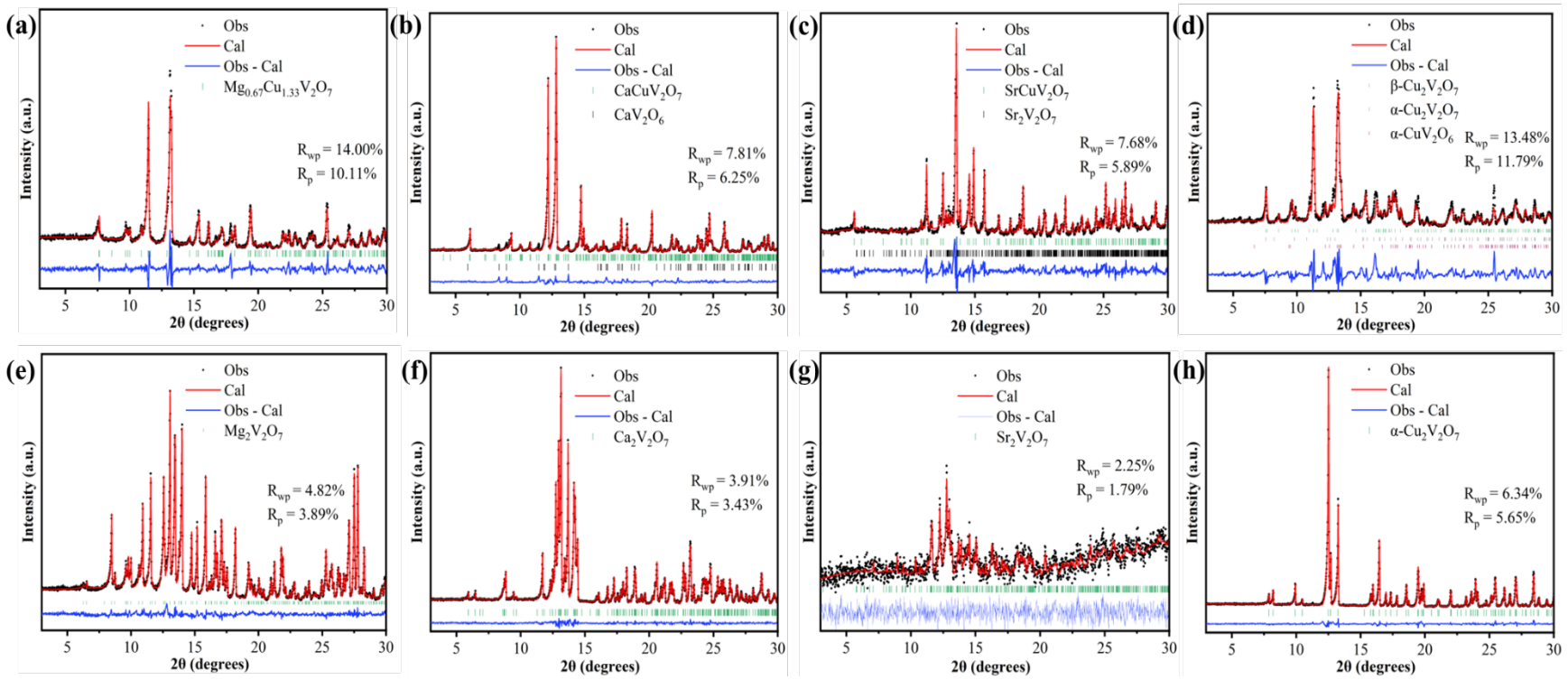

Figure 3-3. Rietveld refinement plots for the end members and solid solutions: (a) monoclinic β-$Cu_2V_2O_7$, (b) orthorhombic α-$Cu_2V_2O_7$, (c) monoclinic $Mg_2V_2O_7$, (d) triclinic $Ca_2V_2O_7$, (e) triclinic $Sr_2V_2O_7$ (f) monoclinic $Mg_{0.67}Cu_{1.33}V_2O_7$, (g) monoclinic $CaCuV_2O_7$ and, (h) orthorhombic $SrCuV_2O_7$.

Table 3-3. Comparison between unit cell parameters obtained via Rietveld refinement and DFT calculations.

Sample		Unit cell parameters							
		a (Å)	b (Å)	c (Å)	α (°)	β (°)	γ (°)	V (Å^3)	R_{wp} (%)
$Mg_2V_2O_7$	Expt.	6.6129(2)	8.4237(3)	9.4934(2)	90.000	100.633(2)	90.000	519.750(2)	4.82
	DFT	6.6900	8.5000	9.5800	90.000	100.850	90.000	535.720	
$Mg0._{67}Cu_{1.3}$	Expt.	7.6293(1)	8.1466(1)	10.1420(1)	90.000	110.806(8)	90.000	589.260(14)	14.00
$MgCuV_2O_7$	DFT	7.7700	8.2300	10.2200	90.000	110.900	90.000	610.820	
$Ca_2V_2O_7$	Expt.	6.6732(1)	6.9304(1)	7.0248(1)	86.449(1)	63.862(1)	83.679(1)	289.850(9)	3.91
	DFT	6.7500	7.0500	7.1300	85.210	63.760	81.910	301.360	
$CaCuV_2O_7$	Expt.	10.0520(4)	8.8780(3)	10.2011(3)	90.000	91.010(2)	90.000	910.220(6)	7.81
	DFT	10.2600	8.9300	10.3000	90.000	91.710	90.000	943.200	
$Sr_2V_2O_7$	Expt.	7.0690(3)	7.1120(3)	13.0190(5)	9.442(2)	93.760(2)	90.780(2)	644.000(4)	2.25
	DFT	7.1600	7.2200	13.1400	98.840	93.390	90.740	670.960	
$SrCuV_2O_7$	Expt.	14.5096(1)	5.4769(3)	7.4299(5)	90.000	90.000	90.000	590.430(7)	7.68
	DFT	14.6800	5.5200	7.5200	90.000	90.000	90.000	609.550	
β-$Cu_2V_2O_7$	Expt.	7.6994(2)	8.0705(2)	10.1240(2)	90.000	110.282(1)	90.000	590.100(2)	13.48
	DFT	7.8340	8.0820	10.2190	90.000	110.000	90.000	608.170	
α-$Cu_2V_2O_7$	Expt.	20.6953(5)	8.4095(2)	6.4522(1)	90.000	90.000	90.000	1122.92(4)	6.34
	DFT	20.6100	8.8500	6.4500	90.000	90.000	90.000	1175.600	

The structure of $Mg_{0.67}Cu_{1.33}V_2O_7$ is similar to that of β-$Cu_2V_2O_7$. Figure 3-4f shows the crystal structure of monoclinic space group *C*2/*c* $Mg_{0.67}Cu_{1.33}V_2O_7$, which consists of MgO_5/CuO_5 square pyramids connected by V_2O_7. On the other hand, $CaCuV_2O_7$ crystallized in monoclinic space group *P*2/*c* as shown in Figure 3-4g. The structure is made up of CuO_4 square planar, CaO_6/ CaO_7 polyhedral and VO_4 tetrahedra that are linked by sharing an oxygen atom to form V_2O_7. Lastly, $SrCuV_2O_7$ formed a layered structure and crystallized in orthorhombic space group *Pnma* (Figure 3-4h). The structure comprises of SrO_{11} polyhedral, CuO_5 tetragonal pyramids and VO_4 tetrahedra that are linked by sharing oxygen atom to form V_2O_7.

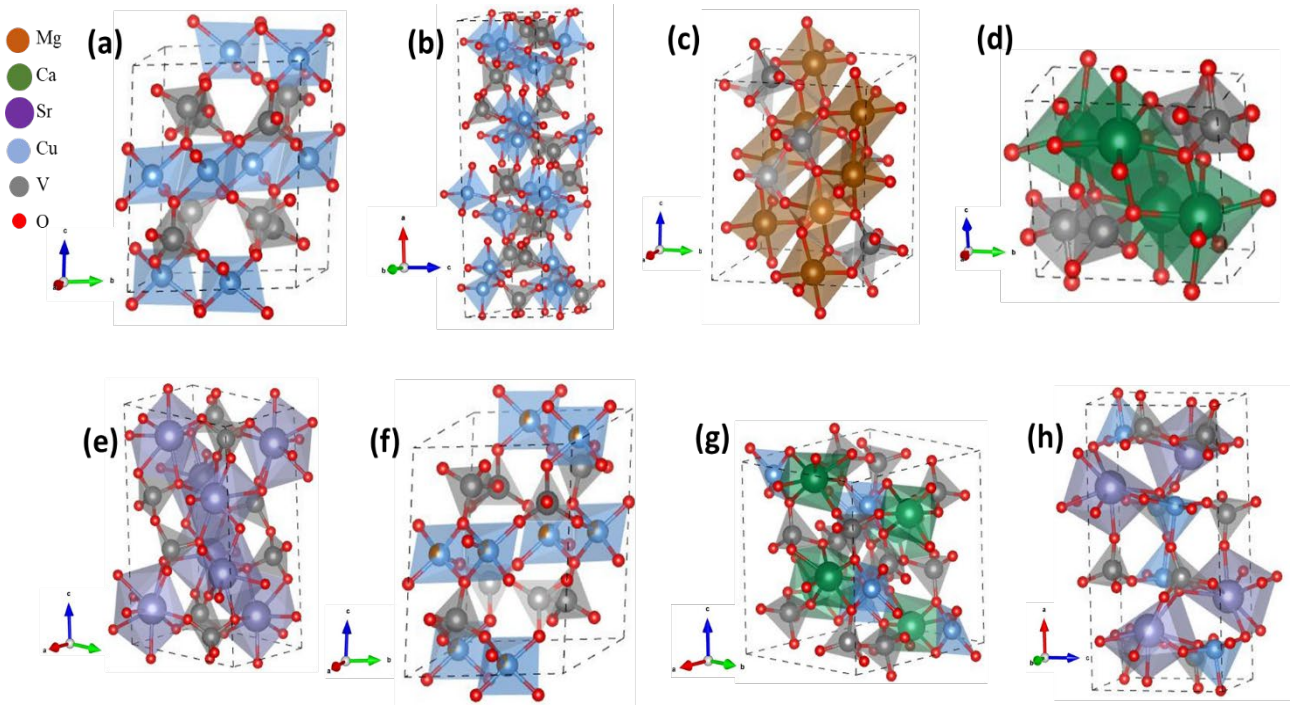

Figure 3-4. Crystal structure for (a) monoclinic β-$Cu_2V_2O_7$, (b) orthorhombic α-$Cu_2V_2O_7$, (c) monoclinic $Mg_2V_2O_7$, (d) triclinic $Ca_2V_2O_7$, (e) triclinic $Sr_2V_2O_7$ (f) monoclinic $Mg_{0.67}Cu_{1.33}V_2O_7$, (g) monoclinic $CaCuV_2O_7$ and, (h) orthorhombic $SrCuV_2O_7$.

The Raman spectra of the end members and solid solutions are shown in Figure 3-5 and Table 3-4. The Raman bands observed in the spectra are consistent with previous reports.[41, 51] The Raman band observed around 1000 - 800 cm^{-1} with strong band at 918 cm^{-1} in β-$Cu_2V_2O_7$ and a broad

band at 904 cm^{-1} in α-$Cu_2V_2O_7$ are assigned to VO_3 symmetric and antisymmetric stretching vibrations (Figure 3-5a, red and black line). The low-intensity bands in both β- and α-polymorphs of $Cu_2V_2O_7$ at around 800 – 500 cm^{-1} are attributed to VOV symmetric and antisymmetric bridge stretching vibrations.[51] Furthermore, the VO_3 and OVO_3 bending vibrations are centered at 400 – 100 cm^{-1}.[51, 53]

In the Raman spectrum of $Mg_2V_2O_7$ presented in Figure 3-5a (blue line), the bands observed at 1000 – 700 cm^{-1} are assigned to VO stretching vibrations in the VO_4 tetrahedra. The VOV bending vibrations were observed in the frequency range of 700 – 500 cm^{-1}, while the bands at approximately 500 – 150 cm^{-1} are assigned to OVO and OMgO bending vibrations.[40] The bands below 150 cm^{-1} are assigned to MgO_6 octahedra's bending vibrations.

The Raman spectrum of $Ca_2V_2O_7$, illustrated in Figure 3-5a (green line), shows bands at 950 – 750 cm^{-1} which were attributed to VO_3 stretching vibrations in the VO_4 tetrahedra and VO_5 square pyramids. Meanwhile, VO_3 bending vibrations were detected in the 500 – 300 cm^{-1} frequency range, followed by the identification of bands at approximately 300 – 100 cm^{-1} as lattice mode of vibrations.[41] Figure 3-5a (purple line) shows the Raman spectrum of $Sr_2V_2O_7$. The Raman bands at approximately 950 - 800 cm^{-1} are assigned to VO_3 symmetric and antisymmetric stretching vibrations.[54] The bands at 800 – 500 cm^{-1} are assigned to VOV stretching vibrations, while the bands below 400 cm^{-1} are due to VO_3 bending vibrations and external lattice vibration.[54]

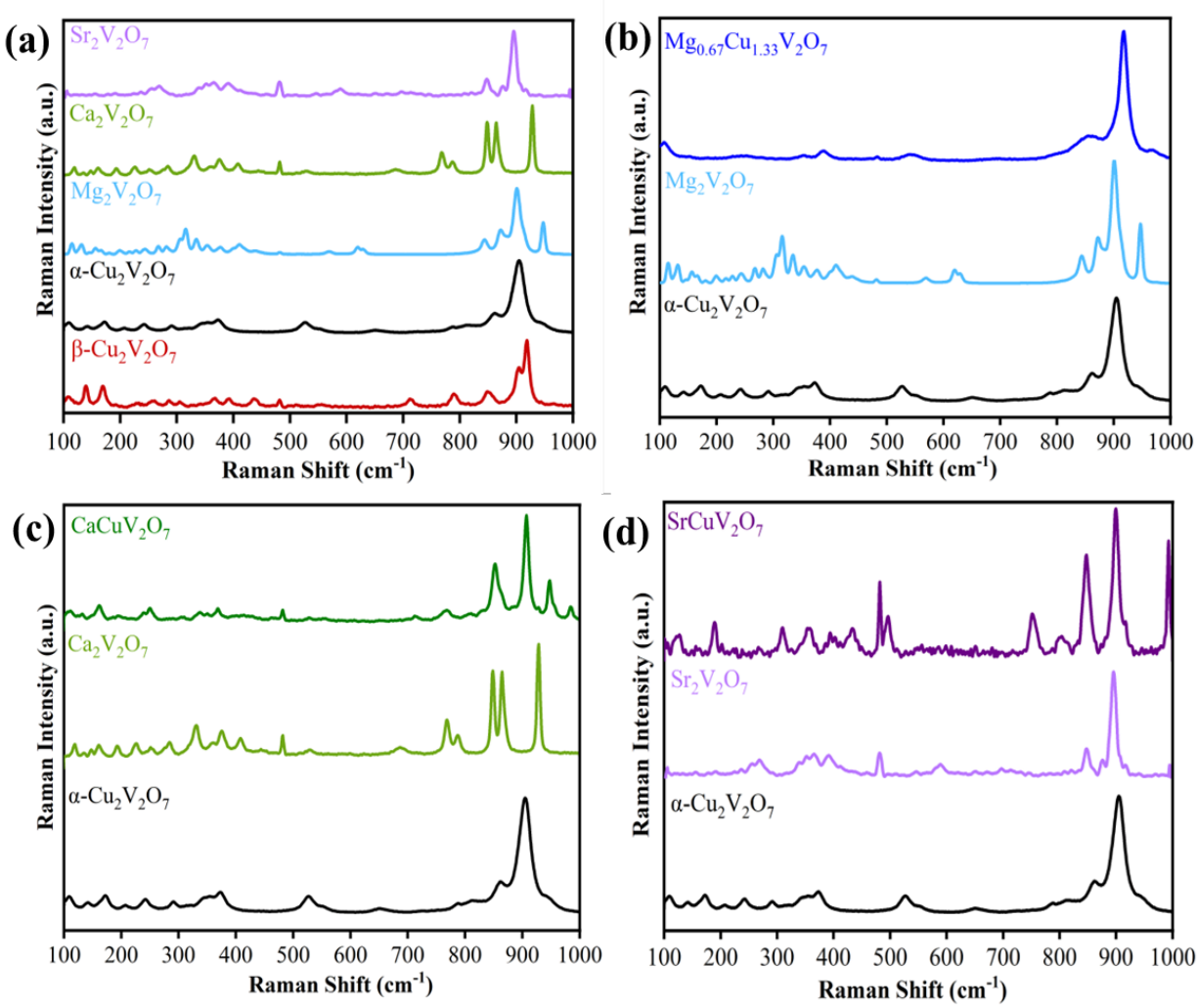

Figure 3-5. Room temperature Raman spectra for the (a) end members β-$Cu_2V_2O_7$, α-$Cu_2V_2O_7$, $Mg_2V_2O_7$, $Ca_2V_2O_7$, and $Sr_2V_2O_7$ and the solid solutions; (b) $Mg_{0.67}Cu_{1.33}V_2O_7$, (c) $CaCuV_2O_7$, (d) $SrCuV_2O_7$.

In Figure 3-5b, the Raman spectra of $Mg_{0.67}Cu_{1.33}V_2O_7$ and the endmembers $Mg_2V_2O_7$ and α-$Cu_2V_2O_7$ are compared. The Raman bands in the spectrum of $Mg_{0.67}Cu_{1.33}V_2O_7$ at approximately 1000 – 800 cm^{-1} are due to VO_3 symmetric and antisymmetric stretching vibrations. The bands between 800 – 500 cm^{-1} [a]re attributed to VOV symmetric and antisymmetric bridge stretching vibrations.[51] Additionally, the VO_3 and OVO_3 bending vibrations are located at approximately 400 – 200 cm^{-1}. Comparison between the Raman spectra of $CaCuV_2O_7$, $Ca_2V_2O_7$ and α-$Cu_2V_2O_7$ is presented in Figure 3-5c. The strong Raman bands at 949, 907 and 853 cm^{-1} are due to VO

symmetric and antisymmetric vibrations in the VO_4 tetrahedra. The bands at 767 and 713 cm^{-1} are assigned to VOV symmetric and antisymmetric stretching vibrations, while the bands at 481, 368, 250 and 162 cm^{-1} are attributed to OVO, VO_3, OCuO and OCaO bending vibrations. The intense peaks between 1000 – 750 cm^{-1} in the spectrum of $SrCuV_2O_7$ shown in Figure 3-5d are attributed to the symmetric and antisymmetric stretching vibrations of VO in VO_4 tetrahedra, whereas the bands observed at 750 – 400 cm^{-1} are assigned to symmetric and antisymmetric VO bending vibrations. Finally, the bands below 400 cm^{-1} are attributed to OVO, SrO and CuO bending vibrations.

The d-spacing values obtained through Rietveld refinement of the PXRD data of β-$Cu_2V_2O_7$, α-$Cu_2V_2O_7$, $Ca_2V_2O_7$, and $CaCuV_2O_7$ were utilized for indexing the selected area electron diffraction, SAED spots in the HR-TEM data of the selected area. The indexed SAED spots are presented in Figure 3-6. There was good agreement between the d-spacings obtained through indexing the SAED spot and that of the PXRD data. To further analyze the end members and the solid solutions, Table 3-5 compares the SAED and PXRD results.

Table 3-4. Comparing the experimental Raman bands from this study and literature for the end members β-$Cu_2V_2O_7$, α-$Cu_2V_2O_7$, $Mg_2V_2O_7$, $Ca_2V_2O_7$, and $Sr_2V_2O_7$ as well as the solid solutions $Mg_{0.67}Cu_{1.33}V_2O_7$, $CaCuV_2O_7$, and $SrCuV_2O_7$.

Sample	Raman shift (cm^{-1})													
β-$Cu_2V_2O_7$	-	943	918	904	850	790	712	480	436	392	366	261	192	139
Ref[51]	-	950	912	-	855	786	-	-	-	398	-	259	192	-
α-$Cu_2V_2O_7$	-	949	904	862	525	372	350	292	242	172	110	-	-	-
Ref[53]	992	920	-	850	553	392	338	275	254	-	111	-	-	-
$Mg_2V_2O_7$	947	901	872	843	618	570	411	377	334	316	131	-	-	-
Ref[40]	946	901	872	843	618	572	-	-	-	-	-	-	-	-
$Ca_2V_2O_7$	928	865	848	788	768	482	408	375	330	284	252	226	192	118
Ref[41]	929	866	850	788	770	-	409	378	333	287	255	227	195	120
$Sr_2V_2O_7$	917	896	876	848	589	480	391	365	269	-	-	-	-	-
Ref[41]	-	897	-	849	589	-	-	365	271	71	-	-	-	-
$Mg0._{67}Cu_{1.33}V_2O_7$	967	918	-	856	798	545	390	354	-	-	-	-	-	-
Ref[51]	959	916	885	849	800	545	398	353	253	-	-	-	-	-
$CaCuV_2O_7$	985	949	907	853	767	713	481	368	250	162	-	-	-	-
$SrCuV_2O_7$	992	900	847	801	752	495	481	433	355	310	189	127	-	-

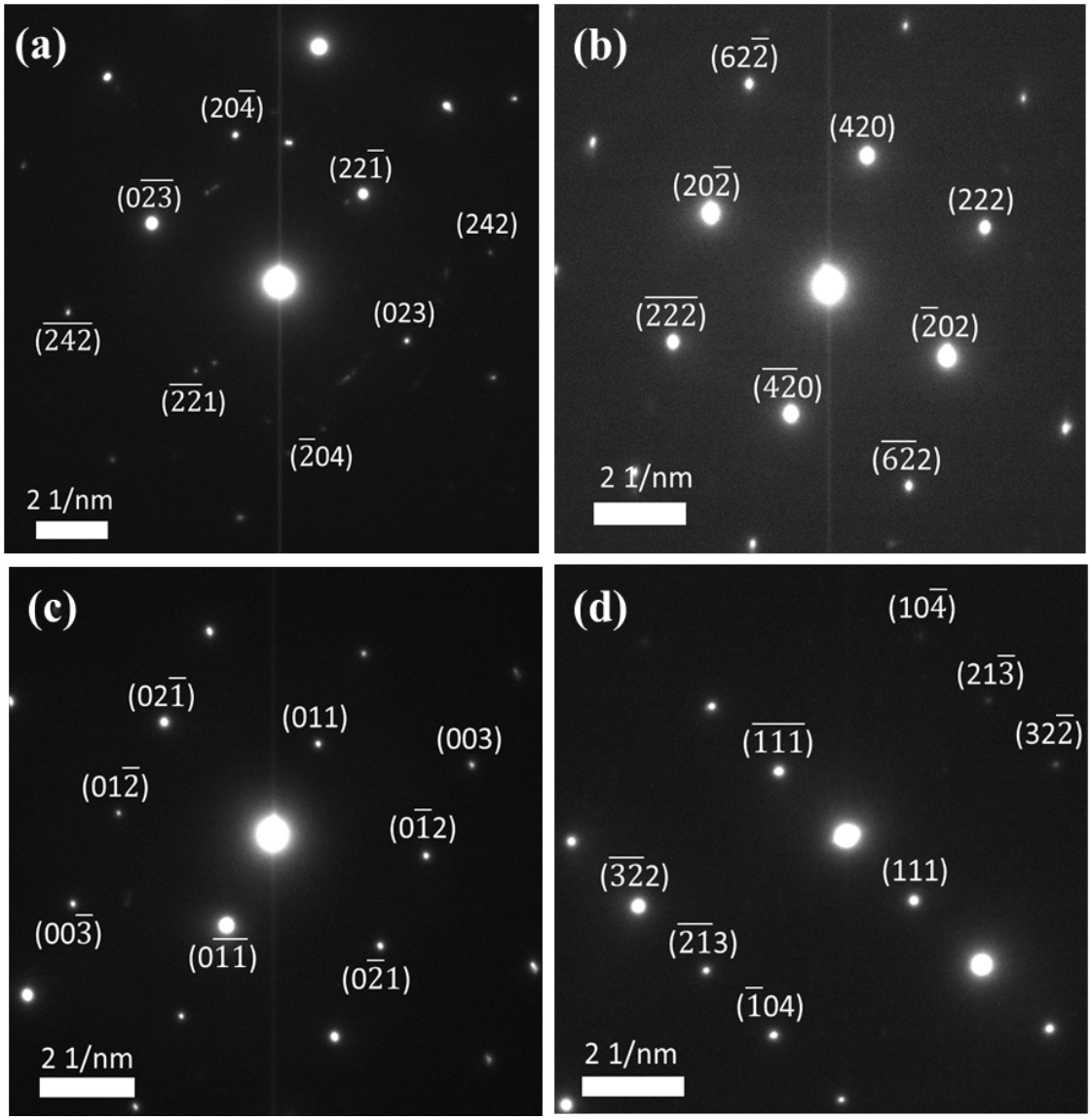

Figure 3-6. SAED patterns for (a) β-$Cu_2V_2O_7$, (b) α-$Cu_2V_2O_7$, (c) $Ca_2V_2O_7$, and (d) $CaCuV_2O_7$. The SAED spots are indexed to the corresponding unit cells illustrated in Figure 3-4.

3.3.2 Optical Properties. In the A-V-O system, we observed a color change when alkaline earth metals were replaced with copper. This change was consistent with our previous report..[25] Specifically, the color changed from light-yellow in $A_2V_2O_7$ to dark orange, emerald green, green and brownish red in $Mg_{0.67}Cu_{1.33}V_2O_7$, $CaCuV_2O_7$, $SrCuV_2O_7$, and $Cu_2V_2O_7$, respectively. Optical absorption spectra in the UV-visible range were measured for the end members and solid solutions, as shown in Figures 3-7a and d. The absorption onsets for β-$Cu_2V_2O_7$, α-$Cu_2V_2O_7$, $Mg_2V_2O_7$,

$Ca_2V_2O_7$, and $Sr_2V_2O_7$ samples were approximately 640, 650, 470, 500 and 450 nm, respectively. Incorporating copper into the A-V-O system resulted in a bathochromic (red) shift in the absorption onset wavelength, which is consistent with the observed color change and our previous report.[25] The absorption onset wavelength for the solid solutions $Mg_{0.67}Cu_{1.33}V_2O_7$, $CaCuV_2O_7$, and $SrCuV_2O_7$ were approximately 620, 570 and 580 nm, respectively. Further explanation is necessary regarding the emergence of optical absorption features in the high-wavelength regime (as shown in Figures 3-7a and d) for $Cu_2V_2O_7$ and the solid solutions. This feature is attributed to the localized ligand field excitation within the square-pyramidal CuO_5 polyhedra, which does not create mobile charge carriers.[25, 30] A similar feature has been observed for CuV_2O_6, $Cu_2V_2O_7$, and $Cu_3V_2O_7$.[10, 25, 30]

Table 3-5. Comparison of estimated d-spacing values from PXRD and SAED data β-$Cu_2V_2O_7$, α-$Cu_2V_2O_7$, $Ca_2V_2O_7$, and $CaCuV_2O_7$.

Sample	d-spacing (Å) XRD	d-spacing (Å) SAED	Plane
β-$Cu_2V_2O_7$	1.558	1.606	(242)
	2.395	2.296	$(20\bar{4})$
	2.478	2.453	(023)
	2.771	2.851	$(22\bar{1})$
α-$Cu_2V_2O_7$	2.051	1.963	$(62\bar{2})$
	2.479	2.503	(222)
	3.074	3.013	$(\bar{2}02)$
	3.254	3.157	(420)
$Ca_2V_2O_7$	2.099	2.162	(003)

	2.846	2.937	$(0\bar{1}2)$
	2.998	2.973	$(02\bar{1})$
	4.682	4.567	(011)
$CaCuV_2O_7$	2.374	2.279	$(\bar{3}\bar{2}2)$
	2.479	2.411	$(10\bar{4})$
	2.699	2.606	$(21\bar{3})$
	5.525	5.433	$(\bar{1}\bar{1}\bar{1})$

In addition, Tauc plots constructed from Kubelka-Munk transformation of DRS data are presented in Figure 3-7.[21, 22] These plots illustrate the direct and indirect energy bandgap for both the end members and solid solutions in Figures 3-7b, e and 3-7c, f respectively. Upon incorporation of copper in the A-V-O system, both the direct and direct band gap values were decreased, suggesting that the band gap value depends on copper substitution.[25, 55]

3.3.3 Electronic and Magnetic Behavior. Apart from the geometric structure, it is also equally important to consider the spin magnetic ordering of Cu^{2+} (d^9 open shell configuration) for proper description of the electronic and optical properties. Magnetic spin ordering has also been considered for other copper vanadate compounds of variant stoichiometries.[24]

Several antiferromagnetic (AFM) and ferromagnetic (FM) configurations were evaluated to find the magnetic ground state for copper pyrovanadates ($Cu_2V_2O_7$) as well as alkali metal substituted copper pyrovanadates, $MCuV_2O_7$ (where M = Mg, Ca, Sr). The calculated exchange energy, i.e., the total energy difference between the lowest energy AFM and FM structures is insignificant, indicating a weak magnetic coupling among Cu^{2+} sites.

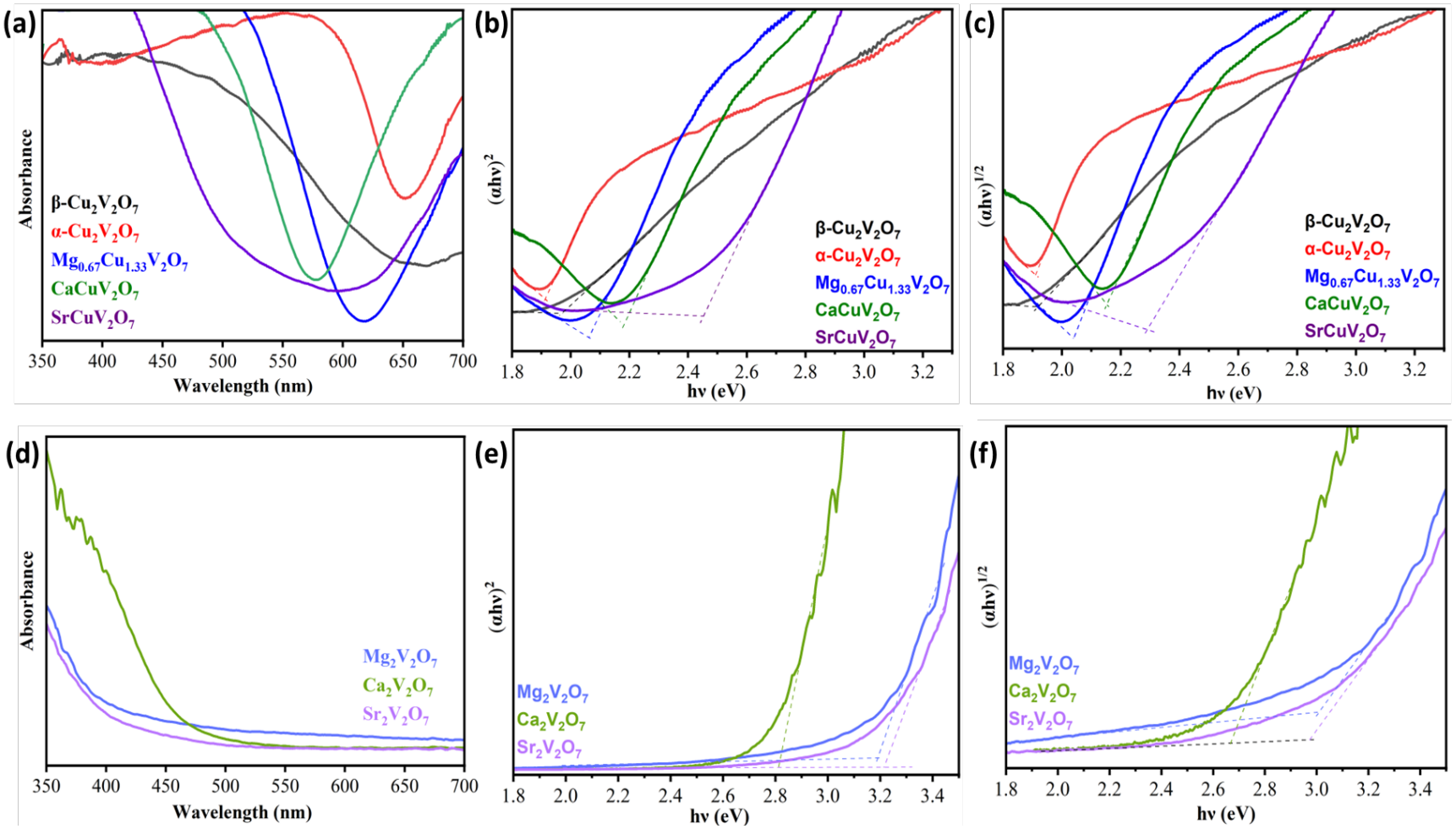

Figure 3-7. (a, d) UV-Vis optical absorption spectra, (b, e) direct Tauc plots, and (c,f) indirect Tauc plots for the end members β-$Cu_2V_2O_7$, α-$Cu_2V_2O_7$, $Mg_2V_2O_7$, $Ca_2V_2O_7$, and $Sr_2V_2O_7$ and the solid solutions$Mg_{0.67}Cu_{1.33}V_2O_7$, (c) $CaCuV_2O_7$, (d) $SrCuV_2O_7$.

Thus, it is more likely that these compounds will crystallize into paramagnetic magnetic ordering under ambient conditions. These results are consistent with other theoretical calculations[56, 57] as well as experimental observations in similar Cu^{2+} based compounds, i.e., α-CuV_2O_6 and β-$Cu_3V_2O_8$.[24] Moreover, $Cu_2V_2O_7$ is antiferromagnetic (AFM) below 15.3 K and becomes paramagnetic above this temperature.[58] Other alkali metal substituted pyrovanadates i.e., $M_2V_2O_7$ where M = Mg, Ca, Sr do not have any magnetic ordering, hence, they are non-magnetic.

For the present study, AFM configurations were adopted for copper pyrovanadates ($Cu_2V_2O_7$) as well as alkali metal substituted copper pyrovanadates, $MCuV_2O_7$ for the final electronic structure calculations because this configuration has slightly lower energy than the lower energy FM configuration. Additionally, the calculated local spin magnetic moment per Cu^{2+} ion was 0.76 μ_B which is very close to the reported value of 0.77 μ_B.[57] Figures 3-8a-e shows the AFM spin orientation of Cu^{2+} ions.

Turning to the electronic structure, Figures 3-8a-e show the calculated orbital projected density of states (PDOS) for copper pyrovanadates ($Cu_2V_2O_7$), and alkali metal substituted copper pyrovanadates $MCuV_2O_7$ in AFM ordering. Figures 3-8f-h show the calculated orbital projected density of states (PDOS) for other alkali metal substituted pyrovanadates. For copper pyrovanadates ($Cu_2V_2O_7$) and alkali metal substituted copper pyrovanadates $MCuV_2O_7$, Cu/V 3*d*-O 2*p* hybridized states contributed to the top of the valence band maximum (VBM) whereas conduction band minimum (CBM) was determined by unoccupied Cu 3*d* e_g states as in $CuWO_4$.[59] There, however, was a small contribution from O 2*p* states to the CBM. It is noteworthy to mention that alkali metal substitution in copper pyrovanadates shifts the CBM to a higher energy direction which is reflected by the increment of the band gap compared to $Cu_2V_2O_7$. For other alkali metal substituted pyrovanadates $M_2V_2O_7$, VBM is constituted with V 3*d*-O 2*p* hybridized states and

CBM is mainly V 3d character with small contribution from O 2p orbitals. Due to complete substitution of Cu atoms by alkali metals, these compounds do not have any mid-gap state which was present in $Cu_2V_2O_7$ and $MCuV_2O_7$. The orbital contributions to the VBM and CBM were in good agreement with those found in recent ab-initio DFT calculations.[57]

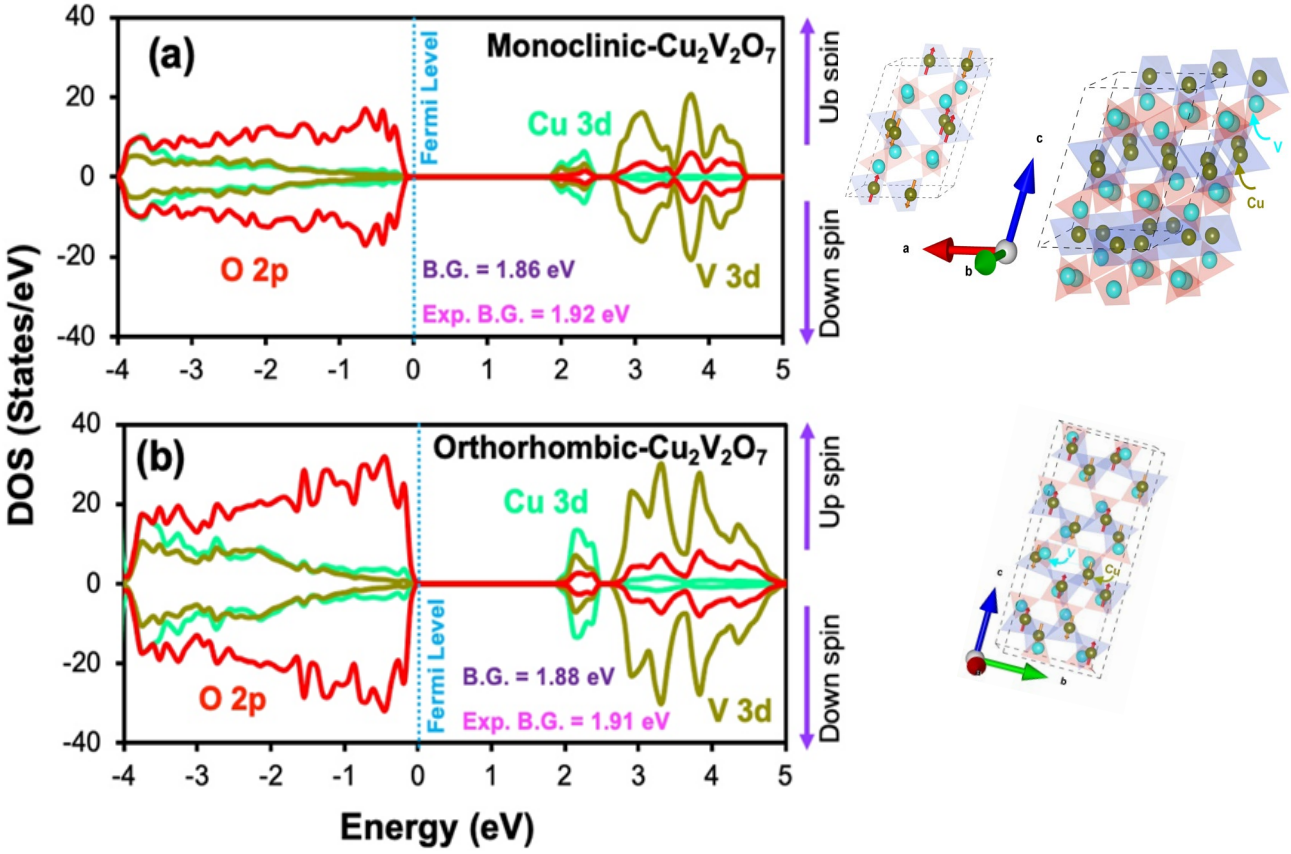

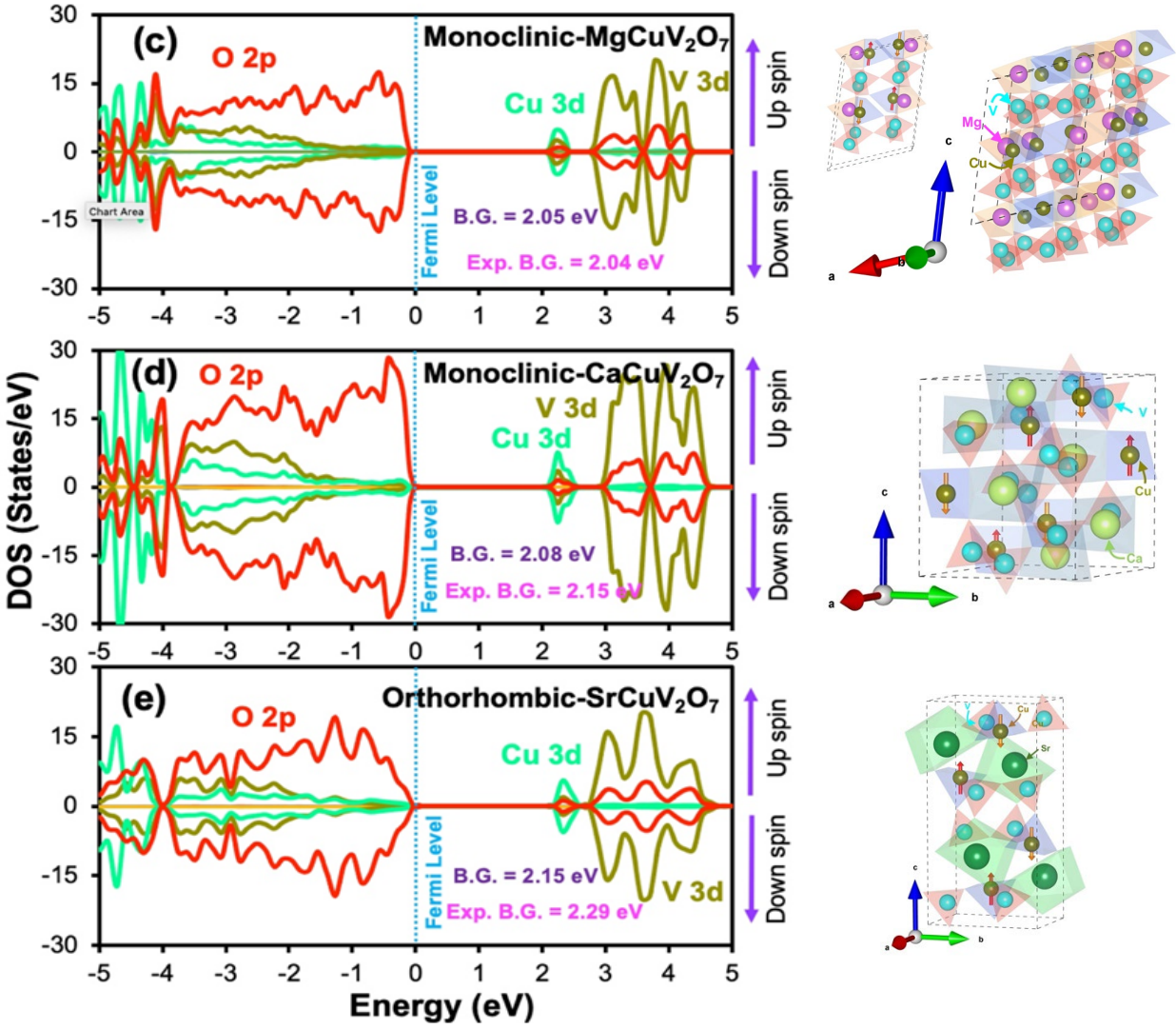
(c)
O 2p
Monoclinic-MgCuV2O7
V 3d
Cu 3d
Up spin
Down spin
Fermi Level
B.G. = 2.05 eV
Exp. B.G. = 2.04 eV
Chart Area
(d)
O 2p
Monoclinic-CaCuV2O7
V 3d
Cu 3d
Up spin
Down spin
Fermi Level
B.G. = 2.08 eV
Exp. B.G. = 2.15 eV
(e)
O 2p
Orthorhombic-SrCuV2O7
Cu 3d
Up spin
Down spin
Fermi Level
B.G. = 2.15 eV
Exp. B.G. = 2.29 eV
V 3d
DOS (States/eV)
Energy (eV)
Mg
V
Cu
Ca
Sr

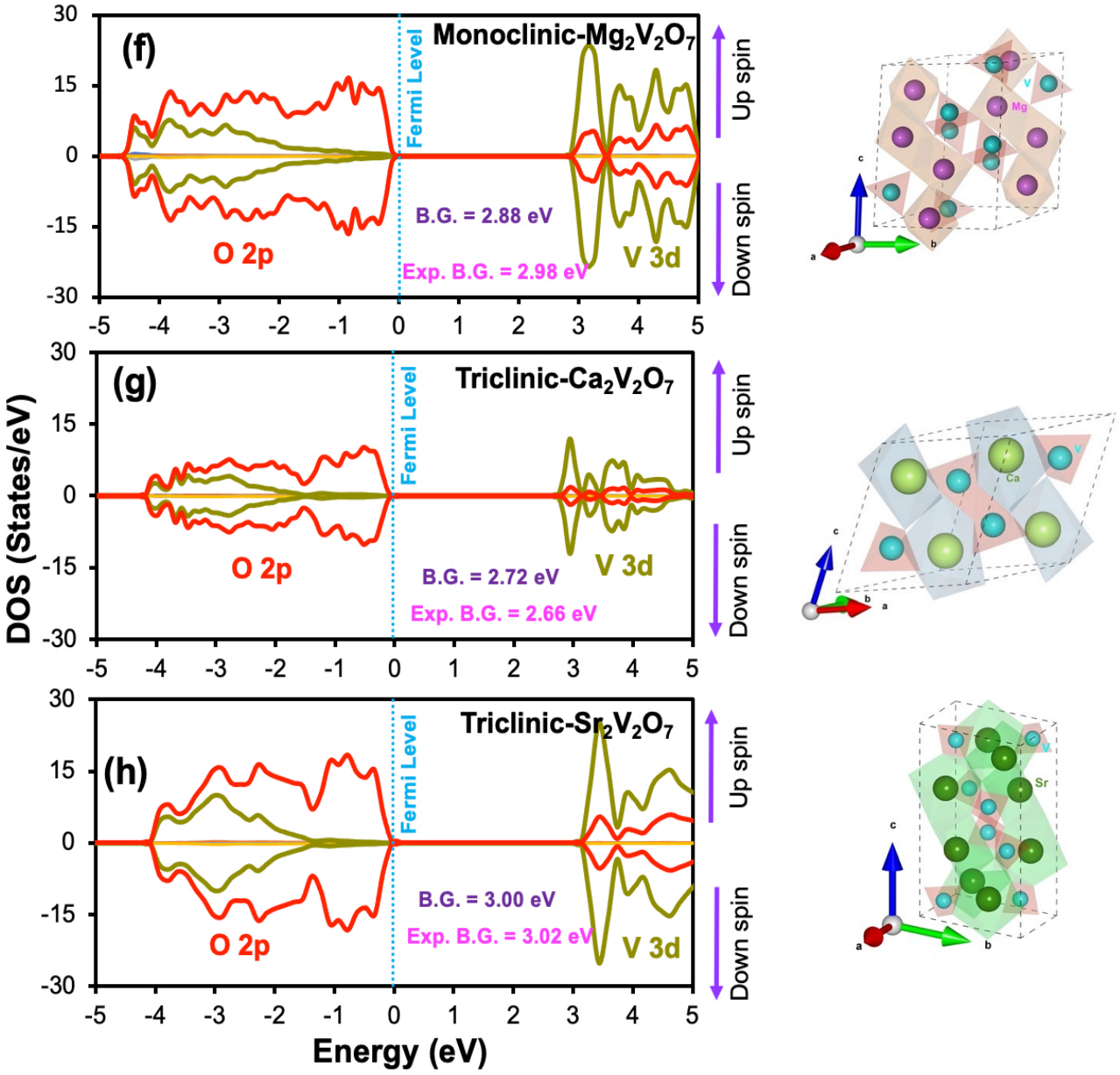

Figure 3-8. Orbital projected density of states for $Cu_2V_2O_7$ and alkali metal substituted copper pyrovanadates i.e., $MCuV_2O_7$ and $M_2V_2O_7$, where M = Mg, Ca, Sr. The Fermi energy level is defined as zeroth energy level and denoted by the blue dotted line. Valence band is defined as below 0 eV states whereas above 0 eV states are defined as conduction band. The spin up and down channel is defined by the purple arrow. The polyhedral model of each compound with their associated magnetic ordering are presented adjacent to each DOS at the right panel.

For $Cu_2V_2O_7$, the calculated minimum gap between the occupied to unoccupied states was 1.85 eV (1.88 eV for orthorhombic symmetry) reasonably close to the experimental value of 1.92 eV (1.91 eV for orthorhombic symmetry). The calculated gap is in good agreement with results from other reported experimental (2.0 eV)[11] as well as ab initio theory calculations.[57] The calculated bandgap for alkali metal substituted copper pyrovanadates i.e., $MCuV_2O_7$ and $M_2V_2O_7$, are in good agreement with experimentally obtained values in this present study. Table 3-6 provides the calculated as well as experimentally obtained band gaps for different pyrovanadate compounds.

Table 3-6. DFT calculated and experimentally obtained bandgap of copper pyrovanadates and alkali metal substituted copper pyrovanadates.

	Band gap (eV)	
Samples	DFT calculation	Experiment
β-$Cu_2V_2O_7$	1.86	1.92
α-$Cu_2V_2O_7$	1.88	1.91
$Mg_{0.67}Cu_{1.33}V_2O_7$	2.05	2.04
$CaCuV_2O_7$	2.08	2.15
$SrCuV_2O_7$	2.15	2.29
$Mg_2V_2O_7$	2.88	2.98
$Ca_2V_2O_7$	2.72	2.66
$Sr_2V_2O_7$	3.00	3.02

As discussed earlier, the optical absorption spectrum of $Cu_2V_2O_7$ and alkali metal substituted copper pyrovanadates, $MCuV_2O_7$ showed a strong absorption below ~700 nm and a weak

absorption above 700 nm (see preceding section) whereas for $Cu_2V_2O_7$, it is around ~1550 nm which we showed in our previous study.[30] The absorption of light below 700 nm is due to the transition between occupied Cu/V 3*d* - O 2*p* hybridized states and unoccupied Cu 3*d* e_g states. Meanwhile, the onset of weak absorption above 700 nm is likely due to the low cross section of the transition between occupied and unoccupied Cu 3*d* e_g orbitals through a dipole forbidden d-d transition. However, for alkali metal substituted copper pyrovanadates, $M_2V_2O_7$, does not have any weak adsorption peak above 700 nm (see preceding section).

3.3.4 Photoelectrochemical Properties. The chopped linear sweep voltammetry (LSV) was used to investigate the PEC activities of thin film electrodes such as β-$Cu_2V_2O_7$, α-$Cu_2V_2O_7$, $Mg_{0.67}Cu_{01.33}V_2O_7$, $CaCuV_2O_7$, and $SrCuV_2O_7$ in 0.1 M borate buffer (pH = 8) under simulated solar light (100 mW/cm2). Both copper vanadate and the solid solutions showed anodic photocurrent under reverse bias potential, suggesting n-type semiconductor behavior of the photoelectrode films (Figure 3-9a). The photoactivity was found to decrease significantly in the solid solutions when alkali earth metals were substituted, which is consistent with previous reports on samples synthesized through conventional solid state and solution combustion methods.[25, 60] The drastic reduction in photoactivity could be attributed to significant increase of bandgap with alkaline earth metal substitution as well as the role played by mid gap states observed in Cu containing compounds (see section 3.3.3 on DFT calculations).[25] Figure 3-9b shows an increase in photocurrent density for all samples when the PEC measurement was carried out in borate + 4 M formate solution, suggesting faster hole transfer kinetics in the presence of hole scavenger.

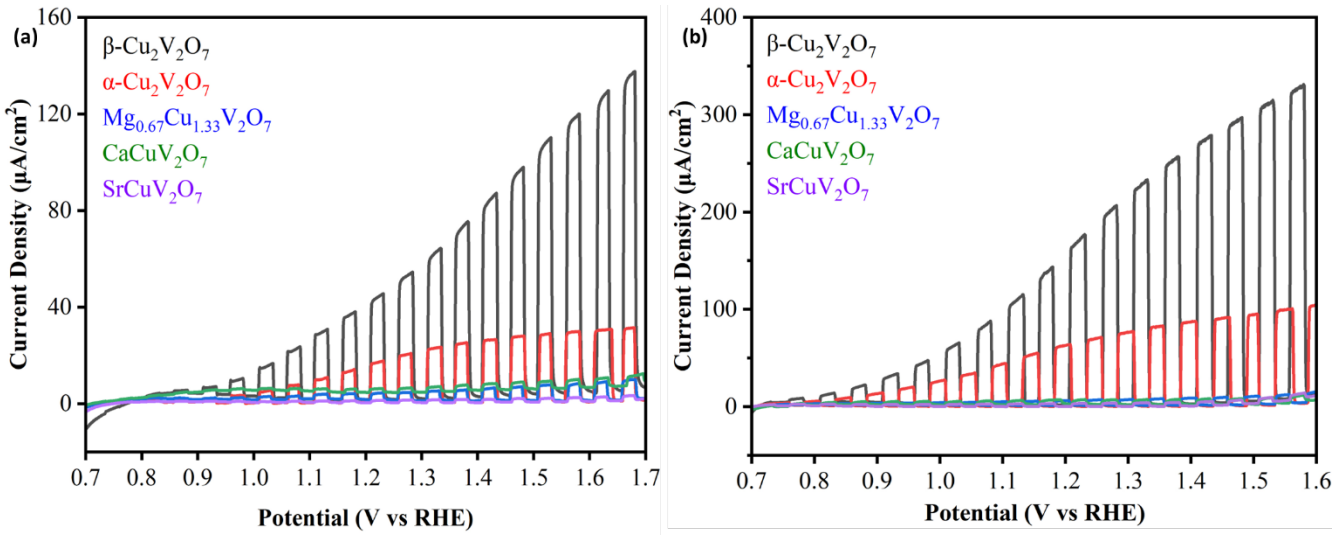

Figure 3-9. Linear sweep voltammogram for β-$Cu_2V_2O_7$, α-$Cu_2V_2O_7$, $Mg_{0.67}Cu_{01.33}V_2O_7$, $CaCuV_2O_7$, and $SrCuV_2O_7$ in (a) 0.1 M borate buffer solution (pH = 8), (b) 0.1 M borate buffer + 4 M formate solution (pH = 8) under front-side illumination. The potential sweep rate was 5 mV/s.

3.4 CONCLUSIONS

Ternary and quaternary copper and alkaline earth metal oxide semiconductors were successfully prepared using a time- and energy-efficient solution combustion synthesis method in this study. To assess their suitability for solar water conversion, a combination of experimental and theoretical approaches was used to investigate the substitution of alkaline earth metals in copper pyrovanadates. Our findings demonstrated that the addition of alkaline earth metals to copper pyrovanadate can change its crystal structure, optoelectronic, and photoelectrochemical properties. Further research is necessary to comprehend the effect of alkaline earth metal substitution on charge separation efficiency, carrier lifetime, and minority carrier diffusion lengths. There is a need for further development of strategies to eliminate the minority phases present in β-$Cu_2V_2O_7$, $CaCuV_2O_7$, and $SrCuV_2O_7$.

3.5 REFERENCES

1. Zhang, M.; Pham, H. K.; Fang, Y.; Tay, Y. F.; Abdi, F. F.; Wong, L. H., The Synergistic Effect of Cation Mixing In Mesoporous $Bi_xFe_{1-x}VO_4$ Heterojunction Photoanodes for Solar Water Splitting. *Journal of Materials Chemistry. A, Materials for Energy and Sustainability* **2019,** *7* (24), 14816-14824.
2. Pihosh, Y.; Turkevych, I.; Mawatari, K.; Uemura, J.; Kazoe, Y.; Kosar, S.; Makita, K.; Sugaya, T.; Matsui, T.; Fujita, D.; Tosa, M.; Kondo, M.; Kitamori, T., Photocatalytic Generation of Hydrogen by Core-Shell $WO_3/BiVO_4$ Nanorods with Ultimate Water Splitting Efficiency. *Scientific Reports* **2015,** *5* (1), 11141.
3. Kim, J. H.; Lee, J. S., Solar Water Splitting: Elaborately Modified $BiVO_4$ Photoanodes for Solar Water Splitting. *Advanced materials (Weinheim)* **2019,** *31* (20), 1806938.
4. Vali, A.; Sarker, H. P.; Jee, H. W.; Kormányos, A.; Firouzan, F.; Myung, N.; Paeng, K. J.; Huda, M. N.; Janáky, C.; Rajeshwar, K., Electrodeposition of Silver Vanadate Films: A Tale of Two Polymorphs. *Chemphyschem* **2019,** *20* (20), 2635-2646.
5. Hong, S.; Burkhow, S. J.; Doughty, R. M.; Cheng, Y.; Ryan, B. J.; Mantravadi, A.; Roling, L. T.; Panthani, M. G.; Osterloh, F. E.; Smith, E. A.; Zaikina, J. V., Local Structural Disorder in Metavanadates MV_2O_6 (M = Zn and Cu) Synthesized by the Deep Eutectic Solvent Route: Photoactive Oxides with Oxygen Vacancies. *Chemistry of Materials* **2021,** *33* (5), 1667-1682.
6. Kumari, S.; Junqueira, J. R. C.; Schuhmann, W.; Ludwig, A., High-Throughput Exploration of Metal Vanadate Thin-Film Systems (M–V–O, M = Cu, Ag, W, Cr, Co, Fe) for Solar Water Splitting: Composition, Structure, Stability, and Photoelectrochemical Properties. *ACS Combinatorial Science* **2020,** *22* (12), 844-857.
7. Guo, W.; Chemelewski, W. D.; Mabayoje, O.; Xiao, P.; Zhang, Y.; Mullins, C. B., Synthesis and Characterization of CuV_2O_6 and $Cu_2V_2O_7$: Two Photoanode Candidates for Photoelectrochemical Water Oxidation. *The Journal of Physical Chemistry C* **2015,** *119* (49), 27220-27227.
8. Seabold, J. A.; Neale, N. R., All First Row Transition Metal Oxide Photoanode for Water Splitting Based on $Cu_3V_2O_8$. *Chemistry of Materials* **2015,** *27* (3), 1005-1013.
9. Zhou, L.; Yan, Q.; Shinde, A.; Guevarra, D.; Newhouse, P. F.; Becerra-Stasiewicz, N.; Chatman, S. M.; Haber, J. A.; Neaton, J. B.; Gregoire, J. M., High Throughput Discovery of Solar Fuels Photoanodes in the $CuO\text{-}V_2O_5$ System. *Advanced Energy Materials* **2015,** *5* (22), 1500968.
10. Jiang, C.-M.; Farmand, M.; Wu, C. H.; Liu, Y.-S.; Guo, J.; Drisdell, W. S.; Cooper, J. K.; Sharp, I. D., Electronic Structure, Optoelectronic Properties, and Photoelectrochemical Characteristics of γ-$Cu_3V_2O_8$ Thin Films. *Chemistry of Materials* **2017,** *29* (7), 3334-3345.
11. Hong, S.; Doughty, R. M.; Osterloh, F. E.; Zaikina, J. V.; Argonne National Lab, A. I. L. A. P. S., Deep Eutectic Solvent Route Synthesis of Zinc and Copper Vanadate n-Type Semiconductors - Mapping Oxygen Vacancies and Their Effect on Photovoltage. *Journal of Materials Chemistry. A, Materials for Energy and Sustainability* **2019,** *7* (19), 1233-12316.

12. Liu, Y.; Li, Q.; Ma, K.; Yang, G.; Wang, C., Graphene Oxide Wrapped CuV_2O_6 Nanobelts as High-Capacity and Long-Life Cathode Materials of Aqueous Zinc-Ion Batteries. *ACS Nano* **2019,** *13* (10), 12081-12089.
13. Morton, C. D.; Slipper, I. J.; Thomas, M. J. K.; Alexander, B. D., Synthesis and Characterisation of Fe–V–O Thin Film Photoanodes. *Journal of Photochemistry and Photobiology. A, Chemistry.* **2010,** *216* (2), 209-214.
14. Rajeshwar, K.; Hossain, M. K.; Macaluso, R. T.; Janáky, C.; Varga, A.; Kulesza, P. J., Review-Copper Oxide-Based Ternary and Quaternary Oxides: Where Solid-State Chemistry Meets Photoelectrochemistry. *Journal of the Electrochemical Society* **2018,** *165* (4), H3192-H3206.
15. Hassan, A.; Iqbal, T.; Tahir, M. B.; Afsheen, S., A Review on Copper Vanadate-Based Nanostructures for Photocatalysis Energy Production. *International Journal of Energy Research* **2019,** *43* (1), 9-28.
16. Nakabayashi, Y.; Nishikawa, M.; Nosaka, Y., Fabrication of Bismuth Copper Vanadate Electrodes Through Feasible Chemical Solution Method for Visible Light-Induced Water Oxidation. *Journal of Applied Electrochemistry* **2016,** *46* (1), 9-16.
17. Liu, H.; Nakamura, R.; Nakato, Y., Bismuth-Copper Vanadate $BiCu_2VO_6$ as a Novel Photocatalyst for Efficient Visible-Light-Driven Oxygen Evolution. *Chemphyschem* **2005,** *6* (12), 2499-2502.
18. Hossain, M. K.; Sotelo, P.; Sarker, H. P.; Galante, M. T.; Kormányos, A.; Longo, C.; Macaluso, R. T.; Huda, M. N.; Janáky, C.; Rajeshwar, K., Rapid One-Pot Synthesis and Photoelectrochemical Properties of Copper Vanadates. *ACS Applied Energy Materials* **2019,** *2* (4), 2837-2847.
19. Toby, B. H., EXPGUI, a Graphical User Interface for GSAS. *Journal of Applied Crystallography* **2001,** *34* (2), 210-213.
20. Perl, J.; Shin, J.; Schümann, J.; Faddegon, B.; Paganetti, H., TOPAS: An innovative proton Monte Carlo platform for research and clinical applications: TOPAS: An innovative proton Monte Carlo platform. *Medical Physics (Lancaster)* **2012,** *39* (11), 6818-6837.
21. Roy, D.; Samu, G. F.; Hossain, M. K.; Janáky, C.; Rajeshwar, K., On the Measured Optical Bandgap Values of Inorganic Oxide Semiconductors For Solar Fuels Generation. *Catalysis Today* **2018,** *300*, 136-144.
22. Tauc, J.; Grigorovici, R.; Vancu, A., Optical Properties and Electronic Structure of Amorphous Germanium. *Physica Status Solidi (b)* **1966,** *15* (2), 627-637.
23. Viezbicke, B. D.; Patel, S.; Davis, B. E.; Birnie Iii, D. P., Evaluation of the Tauc Method for Optical Absorption Edge Determination: ZnO Thin Films as a Model System. *Physica Status Solidi. B: Basic Solid State Physics* **2015,** *252* (8), 1700-1710.
24. Murphy, A. B., Band-Gap Determination from Diffuse Reflectance Measurements of Semiconductor Films, and Application to Photoelectrochemical Water-Splitting. *Solar Energy Materials and Solar Cells* **2007,** *91* (14), 1326-1337.

25. Rawat, A.; Clark, L.; Zhang, C.; Cavin, J.; Sangwan, V. K.; Toth, P. S.; Janáky, C.; Ananth, R.; Goldfine, E.; Bedzyk, M. J.; Weiss, E. A.; Rondinelli, J. M.; Hersam, M. C.; Meletis, E. I.; Rajeshwar, K., Solution Combustion Synthesis and Characterization of Magnesium Copper Vanadates. *Inorganic Chemistry* **2023,** *62* (23), 8903-8913.
26. Hossain, M. K.; Samu, G. F.; Gandha, K.; Santhanagopalan, S.; Liu, J. P.; Janáky, C.; Rajeshwar, K., Solution Combustion Synthesis, Characterization, and Photocatalytic Activity of $CuBi_2O_4$ and Its Nanocomposites with CuO and α-Bi_2O_3. *Journal of Physical Chemistry. C* **2017,** *121* (15), 8252-8261.
27. Kresse, G.; Furthmüller, J., Efficient Iterative Schemes for Ab Initio Total-Energy Calculations using a Plane-Wave Basis Set. *Physical Review. B, Condensed Matter* **1996,** *54* (16), 11169-11186.
28. Perdew, J. P.; Wang, Y. U. E., Accurate and Simple Analytic Representation of the Electron-Gas Correlation Energy. *Physical review. B, Condensed matter* **1992,** *45* (23), 13244-13249.
29. Blöchl, P. E., Projector Augmented-Wave Method. *Physical Review. B, Condensed Matter* **1994,** *50* (24), 17953-17979.
30. Vali, A.; Sarker, H. P.; Heredia Cervera, B.; Rodríguez-Gutiérrez, I.; Hossain, M. K.; Huda, M. N.; Oskam, G.; Rajeshwar, K., Optical, Electrochemical, and Photoelectrochemical Behavior of Copper Pyrovanadate: A Unified Theoretical and Experimental Study. *Journal of Physical Chemistry. C* **2021,** *125* (36), 19609-19620.
31. Tian, C. M.; Jiang, M.; Tang, D.; Qiao, L.; Xiao, H. Y.; Oropeza, F. E.; Hofmann, J. P.; Hensen, E. J. M.; Tadich, A.; Li, W.; Qi, D. C.; Zhang, K. H. L., Elucidating the Electronic Structure of $CuWO_4$ Thin Films for Enhanced Photoelectrochemical Water Splitting. *Journal of Materials Chemistry. A, Materials for Energy and Sustainability* **2019,** *7* (19), 11895-11907.
32. Hermans, Y.; Klein, A.; Sarker, H. P.; Huda, M. N.; Junge, H.; Toupance, T.; Jaegermann, W., Pinning of the Fermi Level in $CuFeO_2$ by Polaron Formation Limiting the Photovoltage for Photochemical Water Splitting. *Advanced Functional Materials* **2020,** *30* (10), 1910432.
33. Momma, K.; Izumi, F., VESTA: A Three-Dimensional Visualization System for Electronic and Structural Analysis. *Journal of Applied Crystallography* **2008,** *41* (3), 653-658.
34. Ahmed, A. M. M.; Abdel Haleem, S. M.; Darewish, M.; El Kaliea, A. S., Effect of Organic Solvents on the Electrodeposition of Copper from Acidified $CuSO_4$. *Journal of Dispersion Science and Technology* **2012,** *33* (6), 898-912.
35. Riveros, G.; Garmendia, A.; Ramírez, D.; Tejos, M.; Grez, P.; Gómez, H.; Dalchiele, E. A., Study of the Electrodeposition of Cu_2O Thin Films from DMSO Solution. *Journal of the Electrochemical Society* **2013,** *160* (1), D28-D33.
36. Wiktor, J.; Reshetnyak, I.; Strach, M.; Scarongella, M.; Buonsanti, R.; Pasquarello, A., Sizable Excitonic Effects Undermining the Photocatalytic Efficiency of β-$Cu_2V_2O_7$. *The Journal of Physical Chemistry Letters* **2018,** *9* (19), 5698-5703.
37. Nagabhushana, G. P.; Nagaraju, G.; Chandrappa, G. T., Synthesis of Bismuth Vanadate: Its Application in H_2 Evolution and Sunlight-Driven Photodegradation. *Journal of Materials Chemistry. A, Materials for Energy and Sustainability* **2013,** *1* (2), 388-394.

38. Kakihana, M., Invited review: Sol-Gel Preparation of High Temperature Superconducting Oxides. *Journal of Sol-gel Science and Technology* **1996,** *6* (1), 7-55.
39. Hossain, M. K.; Sarker, H. P.; Sotelo, P.; Dang, U.; Rodríguez-Gutiérrez, I.; Blawat, J.; Vali, A.; Xie, W.; Oskam, G.; Huda, M. N.; Macaluso, R. T.; Rajeshwar, K., Phase-Pure Copper Vanadate (α-CuV_2O_6): Solution Combustion Synthesis and Characterization. *Chemistry of Materials* **2020,** *32* (14), 6247-6255.
40. Jin, X.; Wang, R.; Zhou, Y.; Lai, J.; Li, J.; Pei, G.; Chen, S.; Wang, X.; Xiang, J.; Zhu, Z.; Lv, X., A Comprehensive Experimental and First-Principles Study on Magnesium-Vanadium Oxides. *Journal of Alloys and Compounds* **2022,** *896*, 162862.
41. Kaur, P.; Khanna, A., Structural, Electrical and Luminescence properties of $M_2V_2O_7$ (M = Mg, Ca, Sr, Ba, Zn). *Journal of Materials Science. Materials in Electronics* **2021,** *32* (16), 21813-21823.
42. Jin, X.; Pei, G.; Jiao, M.; Li, R.; Li, J.; Li, Y.; Wang, R.; Lv, X., Bonding Inhomogeneity and Strong Anharmonicity Induce Ultralow Lattice Thermal Conductivity in Calcium Pyrovanadate. *Journal of Physical Chemistry. C* **2022,** *126* (38), 16492-16498.
43. Thiagarajan, K.; Theerthagiri, J.; Senthil, R. A.; Madhavan, J., Simple and Low Cost Electrode Material Based on $Ca_2V_2O_7$/Pani Nanoplatelets for Supercapacitor Applications. *Journal of Materials Science. Materials in Electronics* **2017,** *28* (22), 17354-17362.
44. Zhang, S.; Mu, W., Fabrication of $Ca_2V_2O_7$ Microspheres and its Application in Lithium-Ion Batteries. *Materials Letters* **2016,** *183*, 311-314.
45. Macías, J.; Yaremchenko, A. A.; Frade, J. R., Redox Transitions in Strontium Vanadates: Electrical Conductivity and Dimensional Changes. *Journal of Alloys and Compounds* **2014,** *601*, 186-194.
46. Baglio, J. A.; Dann, J. N., The Crystal Structure of Beta Strontium Pyrovanadate. *Journal of Solid State Chemistry* **1972,** *4* (1), 87-93.
47. Slobodin, B. V.; Surat, L. L.; Samigullina, R. F., Polymorphism in Copper Pyrovanadate. *Russian Journal of Inorganic Chemistry* **2009,** *54* (5), 797-802.
48. Belik, A. A.; Azuma, M.; Matsuo, A.; Kindo, K.; Takano, M., Low-Dimensional Ferromagnetic Properties of $SrCuV_2O_7$ and $BaCuV_2O_7$. *Inorganic Chemistry* **2005,** *44* (10), 3762-3766.
49. Velikodnyi, Y. A.; Murashova, E. V.; Lepa, E., Crystal Structure of $SrCuV_2O_7$ and the structural family $SrMV_2O_7$ (M=Cu, Zn, Mg, Sr). *Soviet Physics. Crystallography* **1992,** *37* (3), 433-435.
50. Vogt, R.; Mueller-Buschbaum, H. K., The Shift from Planar to Tetrahedral CuO_4 Groups in $CaCuV_2O_7$. *ChemInform* **1991,** *22* (27), 119-126.
51. de Waal, D.; Hutter, C., Vibrational Spectra of two Phases of Copper Pyrovanadate and Some Solid Solutions of Copper and Magnesium Pyrovanadate. *Materials Research Bulletin* **1994,** *29* (8), 843-849.

52. Bhowal, S.; Sannigrahi, J.; Majumdar, S.; Dasgupta, I., A Comparative Study of Electronic, Structural, and Magnetic Properties of α -, β -, and γ − $Cu_2V_2O_7$. *Physical Review. B* **2017,** *95* (7).
53. Fontaine, B.; Benrkia, Y.; Blach, J.-F.; Mathieu, C.; Roussel, P.; Ayesh, A. I.; Sayede, A.; Saitzek, S., Photoelectrochemical Properties of Copper Pyrovanadate (CuVO) Thin Films Synthesized by Pulsed Laser Deposition. *RSC Advances* **2023,** *13* (18), 12161-12174.
54. Baran, E. J.; Botto, I. L.; Pedregosa, J. C.; Aymonino, P. J., ChemInform Abstract: The Vibrational Spectrum of Strontium Divanadate ($Sr_2V_2O_7$) and the Vibrational Properties of the Divanadate Ion. *Chemischer Informationsdienst* **1978,** *9* (21), 41-51.
55. Lakshminarasimhan, N.; Li, J.; Hsu, H.-C.; Subramanian, M. A., Optical Properties of Brannerite-Type Vanadium Oxides, MV_2O_6 (M = Ca, Mg, Mn, Co, Ni, Cu, or Zn). *Journal of Solid State Chemistry* **2022,** *312*, 123279.
56. Abdi, F. F.; Han, L.; Smets, A. H. M.; Zeman, M.; Dam, B.; van de Krol, R., Efficient Solar Water Splitting by Enhanced Charge Separation in a Bismuth Vanadate-Silicon Tandem Photoelectrode. *Nature Communications* **2013,** *4* (1), 2195-2195.
57. Tsirlin, A. A.; Janson, O.; Rosner, H. Beta-$Cu_2V_2O_7$: a spin-$_{1/2}$ Honeycomb Lattice System; Cornell University Library, arXiv.org: Ithaca, 2010.
58. Touaiher, M.; Rissouli, K.; Benkhouja, K.; Taibi, M.; Aride, J.; Boukhari, A.; Heulin, B., Crystal Structures and Magnetic Properties of $M_2V_2O_7$ (M=Co, Ni and Cu) Compounds. *Materials Chemistry and Physics* **2004,** *85* (1), 41-46.
59. Clark, G. M.; Garlick, R., Formation and Properties of Copper(II) Divanadate(V). *Journal of Inorganic & Nuclear Chemistry* **1978,** *40* (7), 1347-1349.
60. Li, P.; Zhou, W.; Wang, X.; Zhang, Y.; Umezawa, N.; Abe, H.; Ye, J.; Wang, D., Effects of Cation Concentration on Photocatalytic Performance over Magnesium Vanadates. *APL Materials* **2015,** *3* (10), 104405-104405-6.

CHAPTER 4

CATION ORDERING AND BANDGAPS IN $NaPrS_2$

ABSTRACT

Controlling a material's structural and optical properties is important to materials design. By identifying key synthetic parameters of $NaPrS_2$, we were able to control cation ordering and therefore, optical bandgaps. Powder X-ray diffraction was used to confirm the preparation of two unique polymorphs of $NaPrS_2$ for the first time. These polymorphs adopt either disordered cubic ($Fm\bar{3}m$) or layered rhombohedral structures ($R\bar{3}m$). Insight into electronic properties from band gap measurements will also be discussed with the view of examining the effect of local structure of the lanthanide site on the optical properties of the ternary rare earth sulfides. Additionally, the long-range order parameter was employed to establish the dependence of the degree of ordering in rhombohedral $NaPrS_2$ on cooling rate. This study demonstrates that cation ordering leads to enlargement of the bandgap compared to the disordered cubic structure which shifts the energy bandgap to a lower energy.

4.1 INTRODUCTION

Chalcogenide semiconductors have been investigated for optoelectronic applications due to their tunable bandgaps and high carrier mobilities [1-3]. Bandgap tuning is a powerful tool for materials design and enhancing device performance in photovoltaics, photocatalytic water splitting, thermoelectrics, and light-emitting diodes [4-10]. The bandgap of $Cu_3NbS_{4-x}Se_x$ has been controlled for photovoltaic and p-type transparent semiconductor applications by partial substitution of sulfur with selenium [11]. Thus, it was shown that the optical bandgap $Cu_3NbS_{4-x}Se_x$ series can be tuned from 2.6 eV for Cu_3NbS_4 to 2.2 eV for Cu_3NbSe_4 [11]. Previously, our group demonstrated that $Ca(La_{1-x}Ce_x)_2S_4$ ($0 \leq x \leq 1$) exhibited photoelectrochemical activity as a photocatalyst for water splitting and its optical bandgap can be tuned by varying the f electron density [12]. The optical bandgap of $Ca(La_{1-x}Ce_x)_2S_4$ shifted from 3.20 eV in $CaLa_2S_4$ where f electron density was absent to 2.15 eV in $CaCe_2S_4$ [12]. Further, bandgap tunable $Cu(In,Ga)S_2$ photocathode for photoelectrochemical water splitting was developed by varying the Ga and In content [13]. $Cu(In,Ga)S_2$ photocathode has a bandgap ranging from 2.05 to 2.45 eV depending on the molar ratio of In and Ga in $Cu(In,Ga)Se_2$ precursor [13].

Investigation into the discovery of new materials with tunable bandgaps by utilizing order-disorder transition for light-emitting diodes, batteries and solar cell applications has been attracting attention in recent years [14-16]. An order-disorder phase transition involves the transformation of an ordered phase, where the cations are occupying a specific lattice site to a disordered phase, where the cations are randomly distributed in the cation sublattice. For instance, an argyrodite, $Li_7Zn_{0.5}SiS_6$ which adopts a tetragonal $I\bar{4}$ structure with ordered Li and Zn sites at room temperature undergoes a phase transition at 138 °C to form a higher symmetry disordered $F\bar{4}3m$ structure [17]. Similarly, a potential thermoelectric material, $CuFeS_2$ with an ordered tetragonal $I\bar{4}2d$

structure was transformed into disordered $F\bar{4}3m$, resulting in a decrease of lattice thermal conductivity from 9.0 $Wm^{-1}K^{-1}$ in the tetragonal phase to 1.5 $Wm^{-1}K^{-1}$ in the cubic phase [4].

Ternary rare-earth chalcogenides, $ALnQ_2$ (A = alkali metal; Ln = lanthanide metal; Q = chalcogenide) are interesting for their optical and magnetic properties. $KLnS_2$ (Ln = Nd, Ho, Er and Lu) have been identified by first-principles calculations as potential ferromagnetic semiconductors [18]. Along with high melting point and hardness, the transparency of $NaLaS_2$ in the IR-range makes it a prime candidate for IR windows [19]. Eu-doped $ALnS_2$ have been studied for their strong emission across the entire visible range and have been patented as scintillators and phosphors for image displays [20]. Ternary gadolinium sulfides, $AGdS_2$ (A = Li, Na, K, Rb and Cs) have been investigated as potential materials for white LED, X-ray phosphors, photovoltaic and photoelectrochemical devices [21, 22]. $NaLnS_2$ (Ln = Nd – Yb) also contains a triangular lattice of Ln^{3+} ions, hence, they have been studied intensely as quantum spin liquid materials [23-25].

$NaLnS_2$ adopts either the disordered NaCl or layered α-$NaFeO_2$ structure types, shown in Figure 4-1. The NaS_6 and LnS_6 octahedra are randomly distributed in a cubic unit cell; alternatively, the NaS_6 and LnS_6 octahedra are ordered into two-dimensional layers along the c-axis in the rhombohedral α-$NaFeO_2$ type. The stability of these two structure types has been rationalized via the Ln^{3+}/Na^{+} radius ratio [26]. For example, the cubic NaCl structure type (herein referred to as C-type) has been reported for $NaLnS_2$ (Ln = La – Pr) where the Ln^{3+}/Na^{+} ratio > 0.97, and the α-$NaFeO_2$ structure type (herein referred to as R-type) has been reported for $NaLnS_2$ (Ln = Eu – Y)

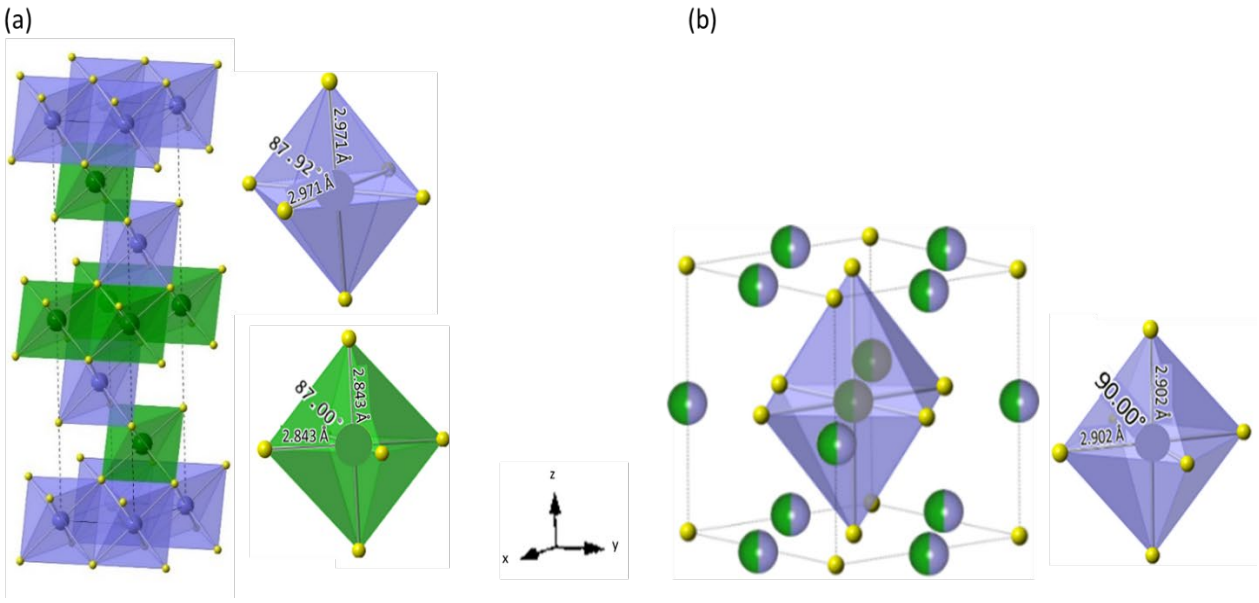

Figure 4-1. Crystal structures of $NaPrS_2$: (a) Rhombohedral structure and experimental NaS_6 and PrS_6 octahedrons and (b) cubic structure and NaS_6 octahedra. Yellow atoms, S; green atoms, Pr; purple atoms, Na.

with Ln^{3+}/Na^{+} ratios < 0.93 [26]. $NaNdS_2$ and $NaSmS_2$ with intermediate Ln^{3+}/Na^{+} ratio ~ 0.96 can crystallize in both C and R-types, and mixtures of structure types are also observed for a wide range of Ln in $LiLnS_2$ (Ln = Tb – Y) and $CsLnS_2$ (Ln = Pr – Lu) [26]. Because these materials are powders, separating these two phases in a mixture is extremely difficult. A thorough analysis of bond valence sums suggest that underbonding of Ln^{3+}, *c/a* ratios and Ln-S interatomic distances must also be considered when considering the stability of NaCl and α-$NaFeO_2$ structure types [27]. Ohtani et al reported an order-disorder transition in $ALnQ_2$. The ordered α-$NaFeO_2$ structure type was transformed into a disordered cubic structure above the critical temperature, T_c (623 – 887 °C). [26].

Given the oxophilic nature of rare-earth metals, it is not surprising to find that oxysulfide impurities, namely Ln_2O_2S tend to plague the syntheses of $ALnS_2$ materials [20, 23, 25, 26, 28-33].

Although they are present in relatively low concentrations, impurities can interfere with material performance. For example, La_2O_2S reduces IR transmission of $NaLaS_2$ to less than 46% [34, 35].

We explored synthetic pathways to address challenges of mixed phases and oxysulfide impurities. Synthetic routes towards $NaLnS_2$ generally fall under two categories – metathesis accompanied by sulfidization or molten polysulfide flux. Metathesis reactions typically involve heating lanthanide-containing reagents, e.g., $LnCl_3$, LnOCl, Ln_2S_3, under flowing H_2S or CS_2 gas [28]. The utilization of such toxic and corrosive reagents is unappealing, especially if syntheses were to be scaled up for production. Alternatively, molten polysulfide fluxes yield reactive S_n^{2-} species to produce a plethora of ternary sulfides [36-38], including $NaGdS_2$ [39], and offers the advantages of lower synthetic temperatures without toxic and corrosive reagents. $ALnS_2$ have been produced by chemoaffinity-mediated synthetic strategy using co-thermolysis which allow the control of sizes and morphologies for the targeted material [18, 27, 28, 40, 41].

We used the flux method and variable cooling rates for the synthesis of $NaPrS_2$ to drive cation ordering, thereby stabilizing one structure type over another. During our work, we discovered that $NaPrS_2$ crystallizes in both C and R structure types, whereas previous reports showed only the existence of C-$NaPrS_2$ [23, 27, 30, 42]. An order-disorder phase transition was observed upon heating the R structure at 850 °C. We also identify routes that drastically reduce oxysulfide impurities. We evaluate the long – range order parameter of various R-$NaPrS_2$ samples using Bragg-Williams equation. Our results indicate that cation ordering dramatically affects the optical band gap of $NaPrS_2$.

4.2 MATERIALS AND METHODS

4.2.1 Synthesis

Pr (Alfa Aesar, 98.5%), Na_2S (Alfa Aesar) and S (Alfa Aesar, 99.5%) were used as received.

Polycrystalline samples of $NaPrS_2$ were obtained via the high temperature solid state method. A Pr rod was manipulated inside a N_2-filled glove box. The exterior of the rod was filed away to remove the surface oxide, and pieces of the rod were cut. Stoichiometric ratios of Pr and S powders were ground with an excess (10% by weight) of Na_2S and subsequently placed inside a graphite crucible. The crucible containing the powder mixture was inserted into a fused silica tube and sealed under vacuum. $NaPrS_2$ powders were obtained by positioning the ampoules in a programmable electric resistance furnace, heating to 850 °C at 10 °C/h, dwelling at this temperature for 48 h and cooling to room temperature at various rates, ranging from 5°C/h to quenching. C-$NaPrS_2$ was obtained by quenching and R-$NaPrS_2$ through slow cooling to room temperature from 850 °C. To remove traces of excess Na_2S, the product was washed several times with distilled water and dried at room temperature for a day.

4.2.2 Powder X-ray diffraction (PXRD)

$NaPrS_2$ samples were characterized by PXRD at room temperature on a PANalytical Empyrean diffractometer (Bragg-Brentano HD optical module and an X'Celerator detector, Cu Kα, λ = 1.5406 Å). The data were collected at 45 kV and 40 mA between 2θ angle range of 10 - 120° with a step size of 2θ = 0.004° and scan speed of 0.021 °/s. Lattice parameters, isotropic displacement parameters and site occupancies were determined by Rietveld refinement of the PXRD data using Highscore package [43]. Structural data on C-$NaPrS_2$ [44] and R-$NaNdS_2$ [30] were

used as starting models for structure refinement, respectively. Small amounts (less than 3%) of Pr_2O_2S impurity was detected in all the samples.

4.2.3 Diffuse reflectance spectroscopy (DRS)

DRS measurements were carried out between 200 – 1000 nm using a UV/Vis Lambda 365 instrument at room temperature. $BaSO_4$ was used as reference for measurement of optical band gaps by employing Tauc plots. Kubelka–Munk function $\alpha/S = (1 - R)^2 /2R$, (α = absorption coefficient, S = scattering coefficient, R = reflectance) was used to calculate absorption coefficient from the DRS data [45].

4.3 RESULTS AND DISCUSSION

4.3.1 X-ray diffraction

Figure 4-1 compares the crystal structures of R- and C-$NaPrS_2$. Diffraction experiments reveal that $NaPrS_2$ adopts both disordered cubic NaCl and rhombohedral layered α-$NaFeO_2$ (space group, $R\bar{3}m$) structure types. R-$NaPrS_2$ consists of edge-sharing NaS_6 and PrS_6 octahedra, which order among alternating layers along the c-axis. In C-$NaPrS_2$, on the other hand, both Na and Pr randomly occupy the corner-sharing octahedral site, therefore cubic symmetry is observed.

The bond angles S-Na-S and S-Pr-S were 87.92° and 87.00°, respectively, this suggests that both NaS_6 and PrS_6 octahedra are distorted (see Figure 4-1a). The bond length of Na-S (2.971 Å) is longer in R-$NaPrS_2$ than in C-$NaPrS_2$ (Na-S, 2.902 Å), also indicating the presence of distorted octahedra in the former. In R-$NaPrS_2$, Pr-S bond length is less than Na-S, suggesting more ionic nature in the later. From the Rietveld refinement of C-$NaPrS_2$ presented in Figure 4-2a, the following were obtained; unit cell a = b = c = 5.7959 Å, R_p = 7.15%, R_{wp} = 9.32% and χ^2 =1.34. The Rietveld refinement plot of PXRD data of R-$NaPrS_2$ is shown in Figure 4-2b (as well as Figure

4-3a,b). From the Rietveld refinement of R- $NaPrS_2$ prepared with a 20 °C/h cooling rate, the unit cell was determined to be: a = b = 4.125 Å, c = 19.981 Å, (R_p = 7.11%, R_{wp} = 9.17% and χ^2 =1.44).

(a)

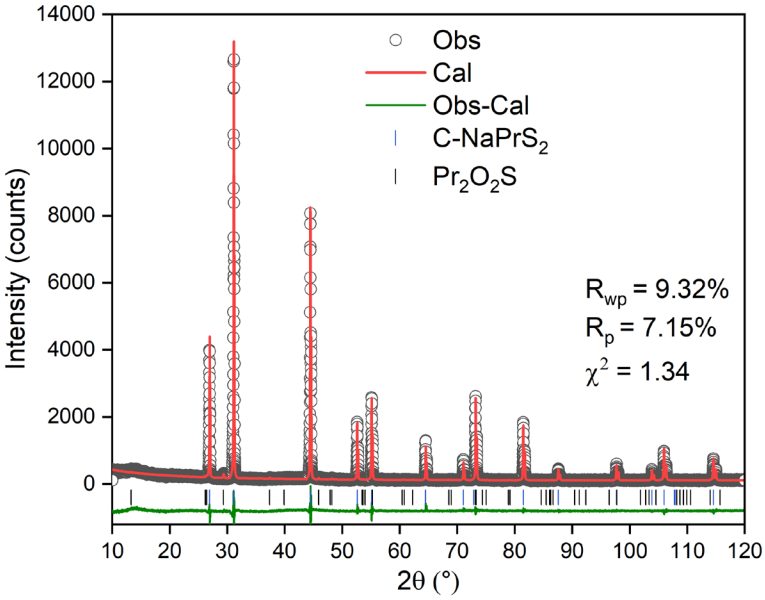

(b)

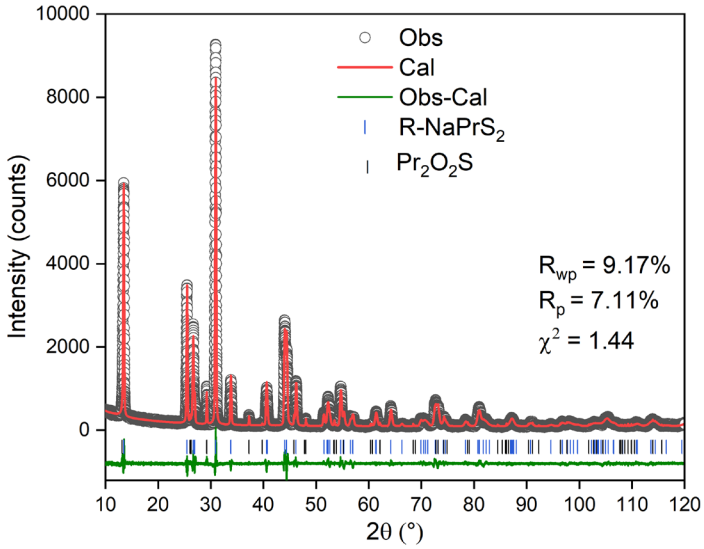

Figure 4- 2. Rietveld refinement plot from powder XRD data for (a) C-$NaPrS_2$ and (b) R-$NaPrS_2$ at 20 °C/h cooling rate.

(a)

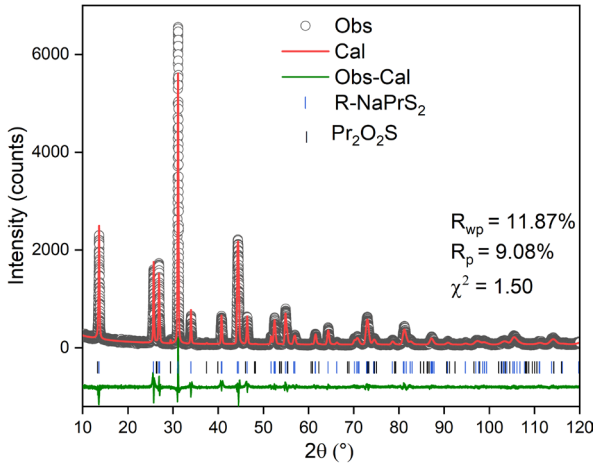

(b)

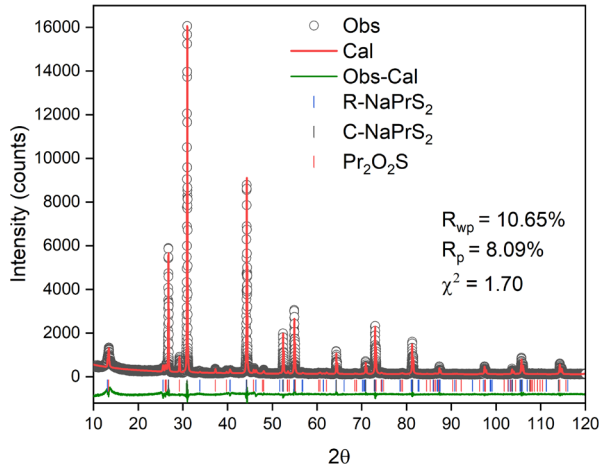

Figure 4-3. Rietveld refinement plot from powder XRD data for rhombohedral $NaPrS_2$ at (a) 50 and (b) 75 °C/h cooling rate.

4.3.2 Effect of synthetic parameters

Polycrystalline ternary praseodymium sulfides were prepared via reaction of stoichiometric amount of Pr, S and Na_2S at 850 °C in graphite crucible sealed in evacuated quartz tube, and the resulting phases were identified by PXRD data analysis. First, to explore the optimum stoichiometric composition for synthesizing phase pure C- or R-$NaPrS_2$, we added excess Na_2S amount with weight percent 10, 20 and 30 (Figure 4-4). A mixture of $NaPrS_2$ and Pr_2S_3 phases were identified when less than 10% excess sulfide flux was used, in good agreement with the

stability of Ln_2S_3 in the presence of small amount of sodium ion [46, 47]. Phase pure C- or R-$NaPrS_2$ were detected by PXRD when 10% excess of Na_2S was used, whereas only C-$NaPrS_2$ was identified when the excess sulfide flux was greater than 20%. We could identify trace amounts of Pr_2O_2S in all the samples which was suppressed in the presence of a large excess of sulfide flux. This suggests that $NaPrS_2$ can be best prepared in the presence of excess flux which agrees with previously reported work [28, 32].

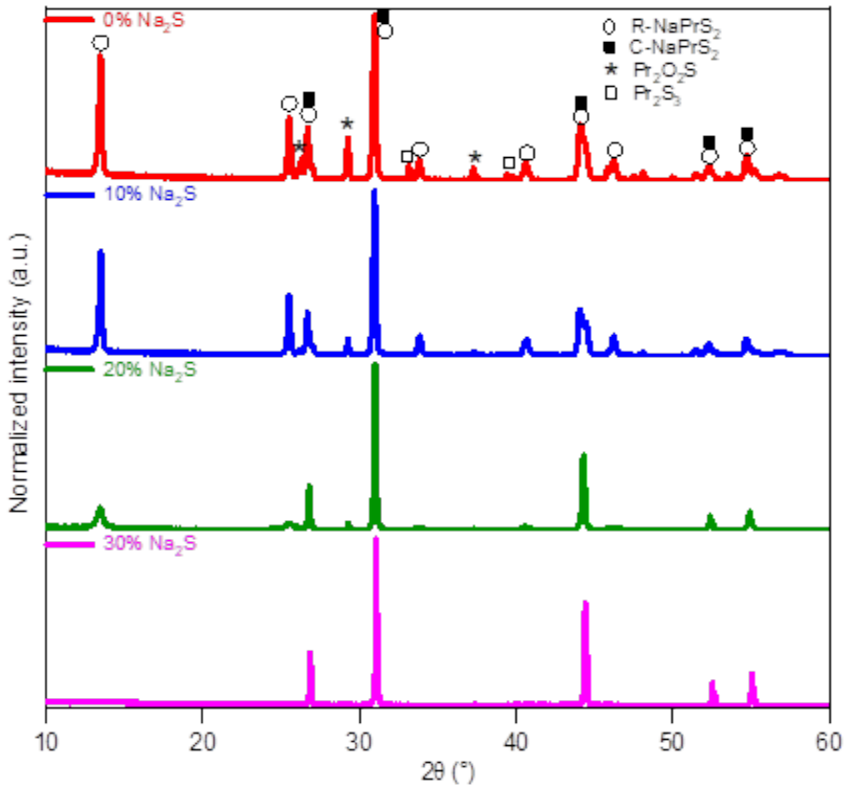

Figure 4-4. Powder XRD patterns for $NaPrS_2$ showing the influence of excess Na_2S in the synthesis of $NaPrS_2$.

A series of R-$NaPrS_2$ samples were prepared at various cooling rates; 5, 10, 20, 50 and 75 °C/h with an excess amount of 10% by mass of Na_2S. There were Pr_2O_2S, $Pr_2O_2S_2$, Pr_2S_3 and/or unidentified impurity peaks detected when slower cooling rates; 5 and 10 °C/h were used. A slower

cooling rate is not suitable for the synthesis of phase pure R-$NaPrS_2$ because sodium sulfide evaporates more rapidly at higher temperature, exchange of oxygen with quartz (SiO_2) tube and oxysulfides are thermodynamically more stable than the sulfides [29], as such, further studies we could not be performed on the samples prepared at 5 and 10 °C/h cooling rates.

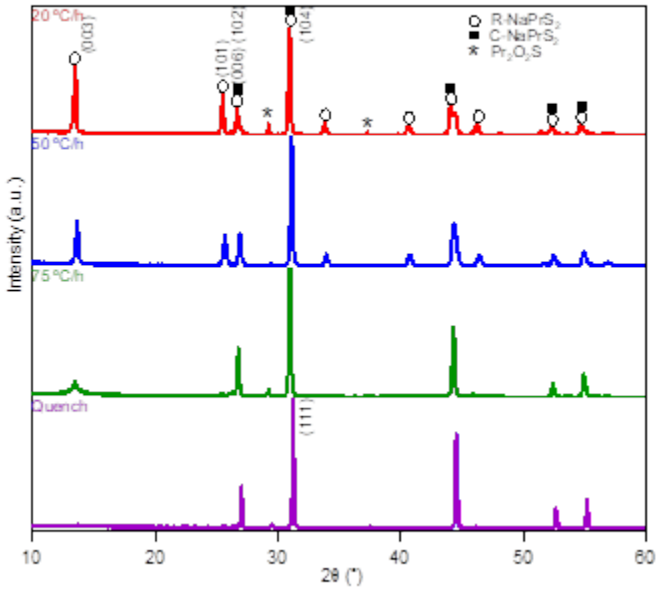

Figure 4- 5. Powder XRD patterns for $NaPrS_2$ synthesized at different cooling rates.

Figure 4-5 shows the normalized powder XRD patterns for series of $NaPrS_2$ prepared at various cooling rates. The XRD patterns of cubic and rhombohedral polymorphs of $NaPrS_2$ are represented by square and open circle symbols, respectively and that of Pr_2O_2S impurity by asterisks. The disordered cubic phase shows only the fundamental reflections, which are represented by square symbols, whereas the reflections represented by both open circle and square indicates superlattice reflections. From the PXRD patterns presented in Figure 4-5, the intensity of superlattice reflections such as (003) and (101) diminished markedly with increasing cooling rates whereas the intensities of fundamental reflections were independent of the cooling rate. The

observed difference in the intensity of superlattice reflections with changing cooling rate suggests variation in the degree of ordering. The (003) and (101) planes contain Na and Pr, respectively, as such, it is not surprising to see variation in their peak intensities with ordering (Figure 4-6). In the rhombohedral phase, Na and Pr atoms are packed along alternate (111) cubic planes to form an ordered structure, and the (006) peak in R-$NaPrS_2$ corresponds to (111) peak in the cubic phase.

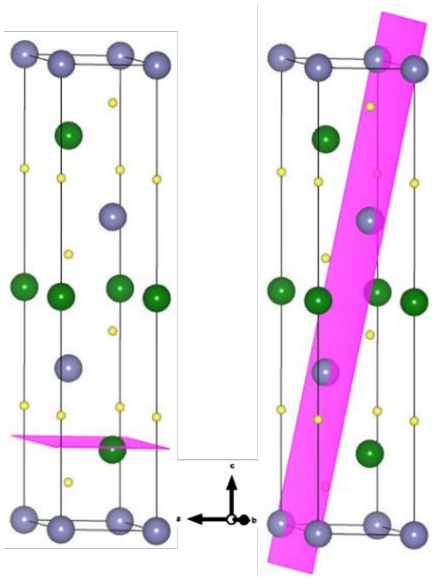

Figure 4-6. Crystal structure for the (003) (left) and (101) (right) planes of R-$NaPrS_2$ which contain Pr and Na atoms, respectively.

In order to understand the variation of (003) and (101) peak intensities with ordering, we compare the peak area of superlattice reflection which disappear as cation order disappears and that of a fundamental reflection which is independent of the degree of cation order [48]. The (003) and (101) peaks which contain Na and Pr, respectively were used as superlattice reflections and (006) peak is the fundamental reflection. The value of the peak area was determined after Rietveld refinement of XRD profiles. Figure 4-7 shows the dependence of peak area ratio of superlattice to peak area of fundamental reflections on the long-range order parameter. A linear relationship was seen between $A_{003,101}/A_{006}$ and long-range order parameter as we varied the cooling rate, indicating

the disappearance of superlattice reflection with cation disorder. As we decreased the cooling rate, the peak area ratio of superlattice to peak area of fundamental reflections and the long-range order parameter increased (Figure 4-7).

The cation order in R-$NaPrS_2$ was investigated using the Bragg-Williams long-range order parameter, here represented as S [16]. The long-range order parameter, $S = r_a^{Na} + r_b^{Pr} - 1$; where r_a and r_b represents the fraction of 3a and 3b Wyckoff sites occupied by Na and Pr, respectively. The value of the order parameter ranges from 0 – 1, with S = 0 for a completely random cation arrangement and S = 1 for a fully ordered system, where each cation occupies its specific sublattice. In the initial Rietveld refinement of R- $NaPrS_2$ samples obtained at various cooling rates; Na, Pr and S atoms were only located on the 3a, 3b and 6c sites, respectively. A significant improvement in fitting parameters were observed when the occupancies of the mixed Na/Pr sites were allowed to refine while constraining each of the 3a and 3b site occupancy to one. This suggests that the cations in R- $NaPrS_2$ are not completely ordered because some fraction of Na atoms are in 3b site, and some fraction of Pr atoms are in 3a sites. The results of final Rietveld refinement and long-range order parameter are summarized in Table 1-1.

Table 1-1. Refinement and long-range order parameters for R-$NaPrS_2$ at various cooling rates.

Cooling rate (°C/h)	Unit cell (Å)		Atom	Wyckoff	U_{iso} (pm^2)	Site occupancy	Long range order parameter
	a	*c*					
20	4.125(1)	19.981(1)	Na1	3a	0.5356(2)	0.9981(1)	0.9963(2)
			Na2	3b	0.5248(5)	0.0019(1)	
			Pr1	3b	0.5248(5)	0.9981(1)	
			Pr2	3a	0.5356(2)	0.0019(1)	
			S1	6c	0.5118(2)	1.0000(2)	

50	4.121(1)	20.048(2)	Na1	3a	0.6825(7)	0.9417(3)	0.8833(4)
			Na2	3b	0.4124(3)	0.0583(3)	
			Pr1	3b	0.4124(3)	0.9417(3)	
			Pr2	3a	0.6825(7)	0.0583(3)	
			S1	6c	0.6963(3)	1.000(1)	
75	4.112(2)	20.071(1)	Na1	3a	0.7547(3)	0.7803(5)	0.5606(6)
			Na2	3b	0.8834(5)	0.2197(5)	
			Pr1	3b	0.8834(5)	0.7803(5)	
			Pr2	3a	0.7547(3)	0.2197(5)	
			S1	6c	0.5280(2)	1.0000(2)	

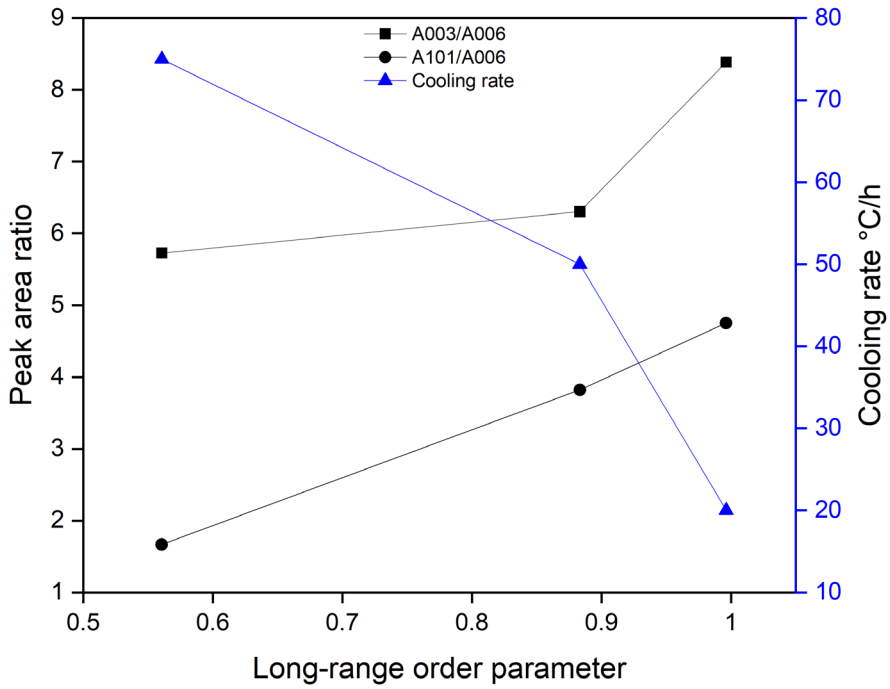

Figure 4-7. Peak area ratio of superlattice to fundamental reflection as a function of long-range order parameter (black) and long-range order parameter in dependence on the cooling rate during crystal growth (blue).

4.3.3 Optical properties

Figure 4-8 depicts Tauc plots [45] constructed from Kubelka-Munk transformation of diffuse reflectance spectroscopy data of $NaPrS_2$ series. The samples showed a progressive increase in direct bandgap energy from 2.75 eV in the fully disordered structure to 3.03 eV in the most ordered phase, suggesting that the bandgap of $NaPrS_2$ lies within this energy range. The optical bandgap of $NaPrS_2$ prepared by quenching, 75, 50 and 20 °C/h cooling rates were 2.75, 2.82, 2.96 and 3.03 eV, respectively, indicating that the degree of cation order affects the optical property of the parent material. The degree of cation order in silver-bismuth double perovskites was reported to influence their optical bandgap [49] which is in good agreement with our measurement.

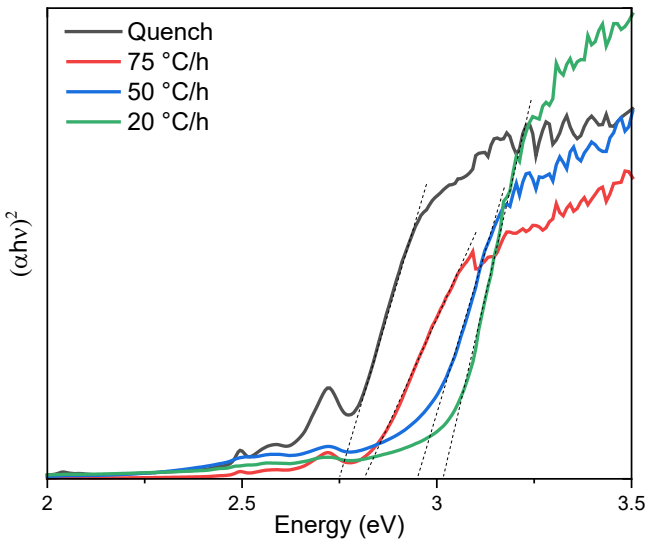

Figure 4-8. Tauc plots for $NaPrS_2$ at various cooling rates.

Figure 4-9 shows the **c**orrelation between the optical bandgap and long-range order parameter for $NaPrS_2$ samples. It was observed that the optical bandgap shifted to higher energy as long-range

order parameter calculated using Bragg-Williams method increased, suggesting that tuning of the degree of cation order enables corresponding tuning of optical bandgap.

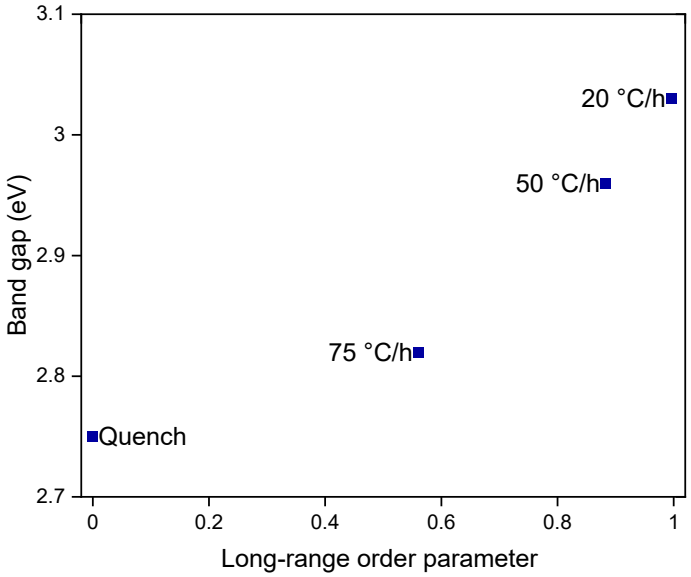

Figure 4-9. Correlation between the optical bandgap and long-range order parameters of $NaPrS_2$ series.

4.4 CONCLUSIONS

Two polymorphs of ternary praseodymium sulfide, $NaPrS_2$ were successfully synthesized via the solid-state method. A disordered C-$NaPrS_2$ phase was synthesized by either rapid cooling or reheating of layered R-$NaPrS_2$ at 850 °C or using more than 10% excess Na_2S. Interestingly, layered R- $NaPrS_2$ was synthesized for the first time to the best of our knowledge by slow cooling to room temperature. Series of R- $NaPrS_2$ were synthesized at various cooling rates and the degree of Na/Pr order was measured using the Bragg – Williams equation. R-$NaPrS_2$ exhibited near-complete to partial ordering of Na/Pr, suggesting that the long-range order parameter decrease with increasing cooling rate. The change in peak area ratio of superlattice (A_{003} and A_{101}) to peak area of fundamental reflections (A_{006}) in a series of R-$NaPrS_2$ samples, further supported the notion that

long-range order parameter was affected by a variation in cooling rate. The optical direct bandgap of $NaPrS_2$ could be tuned by varying the degree of Na/Pr order. The bandgap value trended from 2.75 eV for the most disordered phase to 3.03 eV for the near-completely ordered polymorph. The result suggests that materials with variable degree of cation order can be used for the design of optoelectronic devices with tunable bandgaps.

4.5 REFERENCES

1. Woods-Robinson, R.; Han, Y.; Zhang, H.; Ablekim, T.; Khan, I.; Persson, K. A.; Zakutayev, A., Wide band gap chalcogenide semiconductors. *Chemical reviews* **2020,** *120* (9), 4007-4055.
2. Choi, W.; Choudhary, N.; Han, G. H.; Park, J.; Akinwande, D.; Lee, Y. H., Recent development of two-dimensional transition metal dichalcogenides and their applications. *Materials today (Kidlington, England)* **2017,** *20* (3), 116-130.
3. Wang, Q. H.; Kalantar-Zadeh, K.; Kis, A.; Coleman, J. N.; Strano, M. S., Electronics and optoelectronics of two-dimensional transition metal dichalcogenides. *Nature nanotechnology* **2012,** *7* (11), 699-712.
4. Zhang, D.; Zhang, B.; Zhou, Z.; Peng, K.; Wu, H.; Wang, H.; Wang, G.; Han, G.; Wang, G.; Zhou, X.; Lu, X., Ultralow lattice thermal conductivity of cubic $CuFeS_2$ induced by atomic disorder. *Chemistry of materials* **2021,** *33* (24), 9795-9802.
5. Niki, S.; Contreras, M.; Repins, I.; Powalla, M.; Kushiya, K.; Ishizuka, S.; Matsubara, K., CIGS absorbers and processes. *Progress in photovoltaics* **2010,** *18* (6), 453-466.
6. Zhao, H.-J.; Zhong, X.-A., Synthesis, crystal structure, and optical properties of the noncentrosymmetric sulfide $Ce_8Sb_2S_{15}$. *Journal of solid state chemistry* **2017,** *251*, 65-69.
7. Hsiao, K.-J.; Sites, J. R., Electron reflector to enhance photovoltaic efficiency: application to thin-film CdTe solar cells. *Progress in photovoltaics* **2012,** *20* (4), 486-489.
8. Wu, Q.; Xue, C.; Li, Y.; Zhou, P.; Liu, W.; Zhu, J.; Dai, S.; Zhu, C.; Yang, S., Kesterite Cu_2ZnSnS_4 as a low-cost inorganic hole-transporting material for high-efficiency perovskite solar cells. *ACS applied materials & interfaces* **2015,** *7* (51), 28466-28473.
9. Zhou, M.; Xiao, K.; Jiang, X.; Huang, H.; Lin, Z.; Yao, J.; Wu, Y., Visible-light-responsive chalcogenide photocatalyst Ba_2ZnSe_3: crystal and electronic structure, thermal, optical, and photocatalytic activity. *Inorganic chemistry* **2016,** *55* (24), 12783-12790.
10. Kim, C.; Nguyen, T. P.; Le, Q. V.; Jeon, J.-M.; Jang, H. W.; Kim, S. Y., Performances of liquid-exfoliated transition metal dichalcogenides as hole injection layers in organic light-emitting diodes. *Advanced functional materials* **2015,** *25* (28), 4512-4519.
11. Chen, E. M.; Stoyko, S. S.; Aitken, J. A.; Poudeu, P. F. P., Tuning the optical, electronic and thermal properties of $Cu_3NbS_{4-x}Se_x$ through chemical substitution. *Inorganic chemistry frontiers* **2017,** *4* (9), 1493-1500.
12. Sotelo, P.; Orr, M.; Galante, M. T.; Hossain, M. K.; Firouzan, F.; Longo, C.; Kormányos, A.; Sarker, H.; Janáky, C.; Huda, M. N.; Rajeshwar, K.; Macaluso, R. T., Role of f electrons in the optical and photoelectrochemical behavior of $Ca(La_{1-x}Ce_x)_2S_4$ ($0 \leq x \leq 1$). *Inorganic chemistry* **2019,** *58* (7), 4553-4560.
13. Gaillard, N.; Prasher, D.; Chong, M.; Deangelis, A.; Horsley, K.; Ishii, H. A.; Bradley, J. P.; Varley, J.; Ogitsu, T., Wide-Bandgap $Cu(In,Ga)S_2$ photocathodes integrated on transparent conductive $F:SnO_2$ substrates for chalcopyrite-based water splitting tandem devices. *ACS applied energy materials* **2019,** *2* (8), 5515-5524.

14. Christian, T. M.; Beaton, D. A.; Mukherjee, K.; Alberi, K.; Fitzgerald, E. A.; Mascarenhas, A., Amber-green light-emitting diodes using order-disorder $Al_xIn_{1-x}P$ heterostructures. *Journal of applied physics* **2013,** *114* (7).
15. Barrigón, E.; Barrutia, L.; Ochoa, M.; Rey-Stolle, I.; Algora, C., Effect of Sb on the quantum efficiency of GaInP solar cells. *Progress in photovoltaics* **2016,** *24* (8), 1116-1122.
16. Schnepf, R. R.; Cordell, J. J.; Tellekamp, M. B.; Melamed, C. L.; Greenaway, A. L.; Mis, A.; Brennecka, G. L.; Christensen, S.; Tucker, G. J.; Toberer, E. S.; Lany, S.; Tamboli, A. C., Utilizing site disorder in the development of new energy-relevant semiconductors. *ACS energy letters* **2020,** *5* (6), 2027-2041.
17. Leube, B. T.; Collins, C. M.; Daniels, L. M.; Duff, B. B.; Dang, Y.; Chen, R.; Gaultois, M. W.; Manning, T. D.; Blanc, F. d. r.; Dyer, M. S.; Claridge, J. B.; Rosseinsky, M. J., Cation disorder and large tetragonal supercell ordering in the li-rich argyrodite $Li_7Zn_{0.5}SiS_6$. *Chemistry of materials* **2022,** *34* (9), 4073-4087.
18. Ahmed, N.; Nisar, J.; Kouser, R.; Nabi, A. G.; Mukhtar, S.; Saeed, Y.; Nasim, M. H., Study of electronic, magnetic and optical properties of KMS_2 (M = Nd, Ho, Er and Lu): first principle calculations. *Materials Research Express* **2017,** *4* (6), 065903.
19. Isaacs, T. J.; Hopkins, R. H.; Kramer, W. E., Study of $NaLaS_2$ as an infrared window material. *Journal of Electronic Materials* **1975,** *4*, 1181-1189.
20. Jarý, V.; Havlák, L.; Bárta, J.; Buryi, M.; Mihóková, E.; Rejman, M.; Laguta, V.; Nikl, M., Optical, structural and paramagnetic properties of Eu-doped ternary sulfides $ALnS_2$ (A = Na, K, Rb; Ln = La, Gd, Lu, Y). *Materials* **2015,** *8* (10), 6978-6998.
21. Jarý, V.; Havlák, L.; Bárta, J.; Mihóková, E.; Nikl, M., Luminescence and structural properties of $RbGdS_2$ compounds doped by rare earth elements. *Optical materials* **2013,** *35* (6), 1226-1229.
22. Wu, Y.; Wang, X.; Wang, Y.; Duan, Y.; Peng, M., Insights into electronic and optical properties of $AGdS_2$ (A = Li, Na, K, Rb and Cs) ternary gadolinium sulfides. *Optical materials* **2021,** *114*, 110963.
23. Liu, W.; Zhang, Z.; Ji, J.; Liu, Y.; Li, J.; Wang, X.; Lei, H.; Chen, G.; Zhang, Q., Rare-earth chalcogenides: A large family of triangular lattice spin liquid candidates. *Chinese physics letters* **2018,** *35* (11), 117501.
24. Sarkar, R.; Schlender, P.; Grinenko; Haeussler, E.; Baker, P. J.; Doert, T.; Klauss, H. H., Quantum spin liquid ground state in the disorder free triangular lattice $NaYbS_2$. *Physical review. B* **2019,** *100* (24), 1.
25. Baenitz, M.; Schlender, P.; Sichelschmidt, J.; Onykiienko, Y. A.; Zangeneh, Z.; Ranjith, K. M.; Sarkar, R.; Hozoi, L.; Walker, H. C.; Orain, J. C.; Yasuoka, H.; van den Brink, J.; Klauss, H. H.; Inosov, D. S.; Doert, T., $NaYbS_2$: A planar spin- 12 triangular-lattice magnet and putative spin liquid. *Physical review. B* **2018,** *98* (22).
26. Ohtani, T.; Honjo, H.; Wada, H., Synthesis, order-disorder transition and magnetic properties of $LiLnS_2$, $LiLnSe_2$, $NaLnS_2$ and $NaLnSe_2$ (Ln=Lanthanides). *Materials research bulletin* **1987,** *22* (6), 829-840.

27. Fábry, J.; Havlák, L.; Dušek, M.; Vaněk, P.; Drahokoupil, J.; Jurek, K., Structure determination of $KLaS_2$, $KPrS_2$, $KEuS_2$, $KGdS_2$, $KLuS_2$, KYS_2, $RbYS_2$, $NaLaS_2$ and crystal-chemical analysis of the group 1 and thallium(I) rare-earth sulfide series. *Acta crystallographica Section B, Structural science, crystal engineering and materials* **2014,** *70* (2), 360-371.
28. Cotter, J. P.; Fitzmaurice, J. C.; Parkin, I. P., New routes to alkali-metal-rare-earth-metal sulfides. *Journal of materials chemistry* **1994,** *4* (10), 1603-1609.
29. Verheijen, A. W.; Van Enckevort, W. J. P.; Bloem, J.; Giling, L. J., Flux growth, analysis and crystallographic aspects of alkali rare earth sulfides. *Le Journal de Physique Colloques* **1975,** *36* (C3), C3-39-C3-45.
30. Sato, M.; Adachi, G.; Shiokawa, J., Preparation and structure of sodium rare-earth sulfides, $NaLnS_2$ (Ln; rare earth elements). *Materials research bulletin* **1984,** *19* (9), 1215-1220.
31. Schleid, T.; Lissner, F., Single-crystals of $NaMS_2$ (M = Ho-Lu) from reactions of the lanthanides with sulfur in the presence of NaCl. *European journal of solid state and inorganic chemistry* **1993,** *30* (9), 829-836.
32. Li, H.; Li, P.; Zhang, J.; Tian, L.; Li, H.; Zhao, J.; Luo, F., Powder preparation and high infrared performance of $NaLaS_2$ transparent ceramics. *Ceramics international* **2018,** *44* (1), 83-88.
33. Romero, S.; Mosset, A.; Trombe, J. C., Study of some ternary and quaternary systems based on gamma-Ce_2S_3 using oxalate complexes: stabilization and coloration. *Journal of alloys and compounds* **1998,** *269* (1-2), 98-106.
34. Tsay, B. J.; Wang, L. H., A study on infrared transmission of lanthanum sulfide and oxysulfide in the 2.5–14 μm region. *Materials Letters* **1998,** *34* (3), 180-183.
35. Li, H.; Ding, W.; Gu, Z.; Li, H.; Zhao, J.; Fu, L., Preparation and infrared transmittance of $NaLaS_2$ ceramics. *Materials Letters* **2015,** *156*, 62-64.
36. Kanatzidis, M. G., Discovery-synthesis, design, and prediction of chalcogenide phases. *Inorganic chemistry* **2017,** *56* (6), 3158-3173.
37. Kanatzidis, M. G., Molten alkali-metal polychalcogenides as reagents and solvents for the synthesis of new chalcogenide materials. *Chemistry of materials* **1990,** *2* (4), 353-363.
38. Shoemaker, D. P.; Chung, D. Y.; Mitchell, J. F.; Bray, T. H.; Soderholm, L.; Chupas, P. J.; Kanatzidis, M. G., Understanding fluxes as media for directed synthesis: In situ local structure of molten potassium polysulfides. *Journal of the American Chemical Society* **2012,** *134* (22), 9456-9463.
39. Luo, X.; Ma, L.; Xing, M.; Fu, Y.; Zhou, X.; Sun, M., Preparation of $NaGdS_2$ via thermolysis of $Gd[S_2CN(C_4H_8)]_3$-phen complexes and sodium diethyldithiocarbamate mixtures. *Materials research bulletin* **2013,** *48* (5), 1999-2001.
40. Pomelova, T. A.; Khandarkhaeva, S. E.; Podlipskaya, T. Y.; Naumov, N. G., Top-down synthesis and characterization of exfoliated layered $KLnS_2$ nanosheets, their colloidal dispersions and films. *Colloids and surfaces. A, Physicochemical and engineering aspects* **2016,** *504*, 298.

41. Havlák, L.; Fábry, J.; Henriques, M.; Dušek, M., Structure determination of $KScS_2$, $RbScS_2$ and $KLnS_2$ (Ln = Nd, Sm, Tb, Dy, Ho, Er, Tm and Yb) and crystal–chemical discussion. *Acta crystallographica. Section C, Structural chemistry* **2015,** *71* (7), 623-630.
42. Ding, Y.; Gu, J.; Zhang, T.; Yin, A.-X.; Yang, L.; Zhang, Y.-W.; Yan, C.-H., Chemoaffinity-mediated synthesis of $NaRES_2$-based nanocrystals as versatile nano-building blocks and durable nano-pigments. *Journal of the American Chemical Society* **2012,** *134* (6), 3255-3264.
43. Degen, T.; Sadki, M.; Bron, E.; König, U.; Nénert, G., The HighScore suite. *Powder diffraction* **2014,** *29* (S2), S13-S18.
44. Ballestracci, R.; Bertaut, E. F., Etude Cristallographique de Sulfures de Terres rares et de Sodium. *Bulletin de la Societe Francaise Mineralogie et de Cristallographie* **1964,** *87* (4), 512.
45. Tauc, J.; Grigorovici, R.; Vancu, A., Optical properties and electronic structure of amorphous germanium. *Physica status solidi (b)* **1966,** *15* (2), 627-637.
46. Schleid, T.; Lissner, F., A-Pr_2S_3, D-Ho_2S_3 and E-Yb_2S_3: Synthesis and single crystal structure investigations. *A journal of chemical sciences* **1996,** *51* (5), 733-738.
47. YU, S. W., Dongri; GAO, Xiaolong ; SU, Haiquan, Effects of the precursor size on the morphologies and properties ofγ-Ce_2S_3 as a pigment. *Journal of rare earths* **2014,** *32* (6), 540-544.
48. Warren, B. E., *X-Ray Diffraction*. Dover Publications: New York, 1990.
49. Savory, C. N.; Walsh, A.; Scanlon, D. O., Can Pb-free halide double perovskites support high-efficiency solar cells? *ACS energy letters* **2016,** *1* (5), 949-955.

CHAPTER 5

GENERAL SUMMARY

Investing in the development of new semiconductor materials and improving existing ones is crucial for the conversion of solar energy and environmental remediation. One approach to enhancing the performance of visible-light active PEC catalysts is by tuning the optoelectronic properties of binary, ternary, and quaternary oxides and chalcogenides for solar fuel generation. This dissertation utilized time- and energy-efficient solution combustion synthesis, as well as an environmentally friendly solid-state method, to prepare ternary oxides and sulfides with a modifiable bandgap for solar energy conversion.

Chapter 2 demonstrated a fundamental understanding of the impact of substituting alkaline earth metals on the electronic, optical, and photoelectrochemical traits of copper metavanadate. Mixed compositions of $A_{0.1}Cu_{0.9}V_2O_6$ (A = Mg, Ca) photoanodes were prepared via SCS method. Polycrystalline powder samples were confirmed to be copper and alkaline earth metal metavanadate solid solutions through PXRD, TEM, XPS and Raman results. The incorporation of copper led to a reduction in the optical bandgap, as shown by DRS and theoretical studies. Additionally, the alloy composition had a significant impact on the photoelectrochemical properties.

In Chapter 3, we introduced quaternary oxides through the partial substitution of copper for alkaline earth metal in an A-O-V system using SCS. The addition of copper to alkaline earth metal pyrovanadates resulted in a significant enhancement in photoanode performance. The formation of the end members and solid solutions outlined in Chapter 3 were confirmed by PXRD, TEM, XPS, ICP-OES, and Raman data. Incorporating copper into $A_2V_2O_7$ led to a bathochromic shift in

the optical bandgap energy, as evidenced by DRS and theoretical studies. Additionally, using PXRD, we demonstrated how SCS can be utilized to synthesize various polymorphs of copper and alkaline earth metal pyrovanadates.

Chapter 4 employed the flux method and varying cooling rates to synthesize $NaPrS_2$ in order to achieve cation ordering and stabilize one structure type over the other. Our work revealed that $NaPrS_2$ can crystallize in both cubic (C) and rhombohedral (R) structure types, contrary to previous reports that only mentioned the existence of C-$NaPrS_2$. We observed an order-disorder phase transition when heating the R structure at 850 °C and identified methods to significantly reduce oxysulfide impurities. The Bragg-Williams equation was used to evaluate the long-range order parameter of various R-$NaPrS_2$ samples, and our findings indicated that cation ordering greatly impacts the optical band gap of $NaPrS_2$.

Additional research into different approaches for enhancing the performance of photoelectrodes will help advance the investigation of semiconductors that will be commercially available for converting water into hydrogen and oxygen using solar energy. To enhance the PEC performance of the diverse samples we presented, more methods are required to impede photo corrosion and enhance the efficiency of charge separation, the mobility of charge carriers, the surface electrocatalytic activity, and the minority carrier diffusion length. The results presented in this dissertation do, however, establish the potential of the new generation ternary oxide and sulfide semiconductors for a host of practical technological applications.

BIOGRAPHICAL INFORMATION

Fahad Ibrahim Danladi, a native of Kano, Nigeria, has an impressive academic background. He graduated from Kano University of Science and Technology with a bachelor's degree in chemistry and went on to earn a master's degree in applied chemistry from Jordan University of Science and Technology. After working as a lecturer of chemistry in his home country, he decided to pursue further studies and moved to Texas, United States where he obtained a second master's degree in chemistry from the prestigious University of Texas at Arlington. Driven by his interest in scientific research and thirst for knowledge, Fahad went on to earn a doctorate degree in chemistry. His research work focused on band gap engineering in multinary oxides and sulfides semiconductors for solar energy conversion. His goal is to pursue his research journey either in an academic setting or in the industry.